

Copyright
by
Matthew Scott Byrne
2021

**The Dissertation Committee for Matthew Scott Byrne Certifies that this is
the approved version of the following Dissertation:**

**Extraordinary Acoustic Transmission via Supercoupling and Self -
Interference Cancellation**

Committee:

Andrea Alù, Supervisor

Michael R. Haberman, Co-Supervisor

Mark F. Hamilton

Neal A. Hall

Mark McDermott

**Extraordinary Acoustic Transmission via Supercoupling and Self -
Interference Cancellation**

by

Matthew Scott Byrne

Dissertation

Presented to the Faculty of the Graduate School of
The University of Texas at Austin
in Partial Fulfillment
of the Requirements
for the Degree of

Doctor of Philosophy

The University of Texas at Austin

August 2021

Dedication

To my parents and to my girlfriend for their unwavering support and encouragement.

Acknowledgements

This dissertation was inspired and supported by the guidance of my advisor, Professor Andrea Alù. I would like to thank him for his generous investment of time, as well as for encouragement and advice throughout my time in graduate school. I would also like to thank my co-advisor, Professor Michael Haberman, for extensive discussions and helpful advice, especially regarding the experimental work and dissertation writing. I was very fortunate to have the support and guidance from both Dr. Alù and Dr. Haberman during my time at UT.

Moreover, I must thank Professor Mark Hamilton for his exceptional dedication to teaching Physical Acoustics at UT Austin and for his generous availability during office hours throughout my time here. I'm also grateful to Dr. Neal Hall and Dr. Mark McDermott for very helpful advice and discussions.

I was lucky to collaborate on a portion of this research with Dr. Hussein Esfahlani, and I thank him for his guidance, patience, and integrity while assisting me in developing analytical theory, building numerical simulations, scrutinizing results, and preparing my first academic publications. Additionally, special thanks is given to Matthew McDermott, who was an invaluable research assistant during our early experimental investigations.

Much thanks are also owed to the following researchers for useful discussions related to this work (in alphabetical order): Drs. Anthony Bonomo, Ahmed Kord, Caleb Sieck, Jason Smoker, Dimitrios Sounas, and Alexey Titovich.

In addition, I would like to thank all of my fellow students in the Alù Group and the Acoustics program at UT for their friendship and support throughout my years in Austin. I must also thank our administrative staff: Melanie Gulick, Karen Little, Apipol

Piman, Melody Singleton, and Jaymie Udan, for their help in navigating hurdles along the way. Finally, I would like to acknowledge financial support from the DoD SMART Scholarship and the In-house Laboratory Independent Research (ILIR) program from the Office of Naval Research.

Statement of Shared Contributions

Portions of Chapters II and III have already been published in the papers cited below and were developed as a group effort.

- Byrne, M. S., Esfahlani, H., McDermott, M., & Alù, A. (2019). Acoustic supercoupling in a zero-compressibility waveguide. *Research*, 2019.
- Byrne, M. S., Esfahlani, H., & Alù, A. (2020). Acoustic power divider based on compressibility-near-zero propagation. *Physical Review Applied*, 14(2), 024057.

This work was completed with Hussein Esfahlani and myself as first co-authors, followed by Matthew McDermott and Andrea Alù as additional authors. Hussein Esfahlani initiated the research. Hussein and I spent equal effort on the analytical theory and numerical simulations. I took the lead on the experimental measurements with the assistance of Matt McDermott. Andrea Alù supervised the research. Chapters I, IV, V, and VI were developed wholly by myself and my co-supervisors, Andrea Alù and Michael Haberman.

Abstract

Extraordinary Acoustic Transmission via Supercoupling and Self-Interference Cancellation

Matthew Scott Byrne, PhD

The University of Texas at Austin, 2021

Supervisor: Andrea Alù

Co-Supervisor: Michael Haberman

Supercoupling is a widely researched topic in wave engineering, which has been used to build coupling channels that can, in principle, support total transmission and complete phase uniformity, independent of the length of the channel. This has generally been accomplished by employing dispersion in media that display a near-zero index. In the field of acoustics, prior works have required the presence of periodic embedded resonators, such as membranes or Helmholtz resonators, in order to observe near-zero properties. Here it is shown, theoretically and experimentally, that supercoupling can occur in an acoustic channel without the presence of embedded resonators. A compressibility-near-zero (CNZ) acoustic channel was observed to show remarkable properties analogous to those found in electromagnetics. Furthermore, these principles are employed to develop an acoustic power divider, which takes advantage of the CNZ properties of the channel to also exhibit phase invariance at the output. In the next section, another extraordinary acoustic transmission phenomenon is explored, regarding the potential for sending and receiving from a single acoustic transducer at the same time and at the same frequency. This is made possible

through an electrical circuit that is designed to cancel self-interfering signals in acoustic measurement systems. Systems that employ self-interference cancellation (SIC) are often referred to as simultaneous transmit and receive (STAR) or in-band full duplex (IBFD) systems, which have recently enabled sending and receiving of Radio Frequency (RF) signals at the same time and at the same frequency. This has led to commercialization efforts with the promise of doubling the throughput of traditional radio systems including Wi-Fi and 5G cellular communications. Prior to these advances, researchers in vibration control explored self-sensing actuator systems, also referred to as sensoriaactuators or sensorless control systems. Inspired by these developments, these approaches are combined and extended to explore STAR functionality in an acoustic measurement system. First, self-interference cancellation (SIC) is applied to time-domain measurements to demonstrate the potential for a practical, single-transducer ultrasonic nondestructive evaluation (NDE) system to measure echo returns while it is actively transmitting at the same frequency. Theoretical models and experimental results are presented and discussed.

Table of Contents

List of Tables	xiii
List of Figures	xv
Chapter I: Introduction.....	1
1.1 Objective and motivation	1
1.2 Hypothesis and strategy	6
1.3 Dissertation overview	9
Chapter II: Principles of Supercoupling and Self-Interference Cancellation	11
2.1 Supercoupling	11
<u>2.1.1 Development and Principles of Supercoupling</u>	11
<u>2.1.2 Review of Zero-Index Electromagnetics and Electromagnetic Supercoupling</u>	13
<u>2.1.3 Review of Zero-Index Acoustic Metamaterials and Acoustic Supercoupling</u>	15
<u>2.1.4 Principles and Realization of Acoustic Supercoupling</u>	16
<u>2.1.5 Supercoupling Power Dividers</u>	19
2.2 Self-interference cancellation (SIC).....	23
<u>2.2.1 Development and Principles of Self-Interference Cancellation</u>	23
<u>2.2.2 STAR in Acoustics and Vibration Control</u>	26
<u>2.2.3 Motivation and Opportunities in STAR Acoustics</u>	30
2.3 Summary	36
Chapter III: Acoustic Supercoupling with Compressibility-Near-Zero Material Properties	38
3.1 Introduction.....	38

3.2 Results of the CNZ Supercoupling study.....	39
3.3 Discussion of CNZ Supercoupling results	49
3.4 Materials and Methods.....	50
<u>3.4.1 Transmission-line model for acoustic supercoupling</u>	50
<u>3.4.2 Cut-off in acoustic waveguides and compressibility-near-zero</u>	51
<u>3.4.3 Numerical modeling</u>	53
<u>3.4.4 Measurements</u>	54
3.5 Supercoupling power divider with CNZ properties.....	54
<u>3.5.1 Theory</u>	54
A. Equi-phase power division.....	55
B. Equi-phase zero-reflection power division	58
C. Equi-phase and equi-amplitude zero-reflection power division	58
<u>3.5.2 Realistic Implementation and Simulations</u>	59
A. Lossless case	61
B. Modeling radiation losses and their relation to geometric scaling	68
C. Influence of the visco-thermal acoustic boundary layer	72
3.6 Conclusions	77
Chapter IV: Simultaneous Transmit and Receive with Passive Circuit Elements at Ultrasonic Frequencies.....	80
4.1 Approach.....	80
4.1 Linear System Models	83
4.3 Evaluation of SIC and SIR.....	92
4.4 Chapter summary	94

Chapter V: Experimental Results and Applications of Acoustic STAR.....	95
5.1 Measurement approach and setup.....	95
5.2 Predicting SIC and SIR with the system function	96
5.3 Evaluating the transducer and acoustic response.....	101
5.4 Assessing the effect of component parasitics	104
5.5 Predicting the SIR and measuring the SINR.....	107
5.5 Parasitic modeling with a least-mean-squares fit.....	112
5.6 Broadband SIC and SIR with the least-mean-squares fit solution.....	117
5.7 Time division and time overlap measurements	122
5.8 Conclusions	127
Chapter VI: Conclusions and Future Directions.....	128
6.1 Conclusions and Contributions	128
6.2 Future Directions.....	130
<u>6.2.1 Near-Surface Acoustic Imaging with Self-Interference</u> <u>Cancellation</u>	131
<u>6.2.2 Enhancing Doppler Shift Detection with Acoustic Self-</u> <u>Interference Cancellation</u>	134
Bibliography.....	140

List of Tables

Table 1. Overview of research plan.....	8
Table 2. Explains several possibilities for leveraging STAR in acoustic measurement systems and describes some of the technical differences between each area.	34
Table 3. Component values used to compute the output of the LC-matched bridge circuits as presented in the corresponding figures listed on the leftmost column. All configurations assume that $v_{in} = 1.0v_{pk}$, $R_0 = 50\Omega$, $v_p = 0.1v_{pk}$, $Z_p = 579pF \parallel 3.85k\Omega$, $Z_1 = 560pF$, and use the layout of Figure 20(a).....	88
Table 4. Component values used to compute the output of the LC-matched bridge circuits as presented in the corresponding figures listed on the leftmost column. The first two rows use the topology of Figure 20(a) and the last row uses that of Figure 20(b).	106
Table 5. Experimental parameters used for measurements shown in Figure 31(d). All measurements used the layout of Figure 20(a) with $v_{in} = 1.2V_{pk-pk}$, $R_0 = 53\Omega$, $Z_{M1} = 3.3nF + 0.1\Omega$, $Z_{M2} = 184\mu H + 28.2\Omega$, $Z_1 = 560pF + 0.1\Omega$, $Z_2 = 1/j\omega C_2$, $Z_3 = (1/j\omega C_3) \parallel R_3$, and Z_p representing the V318 transducer with impedance values described in Figure 34. Parasitic resistances for all capacitors were measured as less than 0.2Ω	110

Table 6. Parameter values used for the measurement and predictions shown in Figure 36(a)-(b). ν_p was determined by the measured system function at $D = 10\text{cm}$. The measurement employed a 50 Ohm multiturn potentiometer in series with Z_3 to compensate for parasitic loss in the breadboard, cables, and wires. Maximum SIR was observed for the series resistance value reported in the table of $30.6\ \Omega$	120
Table 7. Parameter values used to fit the analytical model to the measured data, as described in Figure 36. All table entries (except for the first column) list the parameter value and the percent change from the corresponding value used in the measurement of SINR. In these predictions, Z_3 is represented by the S&B model from Figure 27 (with $G_0 \rightarrow \infty$) plus a series resistance, R_s . Other parameters used were $R_0=52.8\ \Omega$, $Z_{M1}=3.3\ \text{nF}$, $Z_{M2} = 180\ \mu\text{H} + 3\ \Omega$, $Z_1=571\ \text{pF}$, and $Z_p = \text{LSQ S\&B Model}$ (reported in Figure 34).	122

List of Figures

- Figure 1.** (a) Geometry and electric field distribution through an epsilon-near-zero (ENZ) supercoupler with arbitrary bends in the coupling channel. Adapted from [15]. (b) Plot of the wave impedance as a function of frequency, which demonstrates that channels filled with mismatched materials can be matched to the impedance of a supercoupler at the ENZ frequency, which is 1.5 GHz in this case. Adapted from [28]. (c) Amplitude and phase of transmission through an electromagnetic supercoupler. Adapted from [15]. (d) Diagram of a mu-near-zero (MNZ) supercoupler. Adapted from [37].15
- Figure 2.** (a) DNZ tunneling around a sharp bend formed by a sound hard boundary, using a space-coiled metamaterial structure. Adapted from [41]. (b) Acoustic pressure of density-near-zero (DNZ) acoustic supercoupling through ultranarrow channels with arbitrary bending and channel lengths. Adapted from [45]. (c) Energy transmission coefficient of a DNZ structure from (b), which shows full power transmission at the frequency where the channel exhibits DNZ material properties for two different channel lengths. Adapted from [45]. (d) Acoustic leaky wave antenna, which radiates from endfire to backfire depending upon the frequency of excitation. The waveguide exhibits DNZ properties at the frequency which corresponds to broadside radiation, due to the response of the acoustically loaded membranes. Adapted from [40].18

Figure 3. Examples of network devices and power dividers in electromagnetics and acoustics, which may be enhanced by metamaterial properties. (a) An electromagnetic metamaterial 1:4 series power divider that supplies equal power split among all four output ports. (b) A series power divider containing conventional one-wavelength long meander lines for in-phase signals at the output ports. (a)-(b) Both adapted from [63]. (c) An electromagnetic infinite wavelength N -port series power divider based on a composite right/left-handed (CRLH) transmission line, which exhibits near-zero index material properties at select frequencies. This power divider supports arbitrary element spacing and length, due to the infinite wavelength in the waveguide. Adapted from [62]. (d) An acoustic network device referred to as a Herschel-Quincke tube, which re-routes an incident signal from Port 1 into a main branch, 2, and a branched conduit, 3. The difference in phase between the two branches result in frequency-dependent transmission behavior at the output from Port 4. Adapted from [68]. (e) A four-port acoustic power splitter, referred to as a rat-race coupler. This passive reciprocal device couples all power from one input channel into two output channels, while isolating it from the fourth channel. Adapted from [70].22

Figure 4. Overview of self-interference cancellation (SIC) systems in radio frequency (RF) communications. (a) SIC system that combines antenna isolation with digital interference cancellation to achieve in-band full duplex communication. Adapted from [22]. (b) A system that performs SIC with a combination of passive cancellation from a circulator, as well as a hybrid analog-digital cancellation system. Adapted from [71]. (c) An all-digital approach to SIC for RF applications, which leverages an auxiliary receiver chain to emulate the effects of the ordinary receiver chain on the received signal. Adapted from [81]......25

Figure 5. Overview of SIC systems in acoustic and vibration systems. (a) Overview of a single-transducer STAR acoustic system. The STAR system is used to isolate the transmitted and received signals while the transducer simultaneously sends and receives over the same frequency band. (b) A custom-built directional coupler was constructed to perform SIC on a 1 MHz ultrasonic transducer interfaced with a solid material sample. Adapted from [23]. (c) A difference amplifier was combined with a compensation circuit, consisting of a phase-shifter and variable gain amplifier, to cancel the self-interfering signal on a 1 MHz transducer that is configured to measure its own output from a rigid reflector in water. Adapted from [90]. (d) A passive bridge circuit is designed to perform SIC on a piezoelectric actuator at frequencies around 100 Hz. The measurement setup uses a vibrating cantilever beam with a single actuator that both senses the vibration and actively damps it simultaneously, using a closed loop control algorithm. Adapted from [24].28

Figure 6. Conceptual demonstration of the benefits of doubling the time-bandwidth product for STAR measurements. (a) Timeseries of a linear FM sweep and its corresponding normalized frequency spectrum, representing the case of a traditional time-division measurement. (b) Timeseries of a linear FM sweep with the same frequency content as above but now with doubled duration, representing a continuous transmit-receive STAR measurement. This results in a spectrum with twice the amount of power in each frequency bin. (c) Timeseries of a linear FM sweep with double the bandwidth compared to (a), but with the same output power across the spectrum.31

Figure 7. An example of enhanced near-surface acoustic imaging using acoustic STAR. This approach can be viewed as an alternative to the signal processing techniques such as matched filtering, or as a method that may augment the capability of a given matched filter due to the finite pulse compression ratio.32

Figure 8. Geometry of the CNZ supercoupling experiment. The geometry under analysis consists of input and output waveguides connected by a much wider intermediate channel with variable length. The output port remains flush with the face of the wooden boundary and moves along with the boundary as L is varied. (*Inset bottom*): transmission line model. (*Inset top-left*): photograph of the experimental setup.....39

Figure 9. Waveguides with two soft and two hard boundaries, operated near the cut-off frequency. **(a)** Calculated transmission phase and amplitude. The design parameters are similar to the experimental setup, with only the length being modified ($a = 0.225$ m, $b = 0.382$ m, and $d = 12.6$ mm). **(b)** Phase distribution through the CNZ channel near the first cut off frequency for different lengths. $f_{\text{tunneling}}(\text{i}) = 763.0$ Hz, $f_{\text{tunneling}}(\text{ii}) = 763.3$ Hz, $f_{\text{tunneling}}(\text{iii}) = 764.9$ Hz. **(c)** Spatial variation of phase at the CNZ tunneling frequency for waveguides with 90° and 180° bends. We observe uniform phase despite bending of the channel. Here, $f_{\text{tunneling_}90}(\text{i}) = 755.10$ Hz, $f_{\text{tunneling_}180}(\text{ii}) = 756.52$ Hz.....42

Figure 10. Waveguides with hard boundary walls, operated near the higher-order $(2,0)$ mode cut-off of the intermediate channel. We can see that the higher-order mode matches the phase pattern of a soft-hard $(1,0)$ mode (from Figure 9) in the center of the channel. This presents an “*effective soft boundary*” along the planes where the phase flips by π . This flip results from a change in sign of the pressure, which is a purely real-valued standing wave. **(a)** Numerical results for transmission phase and amplitude. The design parameters are similar to the experimental setup, with only the length being modified ($a = 0.450$ m, $b = 0.382$ m, and $d = 12.6$ mm). **(b)** Phase distribution through the CNZ channel near the $(2,0)$ cut-off frequency for hard-hard configurations of different lengths. For bottom figure: $f_{\text{tunneling}}(\text{i}) = 762.9$ Hz, $f_{\text{tunneling}}(\text{ii}) = 763.4$ Hz, $f_{\text{tunneling}}(\text{iii}) = 764.8$ Hz. **(c)** Spatial variation of phase at the CNZ tunneling frequency under 90° and 180° bends. Here, $a = 0.450$ m, $b = 0.382$ m, $f_{\text{tunneling_}90}(\text{i}) = 764.40$ Hz, $f_{\text{tunneling_}180}(\text{ii}) = 757.38$ Hz.46

Figure 11. Experimental measurements and numerical results for supercoupling channel. (a) Numerical and experimental comparison for the transmission phase and amplitude. Radiation and material loss from the intermediate channel were modeled using elastic shell boundary conditions with a loss tangent of 0.05. Note that curve (ii), in green, shows the transmission amplitude at the tunneling frequency (~ 765 Hz) is much higher than the others, due to the use of thicker walls for the intermediate channel. The experimental parameters were $a = 0.450$ m, $b = 0.382$ m, and $d = 12.6$ mm. (b) Spatial phase distribution through the CNZ channel at the tunneling frequency for configurations with different lengths and $f_{\text{tunneling}}$ (i) = 769.6 Hz, $f_{\text{tunneling}}$ (ii) = 769.6 Hz, $f_{\text{tunneling}}$ (iii) = 769.4 Hz.....48

Figure 12. Arbitrarily shaped acoustic power divider formed by an intermediate channel with near-zero compressibility. Material property of the channel results in a quasistatic acoustic field, having uniform pressure everywhere. When channels meet the matching conditions derived in the text, the input power is fully transmitted and equally split among the outputs.....55

Figure 13. Geometrical configuration and phase distribution of the uniform-phase equal-amplitude acoustic power divider (inset-bottom-right). The system is composed of hard-walled cylindrical waveguides for the input (port #1) and outputs (port #2-#4), connected to an intermediate hard-walled channel with rectangular cross section. Operated at its second cut-off frequency, the intermediate channel performs as an effective CNZ medium and results in uniform-phase output signals. Moreover, equal cross-sectional areas of the output waveguides results in equal distribution of output power among them **(a)** Power transmission coefficient and phase show that the power is divided evenly ($S_{j1} = 0.25$ where $j \in 2,4$) with equal phase among three output ports at the CNZ frequency of 763 Hz. **(b)** Power reflection coefficient reveals that we observe nonzero reflection at the input port ($S_{11} = 0.25$ at 763 Hz) and therefore not all of the power is transmitted. **(c)** Power transmission coefficient and phase of the power divider from (a), but modified such that the cross-sectional area of the input waveguide is equal to the sum of the cross-sectional areas of the output waveguides ($r_i = 6.3$ mm, $r_o = 6.3/3$ mm). The input signal is split evenly ($S_{j1} = 1/3$) and with the same phase among the three output ports at the CNZ frequency of 763 Hz. **(d)** The reflected power at the CNZ frequency has now been completely suppressed due to the matching condition, dictated by Eq. (3.23). **(e)** Spatial phase distribution at the CNZ frequency, showing the uniformity of the phase of the delivered output signals and the geometrical parameters **(f)** Spatial phase distribution for the higher-order mode at 773 Hz. The dimensions of the CNZ channel are $a =$

0.450 m, $b = 0.382$ m and $L = 1.5$ m . The radius of the input/output channels are $r_i = r_o = 6.3$ mm.....60

Figure 14. Matching condition for the input/output waveguides in the power divider, Eq. (3.23), is met with unequal cross-sectional areas at each output, which allows zero reflection at the input as well as control over the power supplied to each output port. The geometrical parameters of the power divider are similar to Figure 13(e) except for the cross-sectional areas of each input/output waveguide, which are indicated by the proportionally-scaled insets in all plots ($r_i = 6.3$ mm, $r_{o2} = 6.3/6$ mm, $r_{o3} = 6.3/3$ mm, $r_{o4} = 6.3/2$ mm). **(a)** As the matching condition of Eq. (3.23) is satisfied, the reflected power remains zero at the CNZ frequency of 763 Hz. **(b)** The cross-sectional area of the second output port is $A_2 = A_{in}/6$ and the output power is $S_{212} = 1/6$. **(c)** $A_3 = A_{in}/3$ and $S_{312} = 1/3$. **(d)** $A_4 = A_{in}/2$ and $S_{412} = 1/2$63

Figure 15. The geometrical parameters of the power divider are kept identical to Figure 13(e), except that the output ports #2 and #3 are placed along the side of the intermediate channel, while port #4 is placed at the end (see spatial phase profile, top-right inset). **(a)** Power is evenly divided among the three output channels at the CNZ frequency of 763 HZ. **(b)** At this frequency, the phase is flipped by 180 degrees at the output of both side channels, while the phase is 0 degrees at the interface of port #4.65

Figure 16. A more general case of the uniform-phase acoustic power divider, in which the height and length of the channel are varied. This example has a total of 5 output ports (one on each opposing face of the intermediate channel). The power divider maintains uniform phase for any port placed within $\lambda/4$ of the center of the channel and the output phase flips by 180 degrees for any output waveguide that is placed elsewhere (see inset-bottom). **(a)** Power is divided evenly among the 5 output ports at the CNZ frequency of 763 Hz. The phase is zero at the CNZ frequency for ports #2, #3, and #4, and the phase is 180 degrees for ports #5 and #6. **(b)** The reflected power remains zero at the CNZ frequency. The dimensions are $a = 0.450$ m, $b = 0.6$ m and $L = 0.5$ m, $r_i = 6.3$ mm, and $r_o = 6.3/5$ mm.....67

Figure 17. Scaling limitations for the acoustic power divider. Increasing the size of the input waveguide results in a channel that no longer has uniform phase and the power division becomes uneven. **(a)** Power transmission coefficients (left axis, solid lines) and phase (right axis, dashed lines) for ports #2-#6 when the radius of the input waveguide is $a/8$, where $a = 0.450$ m is the width of the intermediate channel. Note that peak power division no longer occurs at the same frequency for each port, although the output power varies by a maximum of 11.5% in this case. The output transmission phase along the central ports ($j = 2,3,4$) has increased from zero in the previous case (Figure 16) to $\sim\pi/4$ and varies by a maximum of 0.15 rad. **(b)** Power reflection coefficient for an input waveguide radius of $a/8$, which has been degraded to 0.03 (compared to the 0 power reflection coefficient of Figure 16) **(c)** Variation of the CNZ frequency for a hard-hard channel (where uniform-phase power division can be achieved) as a function of the width of the channel, a . **(d)** Visco-thermal acoustic boundary layer loss as a function of frequency and waveguide radius. The black curve represents the limit where input radius reaches to $a/8$. Below the black curve, all choices of radius and frequency can result in power dividers with approximately uniform phase and equal power splitting. Note the units of loss are dB/cm as we are interested in centimeter-scale devices.74

Figure 18. Overview of a single-transducer STAR acoustic system.80

Figure 19. Comparison of analog approaches to self-interference cancellation for acoustic measurement systems. The diagram in (a) is similar to the circuit first proposed for acoustics in [90] and further studied in [22], [71], [86], [88], [91] while the system in (b) is similar to the one proposed for ultrasonic applications in [24] and further studied in [97]–[104].81

Figure 20. (a) Linear circuit model of the general impedance-matched bridge circuit for an acoustic transducer, which assumes that the real part of the bridge circuit impedance is less than R_0 . (b) Model for when the real part of the bridge circuit impedance is greater than R_0 . For both (a) and (b), the output voltage, $v_{out} = v_2 - v_1$ will be independent of the input voltage v_{in} , given that $Z_1 / Z_p = Z_2 / Z_3$84

Figure 21. Analytical solution for the output voltage of the bridge circuit during STAR operation (solid line) overlaid with the numerical solution from National Instruments (NI) Multisim software (dashed line). (a)-(b) Magnitude and phase of v_{out} with varied matching of Z_p and Z_3 , corresponding to a mismatch in the parameters A and B such that $|A/B| = 1, 0.995$, and 0.977 . (c)-(d) Magnitude and phase of v_{out} with varied matching of Z_1 and Z_2 , which corresponds to a mismatch in the parameters A and B such that $|A/B| = 1, 1.005$, and 1.025 . Input parameters for (a)-(d) are presented in Table 3.87

Figure 22. Effect of the impedance matching layer on the sensing amplitude. **(a)** The sensed amplitude varies as $|A/B|$ gets further from its ideal value of 1. Parameters for $|A/B|=1$ are C_3/C_p and $R_3/R_p=1$; for $|A/B|=0.993$: $R_3=\infty$ (open circuit) and $C_3/C_p=1$, for $|A/B|=0.995$: are C_3/C_p and $R_3/R_p=0.99$, and for $|A/B|=0.977$: C_3/C_p and $R_3/R_p=0.95$. **(b)** Frequency dependence of the amplitude coefficient C , which is defined with Eq. (4.2).90

Figure 23 (a)-(b) Values of the SIC and SIR spectra as A and B are varied from their optimal values, where it is assumed that the piezoelectric voltage source $v_p = v_{in}/10$, and the circuit parameters are specified in Table 3. **(c)** The first and second terms in Eq. (4.2) which are used to compute the results for SIR and SIC in (a)-(b). Parameters for $|A/B|=0.999$ are C_3/C_p and $R_3/R_p=1$; for $|A/B|=0.998$: C_3/C_p and $R_3/R_p=0.998$; for $|A/B|=0.997$: C_3/C_p and $R_3/R_p=0.995$; for $|A/B|=0.995$: C_3/C_p and $R_3/R_p=0.99$; and for $|A/B|=0.99$: C_3/C_p and $R_3/R_p=0.98$ 93

Figure 24. (a)-(b) Values of the SIC and SIR spectra as A and B are varied from their optimal values, where the transducer impedance, Z_p is now represented by measured impedance values, and v_p is based on empirical results according to Eqn. (5.2). **(c)** The first and second terms in Eq. (4.2) which are used to compute the results for SIR and SIC in (a)-(b). Parameters for $|A/B|=1$ are C_3/C_p and $R_3/R_p=1$; for $|A/B|=1.001$: C_3/C_p and $R_3/R_p=0.998$; for $|A/B|=1.003$: C_3/C_p and $R_3/R_p=0.995$; for $|A/B|=1.005$: C_3/C_p and $R_3/R_p=0.99$; and for $|A/B|=1.01$: C_3/C_p and $R_3/R_p=0.98$. The circuit parameters are specified in Table 3.97

Figure 25. Reference measurement configuration for STAR measurements with an immersion transducer. **(a)** A short-duration signal is transmitted such that the signal ends before any reflection occurs, which permits easy separation of the incident and reflected signals in the time domain. **(b)** A signal with longer duration and same center frequency is transmitted such that the incident signal is still transmitting when the signal reflected from the interface reaches the transducer. In this case, the STAR system can be used to separate the incident and reflected signals in the measurement.98

Figure 26. Measurements of the complex impedance of the V318 immersion transducer compared to a parallel RC circuit model and a higher-order RLC model of a piezoelectric transducer suggested by Sherman and Butler (S&B model) [143] and reproduced in Figure 27. The S&B model consists of a series RLC circuit in parallel with a capacitance and a conductance. (a) Magnitude of the transducer impedance. (b) Real part of the transducer impedance. (c) Phase of the transducer's impedance. (d) Imaginary part of the transducer's impedance.	100
Figure 27. RLC model of a 1-dimensional piezoelectric transducer, reproduced from Figure 3.16 of [143].	101
Figure 28. (a) SLDV measurement of an air-loaded V318 transducer with 500 kHz sinusoidal excitation. (b) Pressure field in the x - z plane through on the transducer axis computed using SLDV transducer velocity data and a Fourier Acoustics solver at 500 kHz. (c) On-axis acoustic pressure along the z -axis at 500 kHz. Data is overlaid with the Fourier Acoustics (FA) prediction and the analytical result for piston with uniform velocity in rigid baffle. The data and FA prediction are in good agreement, within approximately 2 dB for all axial positions measured. (d) System function computed from measurement at $z = 10$ cm, which assumes that the V318 can be modeled as an ideal piston. The Wiener filter was computed with $\varepsilon = 0.1$ as defined in [142].	103

Figure 29. Multi-sim circuit models of the bridge circuit with measured values for the components, under configurations that consider the parasitic resistance, and various forms of balancing the real part of the impedances in the bridge. These changes impact the power delivered to the transducer through resistor R_p . The effect of parasitic resistance on power delivery can be seen by comparing the purple and red curves. It is also seen that balancing all four elements on the bridge with equal resistances results in a reduction of the delivered power to the transducer (green curve), and it was subsequently determined that this did not lead to any improvement in operating bandwidth. Parameter values for each of these configurations are reported in Table 4.	105
Figure 30. Photograph of experimental setup.	107
Figure 31. Tuning the peak SIR frequency of the STAR system. (a) Predicted SIR with Z_3 modeled as a parallel RC circuit (b) Predicted signal-to-interference plus noise ratio (SINR), where -54 dB re 1V of white noise is added to the interference signal (matching noise level in the lab measurements). (c) Predicted interference spectra (solid lines) and received voltage spectra (dot-dashed lines), for the SINR predictions of plot (b). (d) Measurements of SINR at frequencies corresponding to predictions in (b). Parameters used for these measurements are reported in Table 5.	109

Figure 32. (a) Amplitude of the residual input signal as predicted by Eq. (4.2). The solid purple curve uses nominal RLC component values and values of the measured impedance of the transducer, Z_p . The green curve uses measured values of complex impedance for all components. (b)-(c) The real and imaginary parts of the parameters A and B from Eq. (4.2). The vertical dashed line of each subfigure denotes the frequency of maximum SIC, which occurs where both the real and imaginary parts of A and B are nearly equal.111

Figure 33. Measured residual voltage amplitude and predictions from Eqn. (4.2) with values of Z_p as described in Figure 34. Predictions and measurements in plots (a)-(i) have parameters that are listed for the corresponding peak frequencies in Table 5. It can be seen that the predictions for residual amplitude are significantly more accurate when Z_p values are determined by the best-fit choice of parameters.114

Figure 34. (a)-(b) Real and imaginary parts of the measured transducer impedance, Z_p , in comparison with an effective impedance including parasitics in the bridge.....115

Figure 35. (a)-(b) Values of the real and imaginary parts of Z_3/Z_2 that result in peak SIR at each center frequency (simulated and measured), with each measurement corresponding to parameter values reported in Table 5.116

Figure 36. Extending the positive SIR bandwidth. Results are shown for a parameter sweep with a mismatch of $X_n / X_{n,0}$ by 0.2%, 0.5%, 1%, and 2%. In this notation, $n = \{1, 2, 3, 4\}$; $X_1 = C_e$; $X_2 = L_e$; $X_3 = R_e$; and $X_4 = C_0$ as defined in the S&B model of Figure 27 (with $G_0 \rightarrow \infty$). The top and bottom dashed curves represent maximum and minimum bounds on the SINR predicted by a Monte Carlo model that varied these four parameters, in addition to C_2 , by +/- 2%. All predictions assume that the noise level is -54 dB re v_{in} , which matches the noise level in the measured data. Parameters used for these predictions and measurement are reported in Table 6. **(a)** Broadband SIR with Z_3 and Z_p represented by the least-squares fit to the S&B model, as presented in Figure 34(a)-(b), with the RLC parameters comprising Z_3 being varied as described above. These are compared with a measured result having a peak frequency of 481 kHz. **(b)** Predicted SIR with Z_3 represented by the S&B model and Z_p represented by its measured impedance data, with the RLC parameters comprising Z_3 being varied as described above. These are compared with the same measurement result plotted in (a).119

Figure 37. Best fit solutions of Eq. (4.2) to the measured broadband SINR for selected tolerances on the RLC components contained within Z_3 . Here, Z_3 is represented by the S&B model of Figure 27 and $Z_2 = 1 / j\omega C_2$ is treated as an ideal capacitor. Parameters used to generate these solutions are reported in Table 7.121

Figure 38. (a) Time division measurement without STAR cancellation. In this baseline case, the signal-to-interference ratio (SIR) is -52 dB. (b) STAR measurement with a 459 kHz sinusoidal burst having a duration of 40 cycles. This achieves an SIR of 17 dB, resulting from 56 dB of self-interference cancellation (SIC) on the incident signal. The parameters were $f = 459$ kHz, $R_3 = 4558$ Ohm, $C_3 = 554$ pF, and $C_2 = 560$ pF. (c) The time domain data from (b) is convolved with a causal digital bandpass filter in Matlab. A reduction of 19 dB is observed in the transient amplitude, which results in a positive value of SIR across the entire duration of the signal.	124
Figure 39. (a) Time-division measurement with the STAR circuit (baseline). (b) Time-overlap measurement with the STAR circuit. The incident burst has a 94-cycle duration at 452 kHz, which results in approximately a 20% overlap of the first reflection and the incident signal in the time domain. (c) Time-overlap measurement with a 230-cycle period, resulting in approximately 70% overlap of the first reflection and the incident signal.	126
Figure 40. (a) Schematic of near-surface test sample. Transducer measurements are made from the bottom side of the test sample as shown at the bottom of (a). Distances to each flaw are 20 mm, 10 mm, 5 mm, 1 mm, 0.5 mm, and 0.25 mm. Lateral hole spacing was designed to be 5λ at 1 MHz. (b) Picture of the test sample, including top cover which is used to seal the sample from water.	133
Figure 41. Experimental setup for near-surface acoustic imaging with self-interference cancellation.	134

Figure 42. Normalized doppler shift plotted against the angle of the transducer from the blood vessel.....136

Figure 43. (a) Bi-static doppler measurement system that measures the velocity of a moving scatterer in a direction normal to the plane connecting the transducers. **(b)** Blind zone duration of a monostatic doppler measurement system for three different fluid materials. **(c)** Ratio of the bi-static blind zone duration to the monostatic blind-zone duration, in the absence of any directivity for the TX and RX transducers.....139

Chapter I: Introduction

1.1 OBJECTIVE AND MOTIVATION

The principal objective of this dissertation is to determine with analytical, numerical, and experimental investigations the feasibility of extraordinary acoustic transmission phenomena, such as membrane-free acoustic supercoupling and acoustic self-interference cancellation.

Since at least 500 B.C., as early as Pythagoras, people have studied the propagation of sound. Initial curiosity was mainly driven by the study of musical sounds and their propagation in ancient theatres [1]. Acoustic propagation was later described more systematically and in more general terms by physicists such as Newton, Galilei, and Rayleigh [2]. In modern times, more than 100 years after Rayleigh, the maturity of the field of acoustics might lead one to believe that fundamental concepts, such as physical descriptions of the transmission of sound, are bound by models established in the classic literature. For example, one might think of such canonical problems as plane wave transmission through a material with finite thickness, propagation through a uniform waveguide, or reflection and transmission from a Helmholtz resonator, as concepts that place bounds on the kinds of behaviors that we can expect from sound transmission. After all, these fundamental problems significantly impacted acoustical engineering, serving as examples to guide the design of acoustical panels (e.g. architectural acoustics), to study atmospheric and underwater sound propagation and sensing, and to develop applications

in sound absorption and passive amplification (e.g. acoustic loudspeaker and microphone design) [3].

While these fundamental concepts have been central to the study of acoustics since the late nineteenth century, a key contribution in 1968 transformed the way we think about waves interacting with materials. This was when Veselago first described a material that could possess a negative electromagnetic refractive index [4]. His finding implied that wave transmission into a negative index medium from air or vacuum would result in the transmitted wave bending *away* from the normal to the interface between the two media; in other words, the wave bends in a direction opposite to that typically observed for common media that possess positive refractive indices. This contribution gave rise to the field of metamaterials, which studies extraordinary wave phenomena that are generally considered impossible in classic wave physics literature, due to the previously assumed bounds on material properties.

Although the first description of negative index propagation occurred over three decades prior, it was not until the year 2000 when the field of metamaterials accelerated with the first experimental confirmation of negative index material properties [5], the proposal of a perfect lens using metamaterials [6], and the later development of analogous ideas from electromagnetics into acoustics [7]–[10].

Within metamaterial research, one widely influential topic has been the idea of near-zero-index materials, in which the effective permittivity and/or permeability approaches zero in electromagnetic materials, and the effective density and/or compressibility approaches zero in acoustic materials. It was first shown that an

electromagnetic wave in a narrow channel containing a permittivity near zero material (i.e. epsilon-near-zero or ENZ) can display extraordinary transmission properties, such as uniform phase (infinite wavelength), independent of the length of the coupling channel, as well as impedance matching with external channels that are greatly mismatched, thereby allowing full power transmission through all channels [11]. These remarkable properties inspired the development of numerous concepts and devices that were proposed for wave manipulation, including analogous implementations demonstrating supercoupling for acoustic waves (see Chapter 2).

Several demonstrations of supercoupling in electromagnetics were achieved without having to realize a metamaterial through periodic arrays of small inclusions, but simply operating a hollow waveguide at cut-off [12]–[15]. In comparison, an additional challenge arises in acoustics, due to the fact that conventional acoustic waveguides do not support a cut-off for the dominant mode of propagation, and therefore zero-index can be achieved only based on a collective resonance of the loading elements. In the present work, however, it was shown that it is possible to realize acoustic supercoupling in a hollow waveguide by exciting a higher-order mode at cut-off, providing an experimentally viable, simple geometry demonstrating effective zero compressibility and supercoupling for sound.

Similar to supercoupling, recent attention has been paid to coupled resonator systems that demonstrate extraordinary transmission via nonreciprocity, leveraging effective material properties through spatiotemporal modulation or moving media (bias flow) [16]–[20]. These advances led to proposals of compact acoustic circulators [16],[17],

which showed a behavior that mimicked the popular RF devices of the same name. Circulators are commonly used in applications such as RF communications and radar [21], in order to isolate sensitive receiver hardware from the high-powered output of a transmitter, while still interfacing with the same antenna. Although the acoustic circulator was a major conceptual leap in the field of acoustic metamaterials, there are still fundamental limitations when it comes to implementation in a practical device: limited bandwidth and frequency of operation with respect to the physical size of the device, and difficulties in fabrication of resonant cavities that exhibit time-modulated compressibility or density.

Moreover, implementation of an acoustic circulator into a practical measurement system poses another challenge: the acoustic circulator itself must act as the “acoustic antenna”, i.e., the circulator must interface with a passive structure (such as a waveguide) in order to transmit or receive the acoustic energy to/from the propagating field. This is in contrast with typical acoustic measurement systems, in which the electroacoustic transducer acts as the “antenna”, such that the transducer is the first part of the system that interfaces with the wave field. However, when used with an acoustic circulator, a transducer cannot act at the first interface with the wave field, because in that case the acoustic wave would already be transduced into an electrical signal, and therefore the acoustic circulator could no longer be used. The challenge is that any passive acoustic wave interface that is used in conjunction with an acoustic circulator represents an additional layer in the system design (as compared to a traditional acoustic transceiver) and would generally cause increased reflection loss and transmission loss in the overall system.

Given that many effective tools already exist for the manipulation and isolation of signals in the electrical domain, it is the goal of this work to examine whether existing electrical components could be used to effectively isolate acoustical signals after they have been transduced to electrical signals. Specifically, inspiration was taken from prior works that explored in-band full duplex (IBFD) [22], simultaneous transmit and receive (STAR) [23], and self-sensing actuators (SSA) [24], in the domains of Radio Frequency (RF) communications, WiFi, acoustics, and vibration control. While the methodologies used for cancelling self-interfering signals in these varied domains have common features, such as analog-only, digital-only, or hybrid analog-digital system designs, the implementations differ greatly. The chief differences in self-interference cancellation (SIC) approaches stem from 1) the varied responses of the transmitting elements, whether they be RF antennas or electromechanical transducers, including their frequency responses, noise floor, and nonlinear behavior, and 2) the modality of signal processing, depending upon the required frequency content, duration, amplitudes, and propagation dynamics.

Relatively few prior works have investigated applicability of SIC systems (often referred to as STAR, IBFD, or SSA systems) to problems in acoustics, where the frequencies of interest typically span from low audio (~ 20 Hz) up to high ultrasonic frequencies (~ 20 MHz), and where the potential applications for SIC are numerous and enticing. In this dissertation, SIC in acoustic measurement systems is investigated both theoretically and experimentally, and it is shown that SIC of greater than 55 dB can be achieved with an all-passive STAR system at ultrasonic frequencies.

1.2 HYPOTHESIS AND STRATEGY

The principal objective of this dissertation can be satisfied by dividing the objectives into two separate hypotheses. The acceptance of both of these hypotheses will then equate to satisfaction of the principal objective. Both hypotheses relate to different portions of the investigation into extraordinary acoustic transmission phenomena.

Hypothesis 1: Analytical and numerical modeling, combined with experimental validation, can be developed to demonstrate the feasibility of membrane-free acoustic supercoupling.

Hypothesis 2: The viability of simultaneous transmit and receive (STAR) functionality for ultrasonic measurement systems can be proven through the introduction of system modeling of self-interference cancellation, transduction, and acoustic propagation, and by experimentally validating these models.

Hypothesis 1 is accepted through the validation of a physical model of supercoupling that employs transmission line theory, alongside a full-wave finite element model. Both models consider ideal hard and soft acoustic boundaries, while the finite element model also includes consideration of radiation loss due to the finite thickness of material on the boundaries of the resonator. The acceptance is further strengthened by the demonstration of membrane-free compressibility-near-zero supercoupling for use as an acoustic power divider. *Hypothesis 2* is accepted through the development and validation of an all-passive approach to self-interference cancellation of acoustic signals in the electrical domain. System models describe key parameters that determine system performance and analysis is presented to explain accuracy requirements for the values of the components used in the

cancellation circuit. The proposed simultaneous transmit and receive (STAR) system is validated through experimental investigation with an ultrasonic measurement system that demonstrated up to 55 dB of SIC. The experiment demonstrated successful measurement of same-frequency signals that are received by a single ultrasonic transducer that is actively transmitting simultaneously. An overview of discussions in the following chapters and a breakdown of the principal research question is presented in Table 1.

Table 1. Overview of research plan.

Principal Research Question: Can analytical, numerical, and experimental investigations prove the feasibility of extraordinary acoustic transmission phenomena such as membrane-free acoustic supercoupling and acoustic self-interference cancellation?					
Questions	Can a physical model be developed to demonstrate supercoupling in a membrane-free acoustic medium, analogous to supercoupling phenomena observed in electromagnetics?	Given the implementation of acoustic supercoupling, could such principles be employed to develop a practical device for sensing or measurement?	Can a self-interfering acoustic signal be cancelled in the electronic domain to enable simultaneous transmit and receive at ultrasonic frequencies?	Can a STAR acoustic system be modeled to accurately predict performance of acoustic measurements during STAR operation?	Can STAR operation in an acoustic measurement system be demonstrated experimentally?
Answers	Yes. By constructing a coupled resonator geometry that takes advantage of a compressibility-near-zero (CNZ) condition, it is possible to observe acoustic supercoupling without the presence of membranes.	Yes. Principles from the CNZ supercoupling model were extended to develop an acoustic power divider that demonstrates uniform phase and full-power transmission.	Yes. Using a system that extends bridge circuit topology that was originally developed for vibration control, it was shown that this is possible for ultrasonic measurement systems.	Yes. Circuit models were combined with a Fourier Acoustics approach that enables inclusion of measured surface velocity data into the propagation model.	Yes. An immersion transducer used for ultrasonic nondestructive evaluation (NDE) was employed in proof-of-concept experiments and demonstrated greater than 55 dB of SIC at a tunable center frequency.
Location	Chapter III	Chapter III	Chapter IV Chapter V	Chapter IV	Chapter V

1.3 DISSERTATION OVERVIEW

This dissertation is divided into six chapters. **Chapter II** presents a detailed technical introduction to summarize background works regarding supercoupling and self-interference cancellation. Prior work in electromagnetics, including Radio Frequency (RF), microwave, and WiFi systems, are compared to analogous efforts in acoustics and vibration research. The prior art summarized in this chapter form a foundation for the technical contributions presented in Chapters III-V. Chapter II concludes with an overview of potential applications for simultaneous transmit and receive (STAR) in acoustic measurement systems.

Chapter III presents a device concept demonstrating membrane-free acoustic supercoupling. Analytical models are compared with numerical simulations and experimental validation at audio frequencies. Subsequently, an application of acoustic supercoupling is proposed as an acoustic power divider, which demonstrates remarkable properties such as full power coupling, with uniform phase, independent of the length of the coupling channel. Analytical and numerical models of the supercoupling power divider are presented and the chapter concludes with a discussion of scalability, including considerations of visco-thermal acoustic boundary layer loss as the device size is decreased.

In **Chapter IV**, an approach is proposed for cancellation of self-interfering acoustic signals in the electronic domain using all-passive analog circuit elements. This approach is compared with a commonly used alternative method that employs active elements in the

cancellation process. An analytical solution for the model is presented and validated with numerical simulation results. Predictions are described for the overall performance of the passive cancellation system, in terms of figures of merit such as self-interference cancellation (SIC) and the signal-to-interference ratio (SIR).

Chapter V describes an experimental plan for validation of the theoretical predictions of Chapter IV. The measurement setup is described, and the components used are characterized in terms of their complex impedances as a function of frequency. The acoustic output of the transducer is measured to validate propagation models used in theoretical predictions. The SIC and SIR are predicted using the measured values of all components in the lab and compared with theoretical results of Chapter IV. Measurements are presented that validate the model prediction of positive SIR across a wide range of frequencies around the resonance frequency of the acoustic transducer, which is tunable given the choice of component values in the circuit. A concept for extending the bandwidth of the positive SIC and SIR is presented and tested experimentally. Finally, timeseries measurements are presented to demonstrate the operation of a single acoustic transducer that is simultaneously transmitting and receiving at the same frequency.

Finally, **Chapter VI** summarizes the findings and contributions of the previous chapters and considers the limitations and advantages discovered during these investigations. A discussion is presented regarding the outlook of future development and application of the extraordinary acoustic transmission phenomena presented in previous chapters.

Chapter II: Principles of Supercoupling and Self-Interference Cancellation

In this chapter, we present an overview of the fundamental developments, technical background, and physical principles in the study of supercoupling and self-interference cancellation (SIC). In Section 2.1, we will explain how supercoupling is enabled by zero-index metamaterials, which can be described by governing equations that are temporally and spatially decoupled, due to the unusual physics permitted by near-zero constitutive parameters. This chapter will provide a foundation and context for the topic of Chapter III, compressibility-near-zero acoustic supercoupling. Section 2.2 will cover various approaches for cancelling self-interfering signals in systems that transmit and receive electromagnetic, vibrational, and acoustical waves. This section will provide a foundation for the contributions presented in Chapters IV-V. Finally, opportunities for the development and application of self-interference cancellation in acoustic systems will be outlined to serve as further motivation for this work.

2.1 SUPERCOUPLING

2.1.1 Development and Principles of Supercoupling

Over the past decade, significant attention has been paid to zero-index metamaterials, due their extreme capabilities for wave manipulation [25]. Zero-index material properties have led to peculiar scattering and propagation phenomena, such as the transformation of curved wave fronts into planar ones [26], and the ability to tailor the radiation phase pattern from arbitrary sources [27]. The vast majority of this research has been focused in the electromagnetic domain, including media with near-zero dielectric

permittivity, ϵ , (known as epsilon-near-zero or ENZ materials) [12]–[15], [26]–[36], near-zero magnetic permeability, μ , (known as mu-near-zero or MNZ materials) [37] or double-near-zero materials (epsilon-and-mu-near-zero or EMNZ) [38],[39]. Recent attention has also been given to analogous phenomena in the field of acoustics [40]–[47], which is reviewed below.

To understand how zero-index behavior arises in these materials, consider the expression for the phase velocity of an electromagnetic wave in free space [48]:

$$c_{\text{ph}} = \frac{1}{\sqrt{\mu\epsilon}} \quad (2.1)$$

Here we can see that if either $\epsilon \rightarrow 0$ or $\mu \rightarrow 0$, then $c_{\text{ph}} \rightarrow \infty$, and given that $\lambda = c_{\text{ph}} / f$, it is implied that $\lambda \rightarrow \infty$ for nonzero frequencies [49]. Metamaterials can achieve this type of wave behavior through *effective* material properties, meaning that the macroscopic behavior of the material will result in a bulk material property, such as ϵ or μ , that differs from that of any individual constitutive elements or inclusions. It should be noted that c_{ph} is distinct from the information rate, so the result $c_{\text{ph}} \rightarrow \infty$ does not violate causality [50], and that $\lambda \rightarrow \infty$ simply implies that the collective wave oscillation has a uniform phase throughout the zero-index medium (in the time-harmonic solution). When considering acoustic waves, an analogous expression can be derived for the acoustic phase velocity in free space [3]:

$$c_{\text{ph}} = \frac{1}{\sqrt{C\rho}} \quad (2.2)$$

In this formula, C represents compressibility (equal to $1/B$, where B is the bulk modulus), and ρ is the density of the fluid medium in which the acoustic wave propagates.

Here the analogy with electromagnetics can be seen, as we similarly have $c_{\text{ph}} \rightarrow \infty$ with either $C \rightarrow 0$ (compressibility-near-zero or CNZ) or $\rho \rightarrow 0$ (density-near-zero or DNZ).

2.1.2 Review of Zero-Index Electromagnetics and Electromagnetic Supercoupling

Remarkable behaviors of zero-index metamaterials have been described and experimentally validated. For instance, Alù and Engheta showed that a lossless metamaterial coating could be used for cloaking spherical and cylindrical objects [51],[52] and it was later shown by Hao *et al.* [53] and Ma *et al.* [54] that cloaking can be achieved with metamaterial coatings consisting of zero-index layers. Enoch *et al.* demonstrated theoretically and experimentally that a metamaterial can be designed to improve the directivity of a radiating antenna [55], a concept which was developed using zero-index media by Ziolkowski [26], and then later extended by Yu *et al.* [56]. Alù *et al.* showed that zero-index metamaterials can be leveraged to tailor the radiation pattern from arbitrary electromagnetic sources [27]. Ma *et al.* showed that anisotropic zero-index materials can be engineered to exhibit total transmission and total reflection on opposing sides of a rectangular slab [57].

With regard to supercoupling, Silveirinha and Engheta revealed that supercoupling can enable electromagnetic waves to tunnel through narrow channels filled with zero-permittivity materials, regardless of their geometrical shape and bending [14], [34], which was soon experimentally verified by Liu *et al.* [32] and Edwards *et al.* [13]. This concept is demonstrated in Figure 1(a). Later, Nguyen *et al.* demonstrated that zero-index media can be used for enhancing the transmission through channels containing dielectric defects [11], which was further extended by Xu and Chen [33]. The phenomenon was described through transmission-line theory by Alù *et al.* [15], explaining that supercoupling results

from the compensation of the large geometric mismatch between different waveguide sections with the extreme impedance values in zero-index metamaterials, which is demonstrated in Figure 1(b), while the power transmission of the metamaterial waveguide is shown in Figure 1(c). Furthermore, ENZ supercoupling has been also proposed at higher frequencies as an effective way to boost optical nonlinearities in plasmonic channels [29] (Argyropoulos *et al.*) and the local density of states and quantum super-radiance [58] (Alù and Engheta). The dual phenomenon, tunneling through a geometrically mismatched large channel filled with permeability-near-zero (MNZ) materials was also theoretically proposed [37] by Marcos *et al.* and is displayed in Figure 1(d). MNZ supercoupling was then experimentally verified for radio-frequency waves by Ma *et al* [54].

In terms of overall impact, developments in zero-index electromagnetic metamaterials have the potential to improve useful technologies that are omnipresent in everyday life. For example, telecommunication systems such as cell phone or satellite antennas could see improved data rates or reduced information loss, as a result of greater directivity and/or tailored propagation patterns enabled by near-zero index metamaterials. Furthermore, supercoupling can lead to a more versatile design space for guided-wave systems, such as power dividers (as discussed below), leveraging the potential of length-independent and uniform phase power coupling. These concepts could lead to increased capability for wave sensing and multiplexing, as compared to traditional guided wave structures.

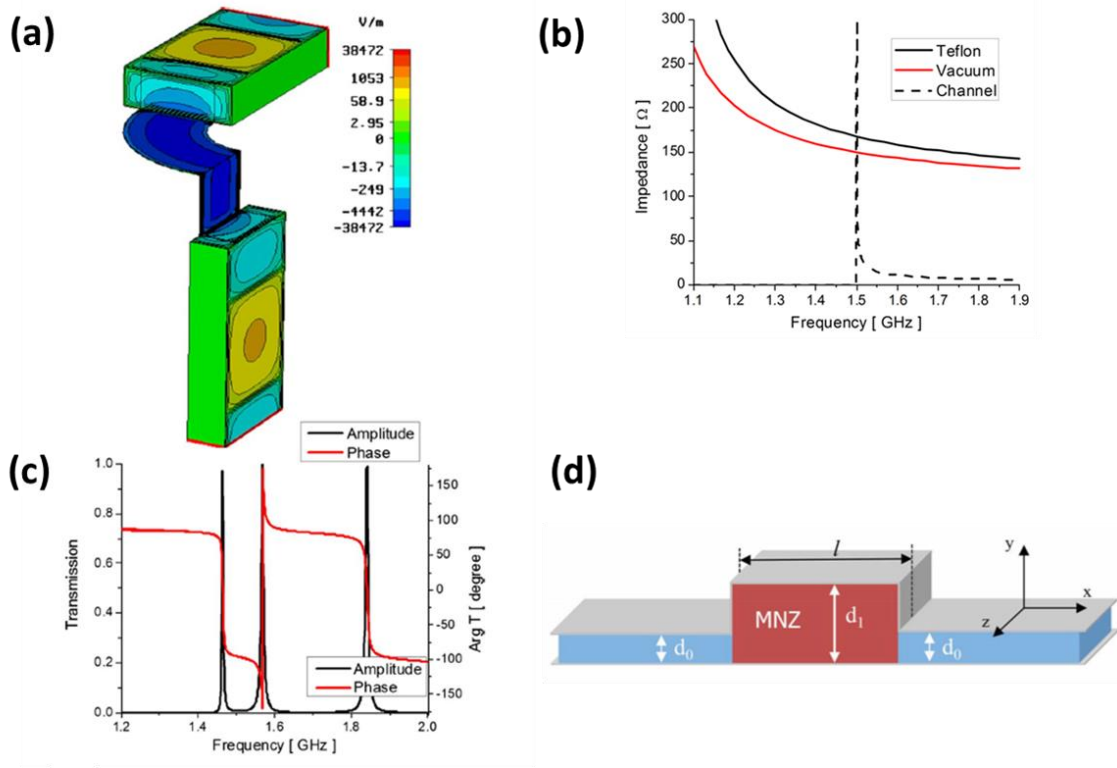


Figure 1. (a) Geometry and electric field distribution through an epsilon-near-zero (ENZ) supercoupler with arbitrary bends in the coupling channel. Adapted from [15]. (b) Plot of the wave impedance as a function of frequency, which demonstrates that channels filled with mismatched materials can be matched to the impedance of a supercoupler at the ENZ frequency, which is 1.5 GHz in this case. Adapted from [28]. (c) Amplitude and phase of transmission through an electromagnetic supercoupler. Adapted from [15]. (d) Diagram of a mu-near-zero (MNZ) supercoupler. Adapted from [37].

2.1.3 Review of Zero-Index Acoustic Metamaterials and Acoustic Supercoupling

Advances on the topic of supercoupling in the electromagnetic domain have motivated recent interest in exploring the physics of acoustic metamaterials with near-zero material properties. An early example was provided by Liang and Li who employed a space-coiled structure to create a density-near-zero (DNZ) material to achieve acoustic tunneling [41], as shown in Figure 2(a). Fleury and Alù demonstrated another approach, which theoretically showed that energy could be squeezed through ultranarrow acoustic

channels by employing a waveguide filled with arrays of transverse membranes [45], as shown in Figure 2(b), thus realizing an effective DNZ ultranarrow channel. Power transmission spectrum of the DNZ channel is shown in Figure 2(c). Naify *et al.* reported the first realization of an acoustic leaky wave antenna that could exhibit a negative, zero, or positive refractive index, depending upon the excitation frequency [40], which is displayed in Figure 2(d). Esfahlani and colleagues employed a waveguide populated with transverse membranes and side holes, to generate density-and-compressibility-near-zero behavior within an air-filled acoustic waveguide to create an acoustic leaky-wave antenna with broadside radiation [42],[43]. Around the same time, Naify *et al.* proposed an alternative design for a compact acoustic metamaterial waveguide to generate topologically diverse acoustic vortex waves [46]. Additionally, Ying *et al.* proposed a membrane-based acoustic metamaterial with near-zero-density as an angular filter that only transmits waves with near-zero incident angle [44]. More recently, Broadman *et al.* adapted metamaterial waveguide concepts to consider elastic effects that are important for underwater acoustic applications [47]. Cselyuska *et al.* described a waveguide loaded with Helmholtz resonators in the form of low-pass filters was shown to support compressibility-near-zero properties and uniform phase through an intermediate channel [59].

2.1.4 Principles and Realization of Acoustic Supercoupling

To understand how near-zero metamaterial properties have been realized in acoustics so far, consider the definitions of the effective dynamic mass density and the effective dynamic bulk modulus of a heterogenous fluid. Effective dynamic mass density is defined through the linearized momentum equation for a fluid, $\vec{m}(\vec{x}, t) = \rho(\vec{x}, t)\vec{u}(\vec{x}, t)$, where $\vec{m}(\vec{x}, t)$ is the local momentum, $\rho(\vec{x}, t)$ is the local mass density, and $\vec{u}(\vec{x}, t)$ is the particle velocity. The effective dynamic density is defined as

$$\rho_{\text{eff}} = \langle \vec{m} \rangle / \langle \vec{u} \rangle \quad (2.3)$$

where $\langle \rangle$ denotes the spatial average of each parameter [60]. The effective density of a heterogenous acoustic metamaterial has been found to become negative or near-zero (within a limited range of frequencies) when an acoustic waveguide is loaded with periodic elastic membranes, which act as series compliances that result in dynamic manipulation of the momentum within the structure [45],[49]. An alternative method for realizing DNZ coupling was proposed using space-coiled structures as metamaterial inclusions [41]. However, experimental realizations of these concepts for acoustic supercoupling have so far been impeded by challenges with visco-thermal loss and the accurate tuning of multiple membrane resonances.

Similarly, the effective dynamic bulk modulus is defined through its relationship with pressure and volume strain in the fluid as $p(x, t) = -B(x, t)\varepsilon_v(x, t)$ where $p = p(x, t)$ is the local acoustic pressure and $\varepsilon_v = \varepsilon_v(x, t)$ is the volume strain. The effective dynamic bulk modulus is that results is

$$B_{\text{eff}} = -\langle p \rangle / \langle \varepsilon_v \rangle \quad (2.4)$$

where, as with the effective dynamic density, B_{eff} is the defined in terms of the spatial average of the acoustic field quantities, which depend upon the particular structure and material properties of the heterogeneous metamaterial¹. Thus far, the realization of such properties have typically been implemented by periodic arrangements of resonant cavities, such as Helmholtz resonators [49], [59], however implementation of this approach in a

¹ $C_{\text{eff}} = 1 / B_{\text{eff}}$, where C_{eff} is the effective dynamic compressibility of the fluid.

supercoupling experiment would require extreme precision in the realization of these arrays of resonators.

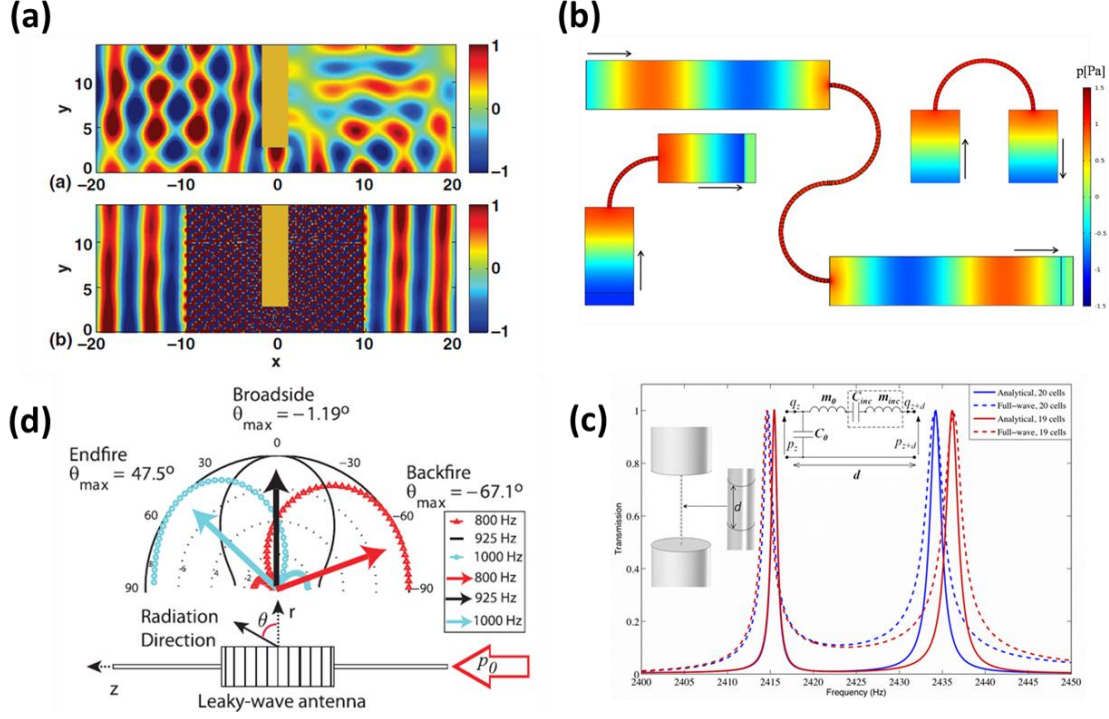


Figure 2. (a) DNZ tunneling around a sharp bend formed by a sound hard boundary, using a space-coiled metamaterial structure. Adapted from [41]. (b) Acoustic pressure of density-near-zero (DNZ) acoustic supercoupling through ultranarrow channels with arbitrary bending and channel lengths. Adapted from [45]. (c) Energy transmission coefficient of a DNZ structure from (b), which shows full power transmission at the frequency where the channel exhibits DNZ material properties for two different channel lengths. Adapted from [45]. (d) Acoustic leaky wave antenna, which radiates from endfire to backfire depending upon the frequency of excitation. The waveguide exhibits DNZ properties at the frequency which corresponds to broadside radiation, due to the response of the acoustically loaded membranes. Adapted from [40].

A big advantage that has enabled the realization of supercoupling in electromagnetics has been the fact that conducting waveguides naturally support effective zero-index properties at the cut-off of their leading-order mode of propagation. This phenomenon has enabled several demonstrations of supercoupling in electromagnetics

without having to realize a metamaterial through periodic arrays of sub-wavelength inclusions, but simply operating a hollow waveguide at cut-off [12]–[15]. Unfortunately, conventional acoustic waveguides typically do not have cut-off for their leading-order propagating mode, as these modes are longitudinal in nature. However, Chapter III of the present work will show that it is possible to realize acoustic supercoupling in a hollow waveguide by exciting a higher-order mode at cut-off, providing an experimentally viable, simple geometry that demonstrates effective zero compressibility and supercoupling for sound. Despite the use of simple materials with physically hard boundaries, the excitation of a higher-order mode is shown to synthesize effective soft-boundary waveguide channels that support a cut-off at finite frequency, and therefore enable this unusual tunneling phenomenon. This approach establishes new pathways for extreme acoustic metamaterials, cloaking, acoustic sensing, and wave patterning.

2.1.5 Supercoupling Power Dividers

Numerous applications for acoustic and electromagnetic supercoupling have been proposed and experimentally validated, such as increasing the directivity of a radiating body [55], realizing a monopolar electromagnetic antenna [61], an acoustic leaky-wave antenna with broadside radiation [42],[43], an electromagnetic N -port series power divider [62]–[65] and general impedance matching [66]. Among the proposed applications, the N -port series power divider is of interest in both microwave and acoustical engineering, because power dividers are useful for dividing signals between amplifier chains, for feeding networks in arrays, and for the distribution of signals to multiplexed subsystems [62]. Power dividers, as an essential part of the feeding network, are classified in three different categories: parallel, series and hybrid (parallel-series), each having their own advantages, disadvantages and specific applications [67]. For example, the use of antenna

arrays with equal amplitude/phase excitation, presenting a main radiation beam at broadside, is popular in communication systems.

Similar to electromagnetics, three types of feeding networks (parallel, series or hybrid) can be employed to divide acoustic power. Series power dividers are preferred when we deal with a limited physical space, because parallel-divider-based networks are usually bulky due to the three-port geometry [62]. In a series feed network, meander lines are typically leveraged to ensure that each radiating element is fed with an equal amplitude and equal phase signal. Hence, there is a cumbersome requirement that the signal is sampled from the meander feed line at locations that are integer multiples of the guided wavelength [63], as can be seen by comparison of Figure 3(a) and Figure 3(b). Therefore, although series power dividers have many advantages, they also have drawbacks such as additional design complexity, restrictions imposed upon the placement of elements in the array, and they must be custom tailored according to the number of elements [64]. These drawbacks have been addressed by Lai *et al.* with their zero-index implementation of an electromagnetic power divider [62], as shown in Figure 3(c). In terms of acoustic devices, it has been long known that a tube containing a branched conduit, referred to as a Herschel-Quincke tube and shown in Figure 3(d), can be used to filter acoustical signals in an acoustic duct or waveguide by constructive and destructive interference at the output of the conduit [68],[69]. A more recent example of a passive acoustic power divider is a rat-race coupler, which takes advantage of interference from a ring resonator to achieve equal power division between two output channels while isolating transmission to a third channel [70], as displayed in Figure 3(e).

Near-zero index media provide interesting opportunities in this context, because their largely stretched wavelength ensures phase uniformity over long distances, and hence another type of series power divider can be envisioned in which the aforementioned

drawbacks can be overcome and significant size reductions compared to meander line series power dividers may be achieved. In the later portion of Chapter III, the design of an acoustic power divider relying on compressibility-near-zero (CNZ) media is explored. Analytical and numerical models are developed to prove and support these concepts. An N -port series power divider is then shown to support operation with several ports arbitrarily positioned, ensuring equal amplitude and phase power division. The divider may be also configured to divide the signal with a phase flip of π radians, alongside with equi-phase output ports. Finally, an analysis of practical trade-offs due to losses is presented within a broader discussion on the scalability of the proposed device.

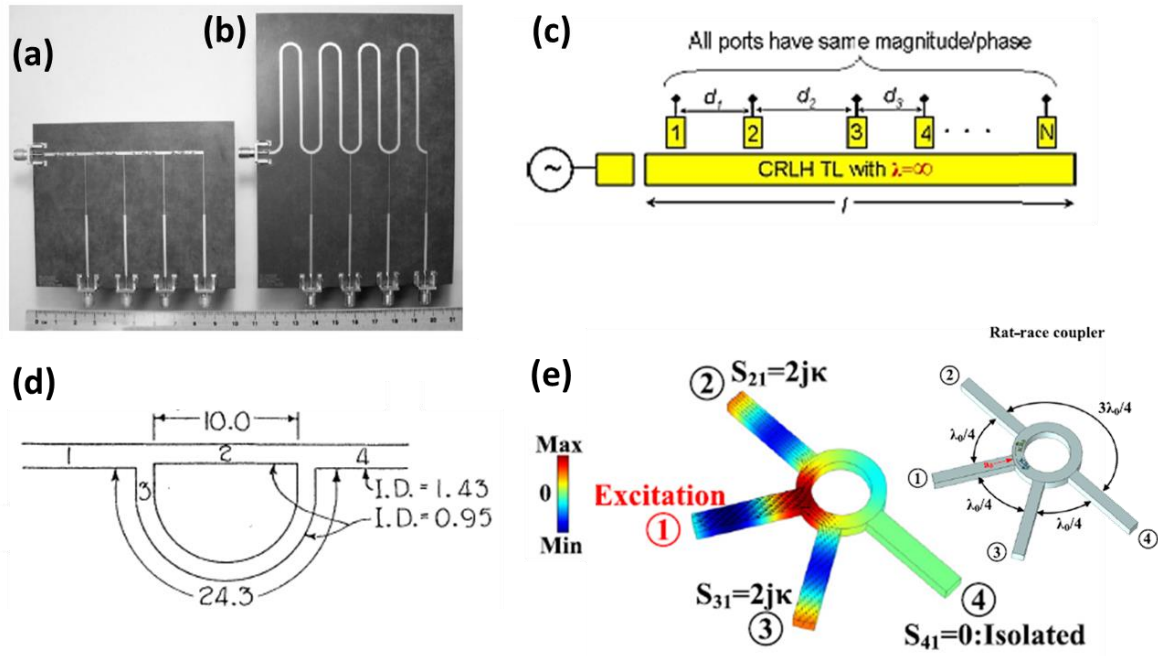


Figure 3. Examples of network devices and power dividers in electromagnetics and acoustics, which may be enhanced by metamaterial properties. (a) An electromagnetic metamaterial 1:4 series power divider that supplies equal power split among all four output ports. (b) A series power divider containing conventional one-wavelength long meander lines for in-phase signals at the output ports. (a)-(b) Both adapted from [63]. (c) An electromagnetic infinite wavelength N -port series power divider based on a composite right/left-handed (CRLH) transmission line, which exhibits near-zero index material properties at select frequencies. This power divider supports arbitrary element spacing and length, due to the infinite wavelength in the waveguide. Adapted from [62]. (d) An acoustic network device referred to as a Herschel-Quincke tube, which re-routes an incident signal from Port 1 into a main branch, 2, and a branched conduit, 3. The difference in phase between the two branches result in frequency-dependent transmission behavior at the output from Port 4. Adapted from [68]. (e) A four-port acoustic power splitter, referred to as a rat-race coupler. This passive reciprocal device couples all power from one input channel into two output channels, while isolating it from the fourth channel. Adapted from [70].

2.2 SELF-INTERFERENCE CANCELLATION (SIC)

2.2.1 Development and Principles of Self-Interference Cancellation

The possibility of sending and receiving signals at the same time and at the same frequency has recently been of significant interest in the field of radio frequency (RF) engineering to enhance spectrum efficiency and facilitate broadband wireless communications in crowded environments [22], [71]–[85]. The main obstacle to overcome in these settings is self-interference, i.e., interference between the signal received by the system and the transmitted one, which can distort or saturate the signal at the receiver. This can be overcome by a process known as self-interference cancellation (SIC), which cancels the known transmission signal at the output of an antenna, in order to simultaneously resolve the unknown received signal, typically much smaller in amplitude. The term in-band full duplex (IBFD) has been used to describe these systems specifically for applications in communications [22], whereas simultaneous transmit and receive (STAR) is a more general term that has been used principally for acoustic systems [23].

SIC systems for RF communications have been proposed using various design approaches. Figure 4(a) displays an early work by Choi *et al.* [22], who studied the concept of antenna cancellation as a method of increasing the isolation between transmitters (TX1 and TX2) and the receiver (RX), prior to processing the received signal with analog or digital hardware. It was found that placing the receiver at the “null zone” between TX1 and TX2 could increase isolation by up to 60 dB, however practical limits from distance and amplitude mismatch restricted antenna isolation to approximately 20 dB. Bharadia *et al.*

[71] followed with the system shown in Figure 4(b), which is a hybrid analog and digital system combined with an RF circulator. This approach achieved a significant level of 110 dB of SIC, which was necessary to reduce the amplitude of the self-interfering signal below the noise floor of the Wi-Fi system. The circulator also adds a unique benefit to this approach, as it is capable of interfacing with a single antenna to isolate signals for simultaneous transmission and reception, without suffering from sensitivity to distance or amplitude mismatch. Another approach by Ahmed *et al.* [81], shown in Figure 4(c), avoided the use of analog circuits and isolation components by performing SIC with an all-digital system. However, one drawback of this approach is that it requires an auxiliary receiver chain, which is an exact copy of the ordinary receiver chain used in the communication system, therefore all hardware including the mixer, analog-to-digital converter (ADC), and filters must be replicated in the system to achieve the desired performance.

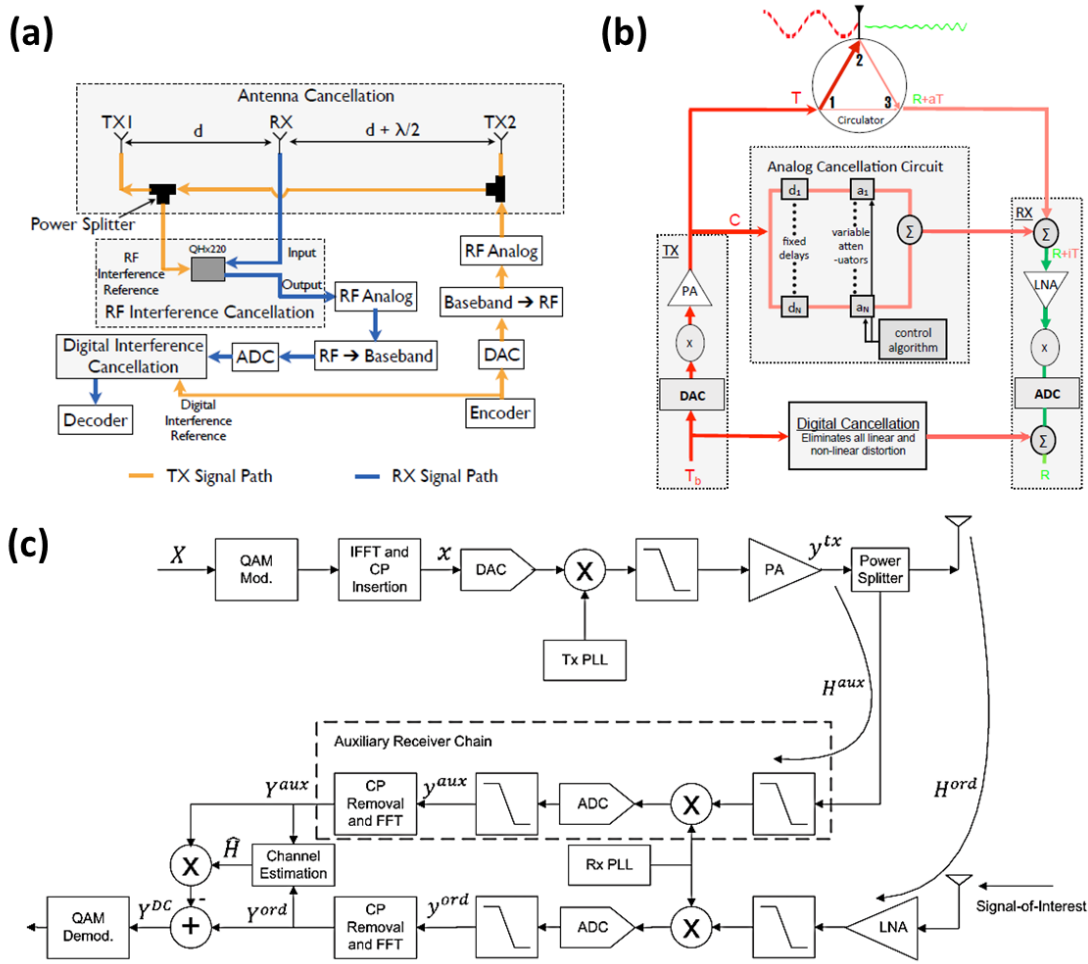


Figure 4. Overview of self-interference cancellation (SIC) systems in radio frequency (RF) communications. (a) SIC system that combines antenna isolation with digital interference cancellation to achieve in-band full duplex communication. Adapted from [22]. (b) A system that performs SIC with a combination of passive cancellation from a circulator, as well as a hybrid analog-digital cancellation system. Adapted from [71]. (c) An all-digital approach to SIC for RF applications, which leverages an auxiliary receiver chain to emulate the effects of the ordinary receiver chain on the received signal. Adapted from [81].

STAR systems have shown great promise as a relatively low-cost approach to doubling the data rate of traditional communication systems, which rely upon time-division

duplexing (transmitting and receiving at different times) or frequency-division duplexing (transmitting and receiving simultaneously over separate frequency bands) in order to avoid interference between signals. STAR systems have also been shown to help solve network problems including hidden terminals, loss of throughput due to congestion, and large end-to-end delays [22]. Furthermore, it has been shown that the maximum number of simultaneous users in a communication system can be increased as a result of STAR, with recent research showing that the number of users on a Global System for Mobile communication (GSM) system could be increased by a factor of 2.8 [76].

2.2.2 STAR in Acoustics and Vibration Control

While the majority of recent STAR research has been in the area of RF communications, a few authors have explored the applicability of STAR in acoustics, both in terms of acoustic communications [86]–[89] and acoustic measurement systems [23], [90], [91]. Figure 5(a) depicts a system diagram of a single acoustic transducer configured with a STAR system that performs SIC on the combined signal at the electrical interface of the transducer. Prior research on the topic of STAR in acoustic measurements is sometimes described as “self-sensing”, especially when the same transducer is used for both generation and reception of the acoustic signal. Of particular interest is the work by Leo and Limpert, which showed that self-sensing could be implemented in a loudspeaker and combined with feedback compensators in order to suppress the acoustic resonances of an enclosed cavity at low audio frequencies [92]. In the realm of acoustic noise control, systems were also developed to suppress acoustically driven vibration of plates, first by Ko

and Tongue [93], and later expanded upon by Qiu *et al.* [94]. Oshima *et al.* developed another adaptation of self-sensing for noise control (which typically employs a separate sensor and source to perform cancellation in free space) to simultaneously output and sense a tone at 100 Hz with a single loudspeaker [95]. Boulandet developed methods for coupling loudspeakers with a synthetic load in order to improve their performance as both speakers and sound absorbers [96]. In terms of ultrasonic transducers, Vossing *et al.* demonstrated that up to 70 dB of SIC can be observed at the output of an ultrasonic transducer by implementing a directional coupler that was manually adjusted to match the transducer response, as shown in Figure 5(b) [23]. Using a different approach, Schröder and Henning showed that 61 dB of SIC could be observed using sinusoidal burst waveforms by implementing an analog difference amplifier with gain and amplitude adjustments [90], shown in Figure 5(c), and then later demonstrated that such methods can be made independent of the radiation load by using a digital system identification approach [91].

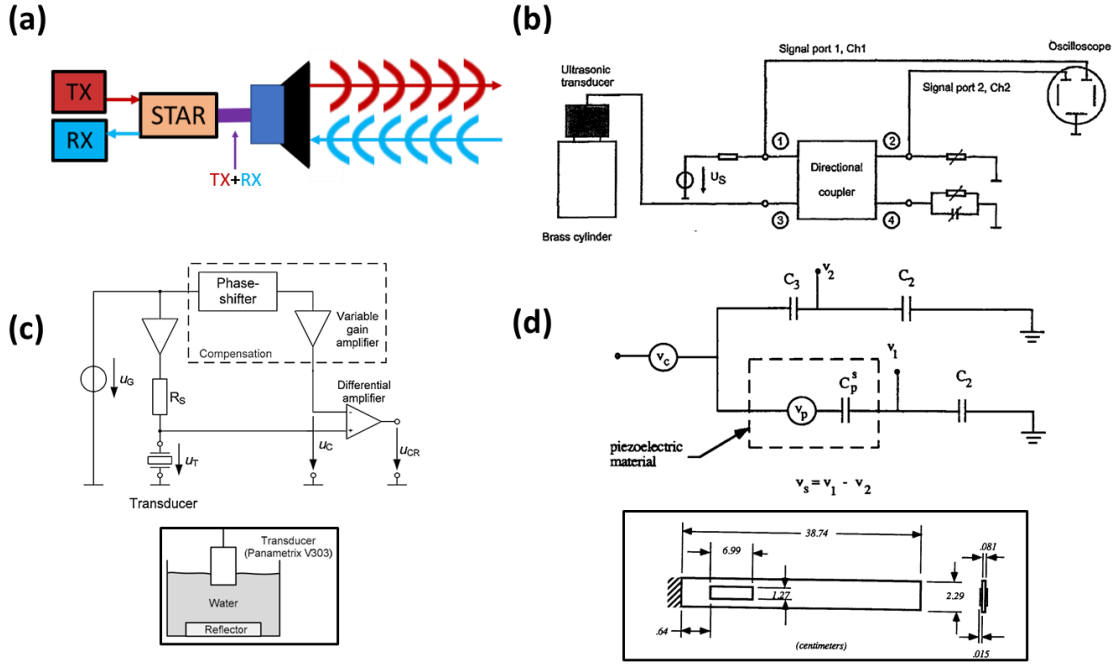


Figure 5. Overview of SIC systems in acoustic and vibration systems. (a) Overview of a single-transducer STAR acoustic system. The STAR system is used to isolate the transmitted and received signals while the transducer simultaneously sends and receives over the same frequency band. (b) A custom-built directional coupler was constructed to perform SIC on a 1 MHz ultrasonic transducer interfaced with a solid material sample. Adapted from [23]. (c) A difference amplifier was combined with a compensation circuit, consisting of a phase-shifter and variable gain amplifier, to cancel the self-interfering signal on a 1 MHz transducer that is configured to measure its own output from a rigid reflector in water. Adapted from [90]. (d) A passive bridge circuit is designed to perform SIC on a piezoelectric actuator at frequencies around 100 Hz. The measurement setup uses a vibrating cantilever beam with a single actuator that both senses the vibration and actively damps it simultaneously, using a closed loop control algorithm. Adapted from [24].

Prior to these works, similar concepts were developed within the field of vibration control, referred to as sensorless control systems or sensoriactuators, first proposed by Dosch and Inman [24], and soon followed by Anderson *et al.* [97]. Many of these efforts followed the approach proposed by Dosch and Inman, shown in Figure 5(d), to employ an

electrical bridge circuit to cancel the self-interfering signal, based on knowledge of the electromechanical impedance of the transducer [24], [97]–[104]. Following research employed all-digital [105]–[107] or hybrid analog-and-digital control schemes [102], [108]–[112] to further improve the accuracy of SIC. Alternative approaches included physical modeling of the device under test to enable SIC in post-processing [101], [113]–[125], while other works achieved self-sensing via frequency division, through filtering [126] or nonlinearity [127]. All of these works considered cancelling the self-interference from piezoelectric or electromagnetic actuators, typically operating below ~ 300 Hz, and generally implemented SIC in closed-loop control systems for the purpose of actively damping the vibrational modes of elastic structures.

STAR systems in the electromagnetic, acoustic, and vibrational domains share many common features, including methods of signal processing such as impulse response estimation, and similar stages of analog and digital cancellation. However, significant challenges remain in the execution of STAR for acoustical measurement systems. Acoustical systems typically operate at frequencies that are several orders of magnitude lower than those used for radio frequency (RF) communication, with generally much larger fractional bandwidths. They must also interface with electromechanical transducers, whose physics is very different from that of electromagnetic antennas, and then couple their mechanical motion to the fluid medium in which the acoustic wave propagates. Signals from acoustic transducers can be distorted due to the generation of harmonics associated with their nonlinear response that may be significant when considering the dynamic range desired for STAR systems. Finally, STAR systems in acoustics can experience multipath

reflections with time delays that are slower by a factor of 10^5 compared to those experienced by electromagnetic waves.

2.2.3 Motivation and Opportunities in STAR Acoustics

To further motivate the research presented in this work, a few particular advantages of developing STAR for acoustic measurement systems are described here. First, an acoustic system that can cancel all self-interference would enable continuous-time data monitoring, as opposed to the on/off nature of traditional time-division systems. This type of operation would result in doubling the time-bandwidth product, enabling the possibility of doubling the power spectral density or doubling the bandwidth for a given band-limited signal. As an example, consider the frequency-modulated (FM) sweep waveform presented in Figure 6(a) with a 50 percent duty cycle. This represents a signal in a traditional time-division measurement, in which approximately half of the time is reserved for transmission and the other half is reserved for reception. Figure 6(b)-(c) represent the signal when the measurement system is augmented with STAR. In this case, we leverage the doubling of the time-bandwidth product to either double the power in each frequency bin, as seen in the right-hand portion of Figure 6(b), or to double the measurement's bandwidth, as seen in Figure 6(c).

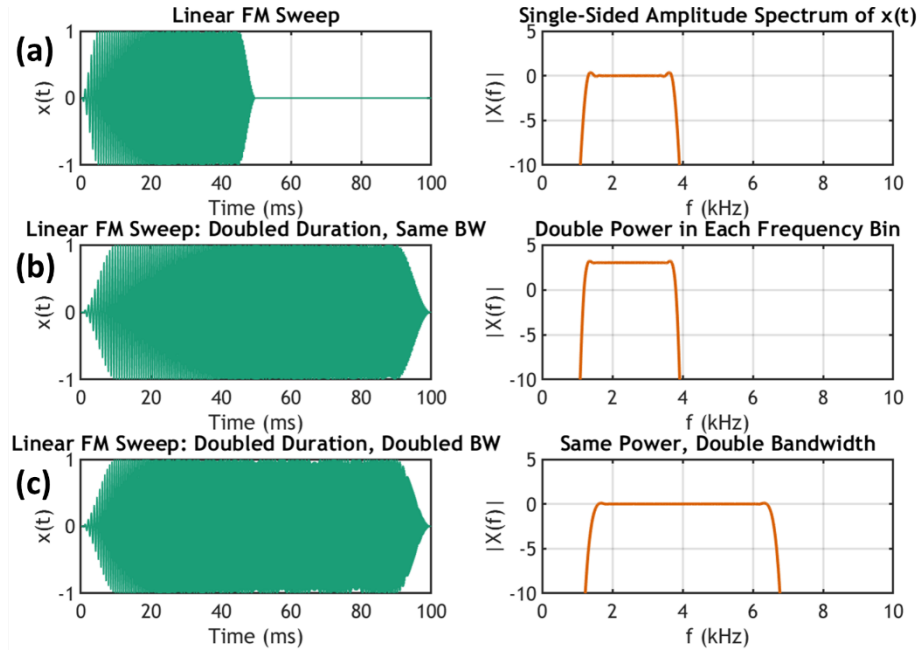


Figure 6. Conceptual demonstration of the benefits of doubling the time-bandwidth product for STAR measurements. (a) Timeseries of a linear FM sweep and its corresponding normalized frequency spectrum, representing the case of a traditional time-division measurement. (b) Timeseries of a linear FM sweep with the same frequency content as above but now with doubled duration, representing a continuous transmit-receive STAR measurement. This results in a spectrum with twice the amount of power in each frequency bin. (c) Timeseries of a linear FM sweep with double the bandwidth compared to (a), but with the same output power across the spectrum.

In addition, STAR in the time domain could also be used to improve near-surface imaging methods, such as those used for ultrasonic nondestructive evaluation (NDE). Figure 7(a) depicts a bulk acoustic wave propagating in an aluminum slab with a crack near the surface where an NDE transducer contacts the sample. Figure 7(b)-(d) show the propagation of an acoustic pulse with center frequency of 1 MHz and a fractional bandwidth of 50%, which is typical for NDE systems. With a sound speed of 6300 m/s, we

can see that the reflected pulse begins to overlap the incident waveform when the flaw has a distance of less than ~ 10 mm from the surface. The region where the echo return overlaps with the incident pulse is known as the near-surface “blind zone” of the transducer [128]. However, with an ideally performing acoustic STAR system, this flaw could be resolved regardless of the proximity to the face of the transducer, as indicated by the simplified simulation shown in Figure 7(e)-(f). This approach can be viewed as an alternative to post-processing techniques such as matched filtering or deconvolution, which can be used to extract highly correlated echo returns from an overlapping incident signal [129].

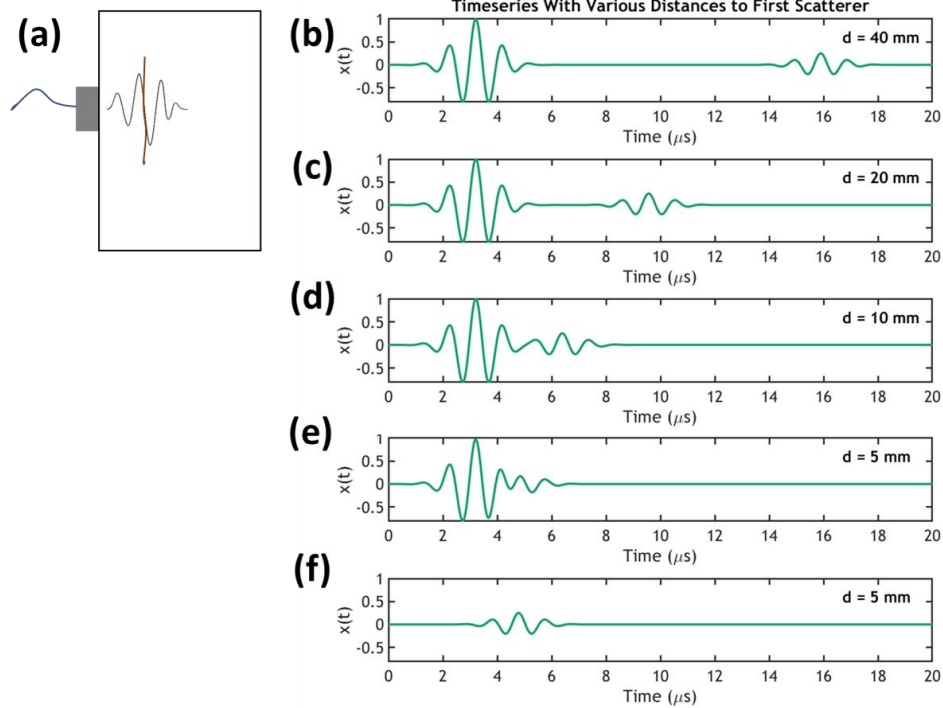


Figure 7. An example of enhanced near-surface acoustic imaging using acoustic STAR. This approach can be viewed as an alternative to the signal processing techniques such as matched filtering, or as a method that may augment the capability of a given matched filter due to the finite pulse compression ratio.

One advantage of the STAR approach is that it could function in real time for continuous monitoring. Another advantage is that STAR may have a reduced dependency on the accuracy of propagation models, in comparison with matched filtering. Matched filtering generally assumes that an accurate propagation model is known *a priori*; otherwise, the filtering method is referred to as blind deconvolution. Blind deconvolution is inherently more susceptible to error and uncertainty, given that the characteristics of any sources of parasitic convolution during propagation are not well known [130]. One example of this is a medium with strong dispersion or nonlinearity, which can be difficult to model. In comparison, the STAR approach generally assumes that the complex input impedance of the measurement is known, which enables the isolation of transmitting and received signals. Furthermore, the use of STAR to augment near-surface imaging systems could be combined with existing matched filtering methods to break traditional limits of the pulse compression ratio (proportional to $1/\Delta f$), which is a fundamental limitation of matched filtering when used on its own [131].

Finally, in considering arrays of acoustic transducers, STAR could be used to double the time-bandwidth product of each element within an array. However, simultaneously transmitting and receiving with arrays presents additional challenges of filtering the radiated self-interference from neighboring elements [77] [132]. It is also worth noting that due to the physical similarity of many acoustic measurement systems, there are numerous opportunities in acoustic STAR that have been either unexplored or only more recently studied; some of these are summarized in Table 2.

Table 2. Explains several possibilities for leveraging STAR in acoustic measurement systems and describes some of the technical differences between each area.

Measurement Type	Approximate Frequency Range	Materials	Description of STAR Application
<u>Non-Destructive Evaluation</u>	100 kHz–15MHz	Any solids: e.g., metals, plastics, or composites.	<ul style="list-style-type: none"> • Measure longer reflection durations than standard time division methods permit. • Measure reflections that are closer to the surface of the transceiver than is traditionally possible.
<u>Biomedical Ultrasound</u>	2 MHz–15 MHz	Tissue and blood	Enhance the signal-to-noise ratio, bandwidth, or axial resolution of individual transducer measurements.
<u>Doppler Ultrasound</u>	4 kHz–200 MHz	Tissue and blood (Medical), Air (Meteorology), Water (Geology and NDE)	Improve co-location of the doppler transmitter and receiver to improve doppler shift measurements (see Section 6.2).
<u>Ballistocardiography</u>	DC–40 Hz	Tissue and blood	Apply STAR to the accelerometer or strain gauge to increase signal-to-noise ratio, bandwidth, or axial resolution.
<u>Phonocardiography</u>	1 Hz–2 kHz	Tissue and blood	Enhance signal-to-noise ratio or axial resolution of the microphone measurement.
<u>Simultaneous Microphone Transceivers</u>	20 Hz–20 kHz	Air	<ul style="list-style-type: none"> • Create new functionality to use any existing microphones as speakers simultaneously, or vice-versa. • Opportunities to design new microphones which are optimized for both transmission and reception.

Table 2 (continued)

<p><u>Underwater Communications</u></p>	<p>20 kHz–30 kHz</p>	<p>Water</p>	<p>In-band Full Duplex (IBFD) underwater communication.</p> <ul style="list-style-type: none"> • Double the data rate of communication, compared to traditional time division or frequency division protocols. • Increase the number of simultaneous users on a given communication system.
------------------------------------------------	----------------------	--------------	---------------------------------------------------------------------------------------------------------------------------------------------------------------------------------------------------------------------------------------------------------------------------------------------------------------------

2.3 SUMMARY

In Section 2.1, the technical background of acoustic supercoupling was described. Physical principles were presented to explain the mechanisms that result in near-zero effective material properties in both electromagnetics and acoustics. Major technical contributions were summarized, from the initial developments in electromagnetic zero-index materials, to electromagnetic supercoupling, and finally acoustic zero-index materials and acoustic supercoupling. Existing challenges in the fabrication of acoustic supercoupling devices were highlighted, such as the lack of experimental evidence of supercoupling via manipulation of ρ_{eff} (using periodic series membrane inclusions) or C_{eff} , (using periodic shunted mass elements). The research presented in Chapter 3 of this work addresses these issues through an alternative approach to acoustic supercoupling, which takes advantage of the effective compressibility of an acoustic waveguide at a higher-order cutoff frequency to realize acoustic supercoupling, both theoretically and experimentally, with a simple coupled waveguide geometry.

In Section 2.2, an overview of the technical background was presented for self-interference cancellation in acoustical systems and principles of operation were described. While prior works in STAR acoustics have focused on closed-loop control of low frequency signals or the analog cancellation of ultrasonic signals with difference amplifiers, the research presented in Chapter IV-V considers the implementation of SIC using a generalized passive bridge circuit model and provides insights regarding the advantages and disadvantages of the passive approach. It will be shown that more than 55

dB of SIC can be achieved with all passive components at ultrasonic frequencies (~500 kHz) without the need for manual adjustment or digital feedback. Furthermore, while other works have emphasized frequency domain analysis, it is our interest to examine STAR for pulse-echo measurement systems, where time-domain processing plays a critical role in extracting relevant features from the signal of interest. Finally, this work focuses on single-element STAR, although implementation with multiple elements, such as transducer arrays for SONAR systems or biomedical imaging systems, is possible and would follow a generalization of the approach presented in this work [75],[78],[86],[89].

Chapter III: Acoustic Supercoupling with Compressibility-Near-Zero Material Properties

3.1 INTRODUCTION

In this chapter, we will show that it is possible to realize acoustic supercoupling in a hollow waveguide by exciting a higher-order mode at cut-off, providing an experimentally-viable, simple geometry that demonstrates effective zero compressibility and supercoupling for sound². Despite the use of simple materials with physically hard boundaries, the excitation of a higher-order mode is shown to synthesize effective soft-boundary waveguide channels that support a cut-off at finite frequency, and therefore enable this unusual tunneling phenomenon. The main results for compressibility-near-zero (CNZ) supercoupling are presented first in Section 3.2. Next, Section 3.3 provides a discussion and interpretation of the modeling and experimental results. In Section 3.4, the modeling and experimental methodology are explained in further detail.

Following the presentation of the fundamental concepts of CNZ supercoupling in Sections 3.1-3.4, an acoustic power divider relying on CNZ media is investigated in Section 3.5. Analytical and numerical models are developed to prove and support the concepts. An N -port series power divider is then shown to support operation with several ports arbitrarily positioned, ensuring equal amplitude and phase power division. The divider may be also configured to divide the signal with a phase flip of π radians, alongside with equi-phase output ports. An analysis of practical trade-offs due to losses is presented within a broader discussion on the scalability of the proposed device. Finally, the chapter closes with concluding remarks in Section 3.6.

² Portions of this chapter have been previously published in [144] and [145]. See the “Statement of Shared Contributions” in the front matter of this document for a description of each author’s contributions.

3.2 RESULTS OF THE CNZ SUPERCOUPLING STUDY

In order to demonstrate the effect of supercoupling for sound in a simple waveguide geometry, we consider the configuration of Figure 8 in which we sandwich an intermediate channel with large cross-sectional area S_2 , length L and modal impedance Z_2 between two narrow input/output channels, each with acoustic impedance Z_1 and much narrower cross-sectional area S_1 .

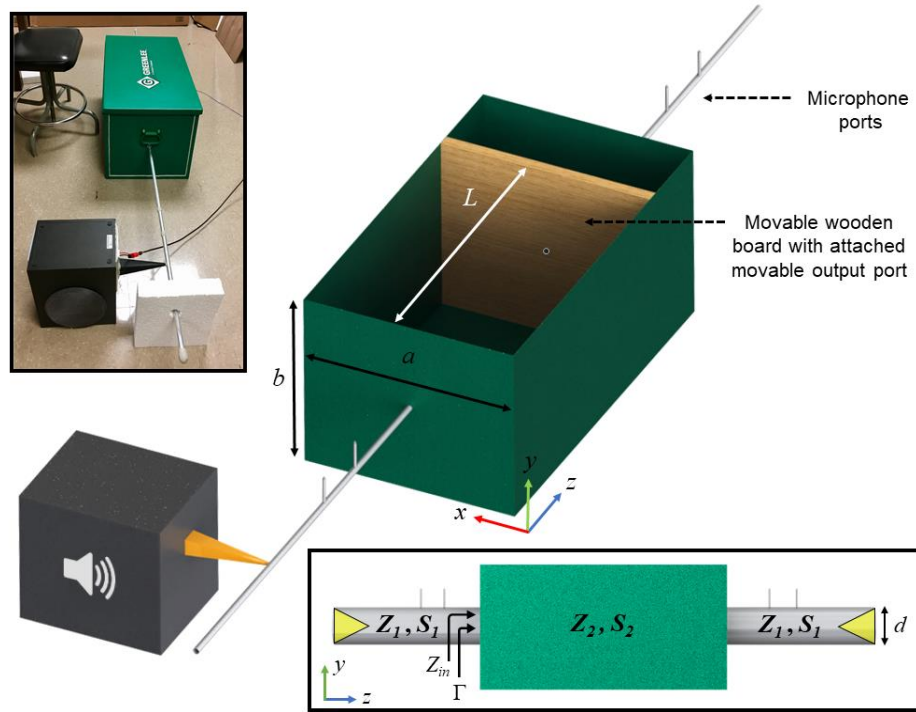


Figure 8. Geometry of the CNZ supercoupling experiment. The geometry under analysis consists of input and output waveguides connected by a much wider intermediate channel with variable length. The output port remains flush with the face of the wooden boundary and moves along with the boundary as L is varied. (*Inset bottom*): transmission line model. (*Inset top-left*): photograph of the experimental setup.

As derived in Section 3.4 *Materials and Methods*, the reflection coefficient at the input port reads

$$\Gamma = \frac{(Z_2^2 - Z_1^2) \tan(k_z L)}{(Z_1^2 + Z_2^2) \tan(k_z L) + 2jZ_1 Z_2}, \quad (3.1)$$

where k_z is the wave number in the middle-channel. Reflection is minimized when $\tan(k_z L) = 0$ or when $Z_2 = \pm Z_1$. The first condition corresponds to conventional Fabry-Perot resonances, which depend upon the length and geometry of the connecting channel. However, tunneling independent of the channel length, as expected in supercoupling phenomena, can be achieved at the impedance matching condition $Z_2 = Z_1$.

A straightforward way to realize this matching condition in waveguides with large geometrical mismatch, as in Figure 8, is to consider a rectangular channel bounded by two hard boundaries and two soft boundaries. This waveguide does not support a mode at low frequencies, and the dominant (or leading-order) propagating mode, as derived in Section 3.4, has impedance

$$Z_2 = \frac{\omega \rho_0}{S_2 \sqrt{\left(\frac{\omega}{c_0}\right)^2 - \left(\frac{\pi}{a}\right)^2}}, \quad (3.2)$$

where ω is the driving frequency, ρ_0 is the density of the filling medium, c_0 is the corresponding sound velocity, and a is the distance between the two soft boundaries. In particular, the impedance becomes very large at the cut-off frequency of the dominant mode $f = \frac{c_0}{2a}$, when the term in the square root goes to zero. For values close to cut-off,

impedance matching can be achieved, as the small value of the square root is compensated

by $S_2 \gg S_1$, yielding zero reflection and full transmission independent of the channel length. In order to confirm this intuition, Figure 9(a) shows full-wave simulations evaluating the transmission through this geometry varying the channel length L . For each length, the first peak in transmission corresponds to the supercoupling frequency, which arises near the cut-off frequency of the intermediate channel. The higher-frequency transmission peaks are due to Fabry-Perot resonances, which are largely dependent on the channel length. By increasing the length of the channel, the number of Fabry-Perot resonances increase for a fixed frequency spectrum, however the tunneling frequency remains nearly unchanged. Figure 9(b) presents the corresponding phase of the pressure field along the channel at the supercoupling frequencies, and the inset shows the 2D field distribution for the different lengths considered. We observe completely uniform phase along the channel, independent of the length of the coupling channel, consistent with propagation in a zero-index material, and with the previous observations of supercoupling in ENZ media for electromagnetic waves [12]–[15], [32], [34].

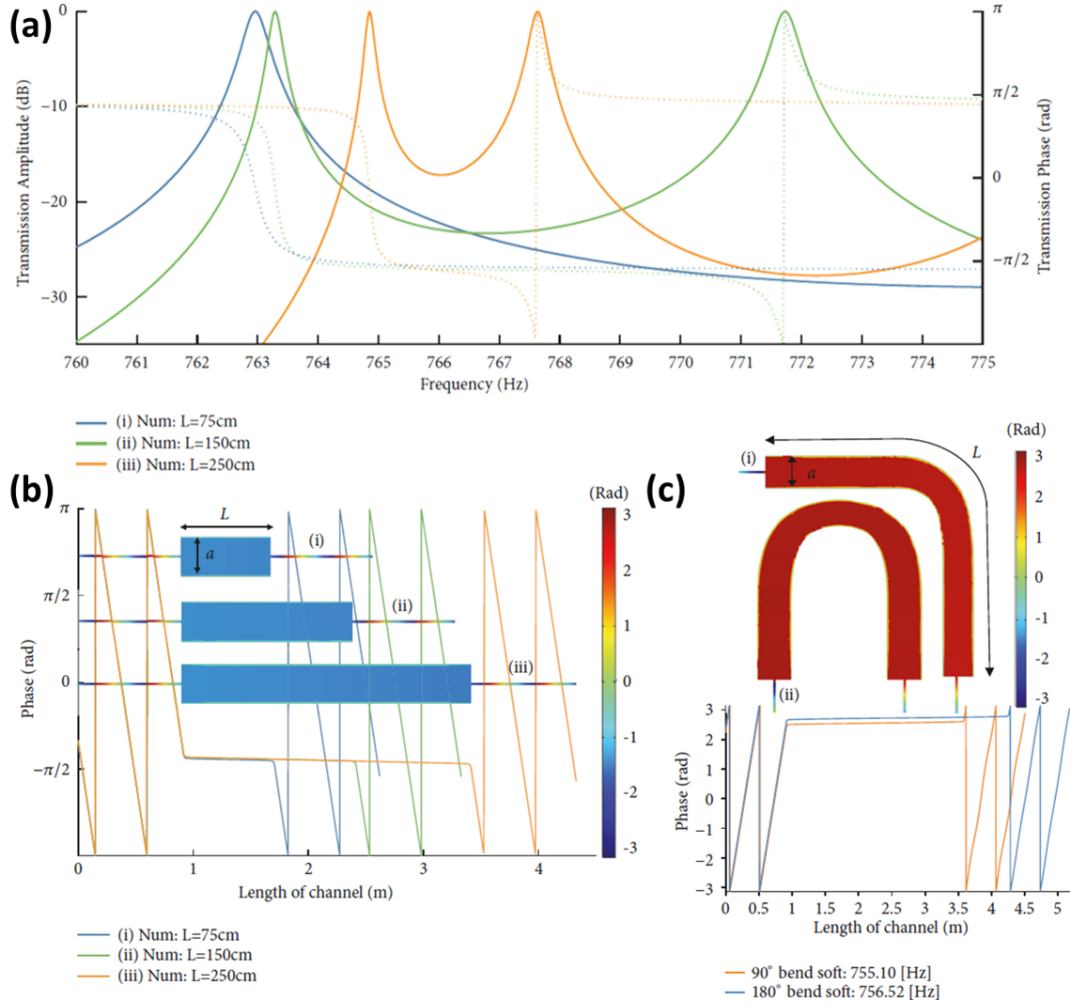


Figure 9. Waveguides with two soft and two hard boundaries, operated near the cut-off frequency. **(a)** Calculated transmission phase and amplitude. The design parameters are similar to the experimental setup, with only the length being modified ($a = 0.225$ m, $b = 0.382$ m, and $d = 12.6$ mm). **(b)** Phase distribution through the CNZ channel near the first cut off frequency for different lengths. $f_{\text{tunneling}}$ (i) = 763.0 Hz, $f_{\text{tunneling}}$ (ii) = 763.3 Hz, $f_{\text{tunneling}}$ (iii) = 764.9 Hz. **(c)** Spatial variation of phase at the CNZ tunneling frequency for waveguides with 90° and 180° bends. We observe uniform phase despite bending of the channel. Here, $f_{\text{tunneling_90}}$ (i) = 755.10 Hz, $f_{\text{tunneling_180}}$ (ii) = 756.52 Hz.

Indeed, for the intermediate channel the effective constitutive parameters can be retrieved as discussed in Section 3.4, yielding

$$\begin{cases} \rho_{\text{eff2}} = \rho_0 \\ \kappa_{\text{eff2}} = \frac{\kappa_0}{1 - \left(\frac{\pi c_0}{a\omega}\right)^2}, \end{cases} \quad (3.3)$$

where κ_0 is the bulk modulus of the filling material. These equations confirm that at the cut-off frequency $f = \frac{c_0}{2a}$, κ_{eff} has a pole, the effective compressibility goes to zero, and

the phase velocity $\frac{\omega}{k_z} = \sqrt{\frac{\kappa_{\text{eff}}}{\rho_{\text{eff}}}}$ becomes infinite. We conclude that the geometry in Figure

8 with mixed hard and soft boundary walls, realizes the dual of zero-density supercoupling, enabling the compensation of large geometrical mismatch in the middle channel through compressibility close to zero. The electromagnetic analogue has been explored in [37],[54] as a wide channel filled by MNZ materials. Consistent with these works and similar phenomena for zero-density supercoupling [45], Figure 9(c) shows that supercoupling tunneling and infinite phase velocity is preserved also when the connecting channel is bent in different configurations, an effect of the quasi-static nature of wave propagation associated with its infinite phase velocity.

So far, we have shown that it is possible to achieve the equivalent of zero-compressibility propagation and supercoupling in a waveguide with mixed hard and soft boundary walls, operating near its cut-off frequency. However, this configuration is hardly realizable in a realistic geometry. Interestingly, in the following we show that it is possible

to achieve an analogous functionality exciting a waveguide with all hard boundaries, as in the case of a conventional acoustic waveguide filled by air, at the cut-off frequency of one of its higher-order modes. In the Section 3.4 we indeed show that the effective constitutive parameters of the $(m,n) = (2,0)$ mode supported by a hard-wall waveguide indeed satisfies a similar expression as in (3.3), ensuring a zero-compressibility condition near its cut-off.

The difference compared to the soft-hard waveguide in Figure 9 is the presence of other modes in the waveguide, including the dominant mode $(m,n) = (0,0)$, which has no cut-off. However, we notice that these other modes, not being operated near the cut-off frequency, are badly mismatched to the input and output waveguides, due to the large geometrical mismatch. Therefore, their coupling to the input signal is negligible. In other words, the transition between different waveguides can be treated as a multi-port network, and the impinging energy naturally couples to the higher-order mode at cut-off, given that the impedance is conserved. In our geometry, we drive the middle channel at its center, totally preventing the excitation of odd-order modes because of symmetry. The dominant $(0,0)$ mode is not excited due to the large impedance mismatch, and therefore all the energy can flow unperturbed into the second-order mode at the Compressibility-Near-Zero (CNZ) frequency.

Figure 10 verifies this prediction in full-wave simulations of a hard-walled acoustic waveguide. Quite surprisingly, we retrieve very similar functionality in this configuration, relying on a simple hollow waveguide driven at the cut-off frequency of its $(2,0)$ mode, $f = c_0 / a$. We can see that the spatial phase distribution of Figure 10(b) matches well the one of Figure 9(b) in the center of the channel, with infinite phase velocity throughout the

channel independent of its length. In the transverse plane of the waveguide we observe a phase flip by π , associated with the modal distribution of the excited higher-order mode. Interestingly, the location of the flip is exactly the effective location of a soft-wall boundary, consistent with the results in Figure 9. This concept may be useful to design effective soft-wall waveguide structures using materials that are not substantially softer than the filling medium. We also note that in this scenario, due to the quasi-static nature of the pressure field near the CNZ frequency, the acoustic wave tunneling occurs regardless of the shape of the channel, as demonstrated in Figure 10(c). In this case, the effective soft boundary also follows the bending profile adiabatically.

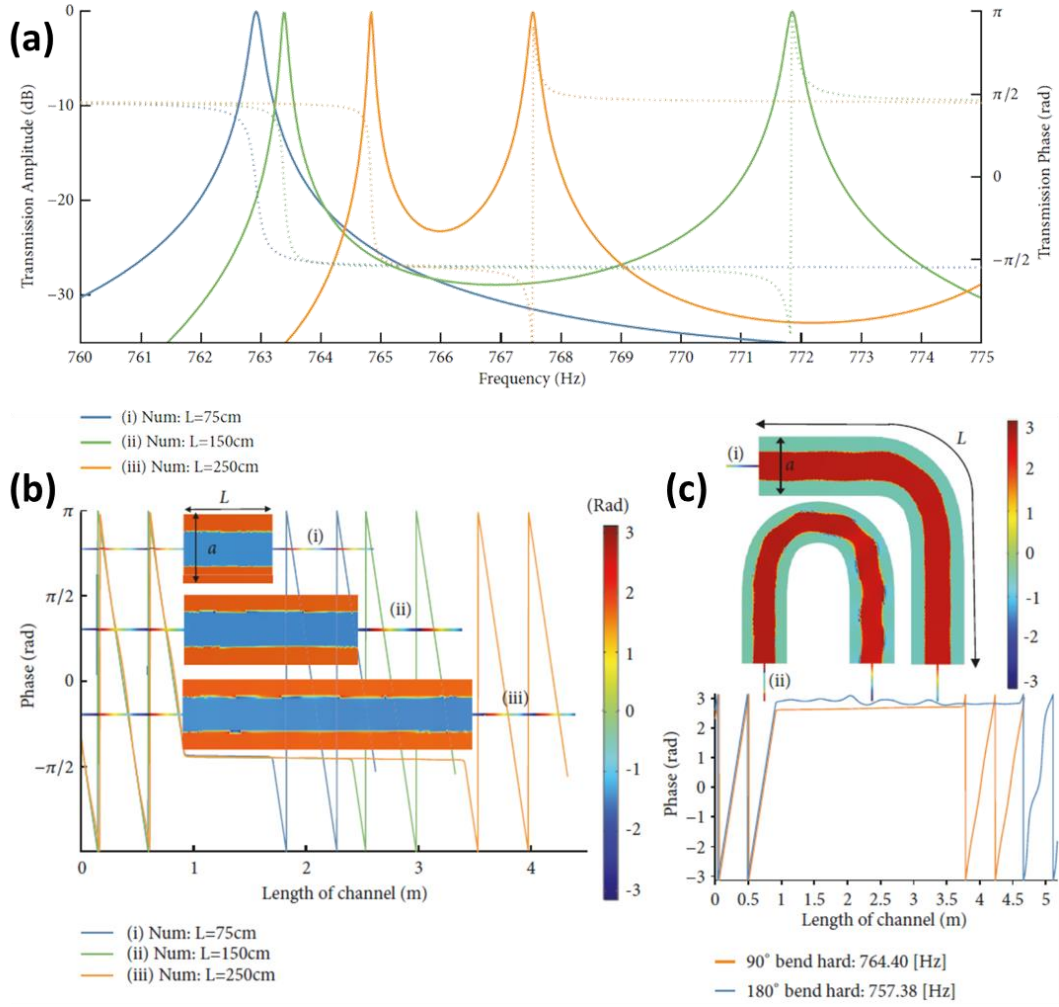


Figure 10. Waveguides with hard boundary walls, operated near the higher-order $(2,0)$ mode cut-off of the intermediate channel. We can see that the higher-order mode matches the phase pattern of a soft-hard $(1,0)$ mode (from Figure 9) in the center of the channel. This presents an “*effective soft boundary*” along the planes where the phase flips by π . This flip results from a change in sign of the pressure, which is a purely real-valued standing wave. **(a)** Numerical results for transmission phase and amplitude. The design parameters are similar to the experimental setup, with only the length being modified ($a = 0.450\text{ m}$, $b = 0.382\text{ m}$, and $d = 12.6\text{ mm}$). **(b)** Phase distribution through the CNZ channel near the $(2,0)$ cut-off frequency for hard-hard configurations of different lengths. For bottom figure: $f_{\text{tunneling}}(\text{i}) = 762.9\text{ Hz}$, $f_{\text{tunneling}}(\text{ii}) = 763.4\text{ Hz}$, $f_{\text{tunneling}}(\text{iii}) = 764.8\text{ Hz}$. **(c)** Spatial variation of phase at the CNZ tunneling frequency under 90° and 180° bends. Here, $a = 0.450\text{ m}$, $b = 0.382\text{ m}$, $f_{\text{tunneling}_90}(\text{i}) = 764.40\text{ Hz}$, $f_{\text{tunneling}_{180}}(\text{ii}) = 757.38\text{ Hz}$.

Figure 11 presents our experimental verification of CNZ supercoupling in a channel with variable length operated near the cut-off frequency of its (2,0) mode. We built the intermediate channel using an off-the-shelf steel welder's tool box, in which a wooden wall was shifted in different positions to change the length of the channel. The measured data capture the physics of the problem well: impedance matching and near-zero phase delay in transmission, independent of the length of the intermediate channel, are verified experimentally, despite the fact that the walls of our waveguide are not ideally hard (details of the experimental setup are provided in Section 3.4). To aid in comparing numerical results to experiment, the model in Figure 11 treated the boundaries of the coupling channel as elastic shells, which are capable of radiating sound into the surrounding air. This model also allowed for coupling of acoustic energy into vibrational modes of the walls, and for dissipation due to loss within the material (with $\tan \delta = 0.05$ for steel lined with silicone caulk). This more realistic condition resulted in predicted transmission amplitudes with 13-18 dB of loss (depending upon length), whereas the experimental results showed similar loss levels of 17-18 dB. This agreement in transmission is good, considering the uncertainties in material properties and variation of the intermediate channel geometry from an ideal rectangular prism. The data displayed slightly lower-Q resonances than in the ideal scenario with hard walls, as expected, but confirmed nearly infinite phase velocity, and a tunneling frequency nearly independent of the channel length.

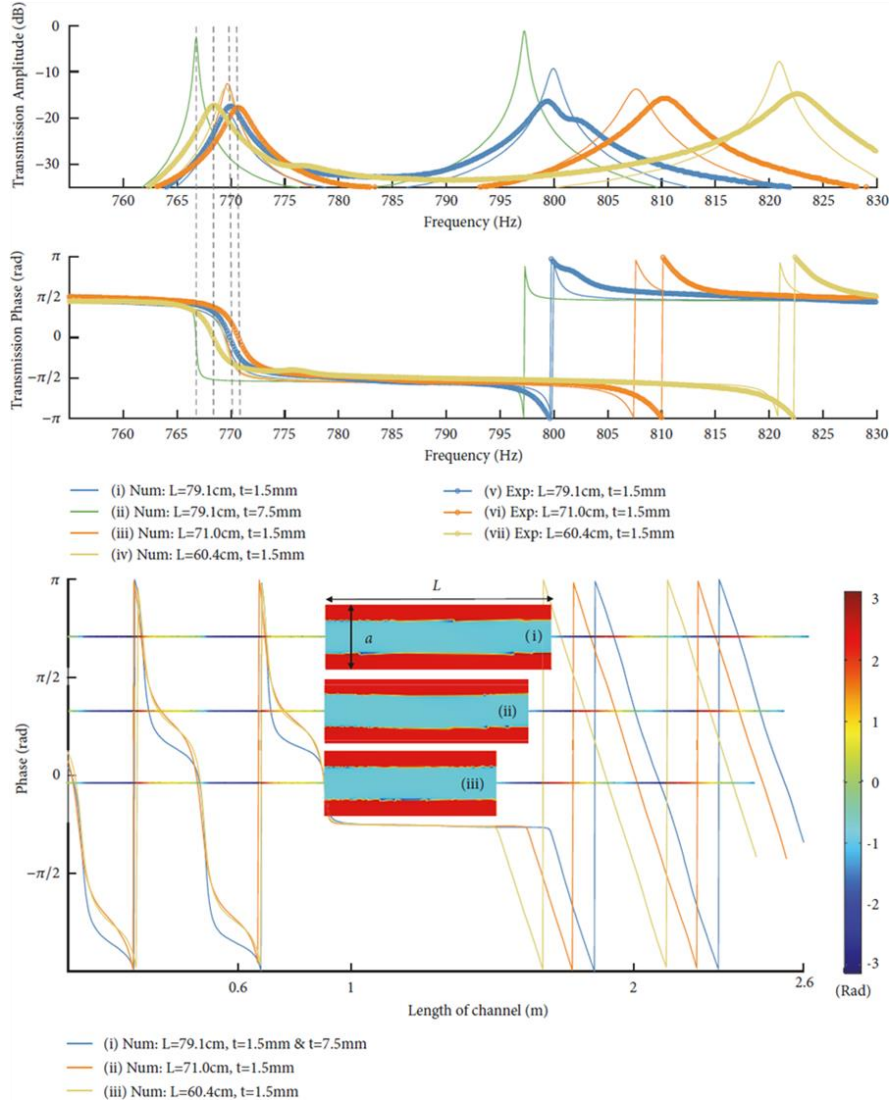


Figure 11. Experimental measurements and numerical results for supercoupling channel. **(a)** Numerical and experimental comparison for the transmission phase and amplitude. Radiation and material loss from the intermediate channel were modeled using elastic shell boundary conditions with a loss tangent of 0.05. Note that curve (ii), in green, shows the transmission amplitude at the tunneling frequency (~ 765 Hz) is much higher than the others, due to the use of thicker walls for the intermediate channel. The experimental parameters were $a = 0.450$ m, $b = 0.382$ m, and $d = 12.6$ mm. **(b)** Spatial phase distribution through the CNZ channel at the tunneling frequency for configurations with different lengths and $f_{\text{tunneling}}$ (i) = 769.6 Hz, $f_{\text{tunneling}}$ (ii) = 769.6 Hz, $f_{\text{tunneling}}$ (iii) = 769.4 Hz.

3.3 DISCUSSION OF CNZ SUPERCOUPLING RESULTS

In Section 3.2, we presented theoretical and experimental validation of a straightforward way of realizing zero compressibility acoustic wave propagation in waveguides, by exciting a higher-order mode at the cut-off frequency. We used this unusual propagation regime to realize the supercoupling phenomenon for sound, enabling tunneling of energy through largely mismatched waveguide geometries. Our theoretical results accurately capture the physics behind this anomalous tunneling, and our experiments confirm large phase velocity and anomalous transmission independent of the channel length. The small discrepancies between measurements and numerical predictions can be explained by irregular geometry and uncertainties in the detailed material properties of the off-the-shelf toolbox used for the middle channel in the experiment. We estimate that the supercoupling transmission loss may be practically reduced below 2 dB, if the middle channel were manufactured with a steel wall thickness of approximately 7.5 mm or higher (see Figure 11(a)).

In summary, we can describe the supercoupling phenomenon as a dispersive impedance matching condition, which occurs when the coupling channel (with smaller characteristic impedance than the input waveguide) has an input impedance that appears nearly infinitely stiff. At this matching condition, the phase velocity approaches infinity, as long as S_2/S_1 is sufficiently large. Under this condition, we achieve full amplitude transmission and total conservation of the phase, independent of the height and length of the coupling channel. Moreover, our results show that a hard-wall waveguide, when driven near the cut-off frequency of a higher-order mode, exhibits compressibility-near-zero

effective material properties, and may be thought of as consisting of two effective soft boundaries, along which the pressure field is equal to zero and the uniform phase of the tunneling mode flips by π . Quite surprisingly, it is possible to suppress the excitation of all other modes in the waveguide, including the dominant plane-wave mode, thanks to the largely mismatched cross-section at the connecting interfaces.

3.4 MATERIALS AND METHODS

3.4.1 Transmission-line model for acoustic supercoupling

Suppose two identical waveguides, each with cross sectional area S_1 , filled with a fluid with characteristic acoustic impedance Z_1 . These waveguides are connected as an input and output to an intermediate rectangular acoustic channel, as in Figure 8, with length L , fluid with characteristic impedance Z_2 and cross-sectional area S_2 . Using transmission-line theory, the reflection coefficient for a plane wave from one port of this structure is written as

$$\Gamma = \frac{Z_1 - Z_{\text{in}}}{Z_1 + Z_{\text{in}}} \quad (3.4)$$

where Z_{in} is the impedance seen from the input waveguide when looking into the channel and it is calculated using

$$Z_{\text{in}} = Z_2 \frac{Z_1 + jZ_2 \tan(k_z L)}{Z_2 + jZ_1 \tan(k_z L)}. \quad (3.5)$$

Plugging Eq. (3.5) in (3.4), the reflection coefficient reads as in Eq. (3.1).

3.4.2 Cut-off in acoustic waveguides and compressibility-near-zero

For sound propagating in an acoustic waveguide with hard boundaries filled by a medium with density ρ_{eff} and bulk modulus κ_{eff} , the following relations can be written

$$\left\{ \begin{array}{l} \frac{\sqrt{\rho_{\text{eff}} \kappa_{\text{eff}}}}{S} = Z \\ \sqrt{\frac{\rho_{\text{eff}}}{\kappa_{\text{eff}}}} = \frac{k_z}{\omega} \end{array} \right., \quad (3.6)$$

where Z and k_z are defined as the acoustic impedance and wave vector in the z -direction, and S is the cross-sectional area of the waveguide. Solving Eq. (3.6) for the effective constitutive parameters results in

$$\left\{ \begin{array}{l} \rho_{\text{eff}} = \frac{Z S k_z}{\omega} \\ \kappa_{\text{eff}} = \frac{Z S \omega}{k_z} \end{array} \right., \quad (3.7)$$

which allows retrieval of the effective constitutive parameters knowing impedance, wave number, operating frequency, and cross-sectional area of the waveguide.

Consider now a waveguide with two parallel soft boundaries at $x = \{0, a\}$ and two parallel hard boundaries at $y = \{0, b\}$. For this configuration, the spatial pressure distribution is given by $p_{mn} = A_{mn} \sin(\frac{m\pi}{a}x) \cos(\frac{n\pi}{b}y)$, and it exhibits cut-off at discrete frequencies

$$f_{mn}^c = \frac{c}{2\pi} \sqrt{\left(\frac{m\pi}{a}\right)^2 + \left(\frac{n\pi}{b}\right)^2}. \quad (3.8)$$

Due to the sinusoidal term in the pressure expression, the mode $(m,n) = (0,0)$ is not supported, resulting in a non-zero cut-off frequency for the dominant mode $(m,n) = (1,0)$,

which we denote as the first cut-off frequency, only depending upon the width a of the channel.

Momentum conservation requires

$$\nabla p + j\omega\rho_0 u = 0, \quad (3.9)$$

therefore the particle velocity u is given by

$$u = \frac{-A_{mn}e^{-jk_z z}}{j\omega\rho_0} [k_x \cos(k_x x) \cos(k_y y) \hat{x} - k_y \sin(k_x x) \sin(k_y y) \hat{y} - jk_z \sin(k_x x) \cos(k_y y) \hat{z}] \quad (3.10)$$

and $Z = p / S u$ for the ($m=1, n=0$) mode, which gives the result in Eq. (3.2).

Then, combining Eq. (3.7) with Eq. (3.2), we derive the effective material properties of the acoustic waveguide with soft-hard boundaries near the (1,0) mode cutoff, yielding Eq. (3.3)

. It is observed that the value of the effective bulk modulus has a pole for $f = \frac{c_0}{2a}$, and

consequently the effective compressibility tends to zero.

This CNZ condition can be exploited to induce supercoupling through a soft-hard channel waveguide. These boundaries however can be difficult to realize in practical acoustic media. For a more realistic case, we assume a waveguide configuration in which all boundaries are composed of a hard material. This is a typical scenario for air-filled waveguides. In this case, the spatial pressure distribution is

$$p_{mn} = A_{mn} \cos\left(\frac{m\pi}{a} x\right) \cos\left(\frac{n\pi}{b} y\right), \quad (3.11)$$

and the cut-off frequencies are again given by Eq. (3.8). In this case, the first cut-off frequency is zero, and a plane wave mode can propagate also for very low frequencies in this configuration. However, a compressibility near zero (CNZ) condition can arise when

the hard boundary waveguide is operated near a higher cut-off frequency, for instance with

$$(m,n) = (2,0) , \text{ for which } \kappa_{\text{eff}2} = \frac{\kappa_{0_2}}{1 - (\frac{c_0}{af})^2}, \text{ and the CNZ frequency is } f = \frac{c_0}{a}.$$

3.4.3 Numerical modeling

Finite element analysis was conducted using Comsol Multiphysics. The Pressure Acoustics module was selected with the frequency domain solver. Air was chosen from the Comsol built-in material list as the filling fluid of all structures. Finally, the input and output ports were set to Plane Wave Radiation conditions, while the acoustic source was modeled as an Incident Pressure Field at the input port. In Figure 8, the walls of the intermediate channel were modeled as either hard or soft boundary conditions. For the simulation of experimental parameters and consideration of vibrational coupling in the results of Figure 11(a), the supercoupling system was first placed in an external rectangular domain filled with air. This domain enabled the modeling of leakage from the intermediate channel and was bounded by Perfectly Matched Layers (PMLs) to realize non-reflecting boundaries. Materials were chosen from the built-in material library as Steel AISI 4340 for the intermediate channel walls and aluminum for the input/output channel. The effects of visco-thermal acoustic boundary-layer loss were modeled by specifying the input/output waveguides as coupled to Narrow Region Acoustics. Then, walls in the intermediate channel were numerically modeled as thin elastic shells in the Comsol Acoustic-Shell Interaction Module. Finally, the reflection and transmission coefficients were calculated

using a four-microphone measurement technique similar to [133], where the value of complex k_z was derived from numerical simulations using complex sound speed.

3.4.4 Measurements

The experimental setup was built from an off-the-shelf steel welder's tool box with dimensions of $a = 0.450$ m, $b = 0.382$ m, $L = 0.79$ m, and wall thickness of 1.54 mm. The input and output waveguides were nearly-identical aluminum tubes with inside diameter of 12.6 mm, length of 92 cm, and wall thickness of 1.6 mm. The input waveguide was fed by a horn that was mounted transversely to the direction of propagation, and both input and output waveguides were terminated with anechoic foam to suppress standing waves in the tubes. Measurements were carried out with a procedure similar to [133] and following the standards of [134] and [135]. Due to the small dimensions of the input and output waveguides, a modest amount of acoustic boundary-layer loss was observed in the waveguides alone. This was corrected for by employing a complex value of $k_z = \beta + j\alpha$ in the transfer-matrix equations, with $\alpha \approx -0.13 \text{ m}^{-1}$ according to [2].

3.5 SUPERCOUPLING POWER DIVIDER WITH CNZ PROPERTIES

3.5.1 Theory

In a zero-index material, the governing wave equations are temporally and spatially decoupled [38]. For acoustic phenomena, this property results in a pressure field that is uniform throughout the medium; therefore, if the signal is sampled from such a medium at different points, the output signals are expected to have equal phase. To demonstrate this

phenomenon, let us consider the scenario where several input and/or output channels are connected to an intermediate medium with near-zero-index properties, as shown in Figure 12.

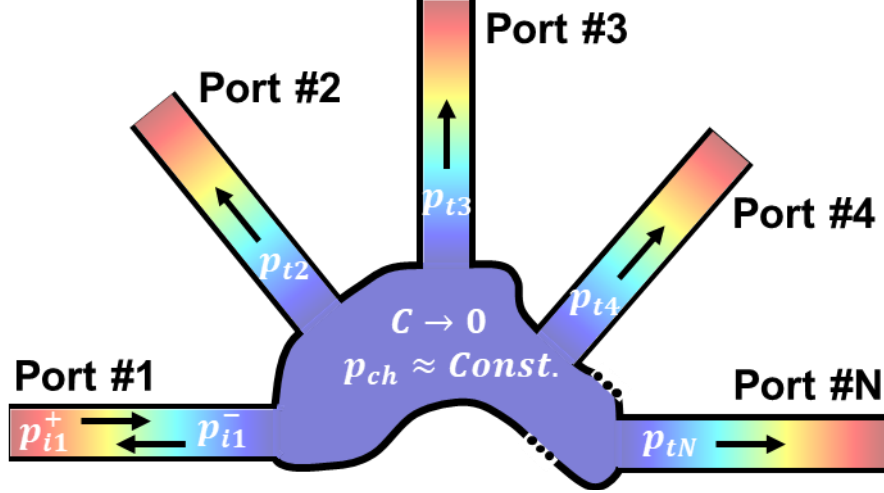


Figure 12. Arbitrarily shaped acoustic power divider formed by an intermediate channel with near-zero compressibility. Material property of the channel results in a quasistatic acoustic field, having uniform pressure everywhere. When channels meet the matching conditions derived in the text, the input power is fully transmitted and equally split among the outputs.

A. Equi-phase power division

Specifically, we assume that the effective compressibility C_{eff} is near zero, and thus $\lambda =$

$\frac{1}{f} \sqrt{\frac{1}{C_{\text{eff}} \rho_{\text{eff}}}} \rightarrow \infty$. Channel 1, with characteristic acoustic impedance Z_1 , carries the input

signal, while the other channels, with characteristic acoustic impedance Z_j , connect to the

output ports. Z_j is defined as $Z_j = \frac{\rho_j c_j}{A_j}$, where $j \in [2, N]$ is the index of each output channel

and ρ_j , c_j and A_j are respectively the mass density, sound velocity and cross-sectional area of the channel j .

The pressure in the CNZ medium connecting the different channels is constant because $\lambda \rightarrow \infty$, hence the pressure boundary condition becomes

$$p_{i1}^+ + p_{i1}^- = p_{ch} = p_{t2} = p_{t3} = \dots = p_{tN} \quad (3.12)$$

where p_{ch} is the uniform pressure in the CNZ medium. Eq. (3.12) implies that

$$1 + R_1 = T_2 = \dots = T_N \quad (3.13)$$

where R_1 and T_x $x \in [2, N]$ are the reflection and transmission pressure coefficients of the input and output channels, respectively. For similarly sized cross-sections, the large characteristic impedance of the CNZ medium implies very poor matching and $R_1 = -1$. However, if the cross-sectional area of the CNZ buffer is much larger, as sketched in Figure 12, Z_{ch} can be impedance matched to any of the ports, as experimentally shown in Section 3.2 for acoustic tunneling between two ports. Interestingly, this tunneling is independent of the shape and form of the CNZ buffer, as long as the impedance matching condition is satisfied by increasing the overall cross-sectional area.

Hence, if we assume that the CNZ section is impedance matched to port 1, we can write generally for the volume velocity q :

$$q_{i1}^+ + q_{i1}^- = q_{ch} = q_{t2} + q_{t3} + \dots + q_{tN}, \quad (3.14)$$

which can be written in terms of pressure as:

$$\frac{p_{i1}^+}{Z_1} - \frac{p_{i1}^-}{Z_1} = \frac{p_{t2}}{Z_2} + \frac{p_{t3}}{Z_3} + \dots + \frac{p_{tN}}{Z_N}, \quad (3.15)$$

and in terms of reflection and transmission coefficients:

$$1 - R_1 = Z_1 \left(\frac{T_2}{Z_2} + \frac{T_3}{Z_3} + \dots + \frac{T_N}{Z_N} \right). \quad (3.16)$$

By replacing Eq. (3.13) into Eq. (3.16), the reflection and transmission coefficients of the input and output channels are derived and expressed respectively by

$$R_1 = \frac{1 - Z_1 \sum_{j=2}^N Z_j^{-1}}{1 + Z_1 \sum_{j=2}^N Z_j^{-1}} \quad (3.17)$$

$$T_x = 1 + R_1 = \frac{2}{1 + Z_1 \sum_{j=2}^N Z_j^{-1}}, x \in [2, N], \quad (3.18)$$

where the power transmission and reflection coefficients are defined by $T_{\Pi x} = \frac{Z_1}{Z_x} |T_x|^2$ and

$R_{\Pi 1} = |R_1|^2$, respectively [3]. For a two-port structure with $Z_1 = Z_2$, for instance, no signal

is reflected back towards the input, while all of the energy is tunneled through the intermediate CNZ buffer towards the output, independent of its shape or size.

Let us now consider the special case for which the characteristic acoustic impedance of the input/output channels are all the same ($Z_1 = Z_2 = \dots = Z_N$), corresponding to transmission lines consisting of the same medium and physical cross section, for instance. This assumption results in the following expressions for the reflection and transmission coefficients for amplitude and power:

$$R_1 = \frac{2}{N} - 1, R_{\Pi 1} = \frac{4}{N^2} - \frac{4}{N} + 1 \quad (3.19)$$

$$T_x = \frac{2}{N}, T_{\Pi x} = \frac{4}{N^2}, \quad (3.20)$$

where N is the total number of ports in the power divider ($N \geq 2$). The relations (3.19) and (3.20) reveal that: (i) since the CNZ buffer is assumed to be lossless, energy conservation is satisfied with $R_{\Pi 1} + (N - 1)T_{\Pi x} = 1$; (ii) if the number of output channels is increased, the amount of reflected power rises; (iii) the amount of transmitted power in each channel is inversely proportional to the square of the number of output ports. These findings are consistent with the quasi-static nature of the CNZ buffer, for which what matters to evaluate the transmission are the overall area of the output versus the input ports normalized to their impedance.

B. Equi-phase zero-reflection power division

As a corollary of the previous findings, we find from Eq. (3.17) and Eq. (3.18) that, when the number of output ports is larger than one, the reflected power can be suppressed if

$$Z_1^{-1} = \sum_{j=2}^N Z_j^{-1}. \quad (3.21)$$

Hence, as far as this relation is satisfied, the input power can be ideally split among the output ports with equal phase and without reflection, irrespective of the distribution of the acoustic characteristic impedance of the output ports.

C. Equi-phase and equi-amplitude zero-reflection power division

While suppressing the reflection in the input channel, the output power can be evenly divided among the ports if the characteristic impedance of each output port (Z_j) is equal. To demonstrate this property, Eq. (3.21) can be further expanded using the material properties as well as geometrical dimensions of the channel, as

$$\frac{A_1}{\rho_1 c_1} = \frac{A_2}{\rho_2 c_2} + \frac{A_3}{\rho_3 c_3} + \dots + \frac{A_N}{\rho_N c_N}. \quad (3.22)$$

If the material inside the input and output channels is the same, or in other words the specific acoustic impedances of the channels are equal, the relation above is simplified to

$$A_1 = A_2 + A_3 + \dots + A_N. \quad (3.23)$$

Finally, in order to create equi-amplitude output $A_2 = A_3 = \dots = A_N$, This relation reveals a matching condition for the CNZ power divider that completely suppresses the reflected power from the input. For this to happen, the sum of the cross-sectional areas of the output channels should be equal to the cross-sectional area of the input channel.

3.5.2 Realistic Implementation and Simulations

Now we turn to the realistic implementation of a CNZ power divider. In Section 3.2, we showed that it is possible to implement an effective near-zero compressibility by exciting a hard-walled acoustic waveguide with a rectangular cross section at exactly the cutoff frequency of its (2,0) mode. As mentioned above, in order to achieve good impedance matching the ratio of the cross-sectional areas of the input/output waveguides to the intermediate tunneling channel should be made very small, i.e.,

$$A_j \ll A_{\text{ch}} \quad \forall j \in [1, N], \quad (3.24)$$

where A_{ch} is the cross-sectional area of the intermediate channel exhibiting CNZ properties and N is the total number of waveguides connected to the intermediate channel.

Following these principles, a finite element model was constructed in Comsol Multiphysics, employing the Pressure Acoustics module and frequency domain solver. Sound hard boundary conditions were used to model the walls of the input/output waveguides and the intermediate channel, and air was chosen as the filling material. The final layout is shown in the inset of Figure 13 with dimensions $a = 0.450 \text{ m}$, $b = 0.382 \text{ m}$ and $L = 0.79 \text{ m}$, similar to the experimental setup in Section 3.2.

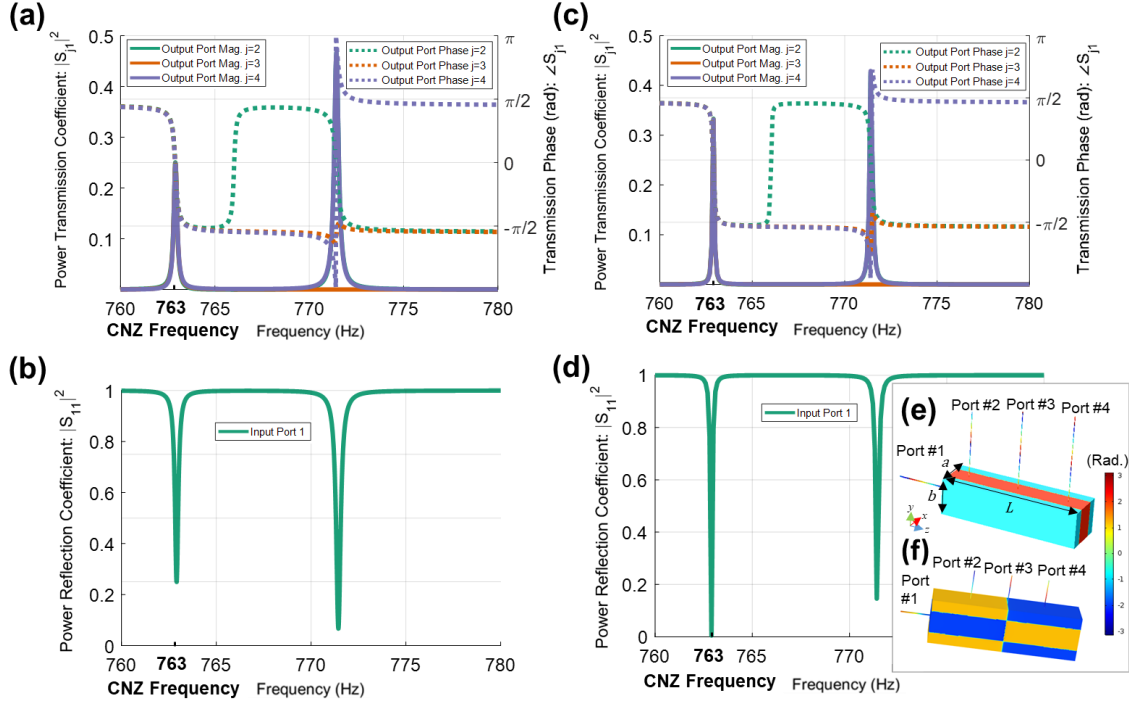


Figure 13. Geometrical configuration and phase distribution of the uniform-phase equal-amplitude acoustic power divider (inset-bottom-right). The system is composed of hard-walled cylindrical waveguides for the input (port #1) and outputs (port #2 – #4), connected to an intermediate hard-walled channel with rectangular cross section. Operated at its second cut-off frequency, the intermediate channel performs as an effective CNZ medium and results in uniform-phase output signals. Moreover, equal cross-sectional areas of the output waveguides results in equal distribution of output power among them (a) Power transmission coefficient and phase show that the power is divided evenly ($|S_{j1}| = 0.25$ where $j \in [2,4]$) with equal phase among three output ports at the CNZ frequency of 763 Hz. (b) Power reflection coefficient reveals that we observe nonzero reflection at the input port ($|S_{11}| = 0.25$ at 763 Hz) and therefore not all of the power is transmitted. (c) Power transmission coefficient and phase of the power divider from (a), but modified such that the cross-sectional area of the input waveguide is equal to the sum of the cross-sectional areas of the output waveguides ($r_i = 6.3 \text{ mm}$, $r_o = 6.3/\sqrt{3} \text{ mm}$). The input signal is split evenly ($|S_{j1}| = 1/3$) and with the same phase among the three output ports at the CNZ frequency of 763 Hz. (d) The reflected power at the CNZ frequency has now been completely suppressed due to the matching condition, dictated by Eq. (3.23). (e) Spatial phase distribution at the CNZ frequency, showing the uniformity of the phase of the delivered output signals and the geometrical parameters (f) Spatial phase distribution for the higher-order mode at 773 Hz. The dimensions of the CNZ channel are $a = 0.450 \text{ m}$, $b = 0.382 \text{ m}$ and $L = 1.5 \text{ m}$. The radius of the input/output channels are $r_i = r_o = 6.3 \text{ mm}$.

A. Lossless case

Figure 13(a)-(b) show the power reflection and transmission coefficients for a 4-port CNZ power divider. In this configuration, all input/output waveguides have the same cross-sectional areas. The output ports are placed at the top-center of the channel, where the phase of the CNZ resonance is uniform and equal to the input phase. At the CNZ frequency (763 Hz), this geometry results in equal power division with uniform phase to all the output ports (Figure 13(a)); however, there is some reflection of the incident energy, namely 25% of the power is reflected back (Figure 13(b)), in agreement with Eq. (3.19) and Eq. (3.20).

In order to suppress the reflected power and couple all the input energy to the output of the system, a second configuration was devised following Eq. (3.23), as shown in Figure 13(c)-(f). In this case, all the dimensions and materials are kept constant with respect to Figure 13(a)-(b), except for the cross-sectional areas of the output waveguides, which are each smaller by a factor of three. Therefore, the sum of the cross sections of the outputs is equal to the cross section of the input channel ensuring the matching condition. By examining this figure, we can verify impedance matching at the CNZ frequency and therefore full power transmission of the input signal with zero reflection at the input, while the power is split evenly among the three output channels with equal phase.

The CNZ mode profile corresponds to a standing wave in the transverse plane of Figure 13(e), where the frequency of the mode depends upon the width of the intermediate channel a and is independent of the length L and the height b [given that Eq. (3.24) is also satisfied]. This property is in contrast with the higher-order tunneling resonances (the second peak in Figure 13(a) and Figure 13(c)), which are largely affected by variations in the length of the

channel, analogous to Fabry-Perot resonances [28]. The phase distribution of this higher-order mode is not uniform along the channel length (see Figure 13(f)), and therefore does not provide power equally to all ports.

It should be noted that the matching condition (3.23) does not require all output ports to have the same cross-sectional area. Interestingly, when this condition is met with unequal cross sections, the power distribution can be tuned at each of the output ports, as shown in Figure 14, still ensuring impedance matching at the input port. In this case, the geometrical and material parameters are kept constant with respect to Figure 13(e), except that the cross-sectional areas of the outputs were set to $A_2 = A_1/6$, $A_3 = A_1/3$ and $A_4 = A_1/2$, such that $A_1 = A_2 + A_3 + A_4$ and Eq. (3.23) is satisfied. In turn, this results in an impedance-matched power divider, where no reflection is seen at the input, but where the amount of power distributed to each output is equally proportional to A_j/A_1 , such that $P_2 = P_{\text{in}}/6$, $P_3 = P_{\text{in}}/3$, and $P_4 = P_{\text{in}}/2$. This tuning of output power can prove useful in several applications. An example may be in making interferometric measurements on a lossy sample, where there are two output waveguides: one being an empty reference waveguide (without material loss), and the second one being filled by some lossy material [136]. By increasing the output power to the waveguide containing the material sample, the system can be designed to compensate for the material loss and then compare the phase of two signals having equal power.

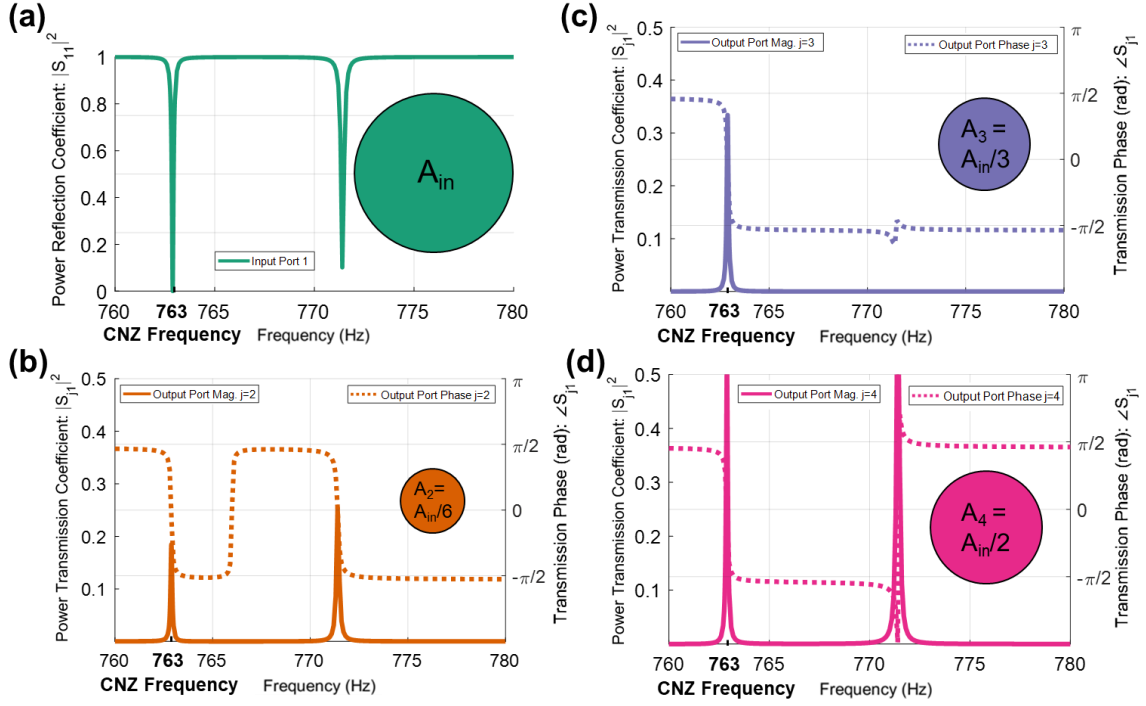


Figure 14. Matching condition for the input/output waveguides in the power divider, Eq. (3.23), is met with unequal cross-sectional areas at each output, which allows zero reflection at the input as well as control over the power supplied to each output port. The geometrical parameters of the power divider are similar to Figure 13(e) except for the cross-sectional areas of each input/output waveguide, which are indicated by the proportionally-scaled insets in all plots ($r_i = 6.3 \text{ mm}$, $r_{o2} = 6.3/\sqrt{6} \text{ mm}$, $r_{o3} = 6.3/\sqrt{3} \text{ mm}$, $r_{o4} = 6.3/\sqrt{2} \text{ mm}$). **(a)** As the matching condition of Eq. (3.23) is satisfied, the reflected power remains zero at the CNZ frequency of 763 Hz. **(b)** The cross-sectional area of the second output port is $A_2 = A_{in}/6$ and the output power is $|S_{21}|^2 = 1/6$. **(c)** $A_3 = A_{in}/3$ and $|S_{31}|^2 = 1/3$. **(d)** $A_4 = A_{in}/2$ and $|S_{41}|^2 = 1/2$.

Another unique feature of the proposed configuration is that the phase of the (2,0) CNZ mode within the channel is flipped by 180 degrees near the boundaries on the sides of the channel, (see Figure 15, *top-right inset*; also compare with the inset of Figure 13). In the example demonstrated in Figure 15, all geometrical and material parameters are the same as in Figure 13(e), except for the location of the output waveguides, which are placed with

two outputs along the side and one output along the end-face. It can be seen that impedance matching, and thus full power transmission, is still achieved (Figure 15(a)), even in this scenario, where the output ports are installed transverse to one another. More importantly, the signal that is coupled to the side channels (#2 and #3) is the phase inverted (180-degree phase flipped) version of the output signal along the end face (channel #4). Figure 15 also highlights the capability of inverting the phase of some output channels, while preserving the input phase of the others.

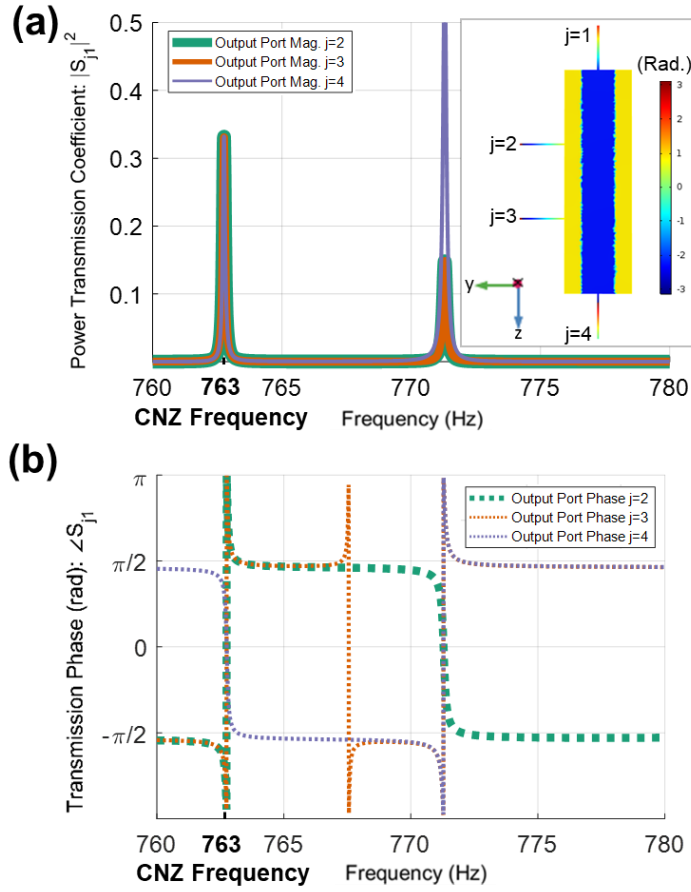


Figure 15. The geometrical parameters of the power divider are kept identical to Figure 13(e), except that the output ports #2 and #3 are placed along the side of the intermediate channel, while port #4 is placed at the end (see spatial phase profile, top-right inset). **(a)** Power is evenly divided among the three output channels at the CNZ frequency of 763 HZ. **(b)** At this frequency, the phase is flipped by 180 degrees at the output of both side channels, while the phase is 0 degrees at the interface of port #4.

As previously discussed, CNZ-based series power dividers are also expected to have invariant performance with changes in the length and height of the buffer channel. To demonstrate this property, a more general scenario of power divider is shown in Figure 16, where both the length and height are changed with respect to the previous figures; additionally, the number of output ports is increased to five, and the output ports are placed

along all faces of the intermediate channel (except for the input face). In this case, the cross-sectional area of the input port is the same as in Figure 13(c) to Figure 15, however the cross-sections of all output ports are now equal to $A_1/5$, in order to satisfy Eq. (3.23). We see that impedance matching still occurs at the CNZ frequency (Figure 16(b)), while the phase of the output signal will be either 0 or 180 degrees, depending upon the placement of each port (see Figure 16(a)).

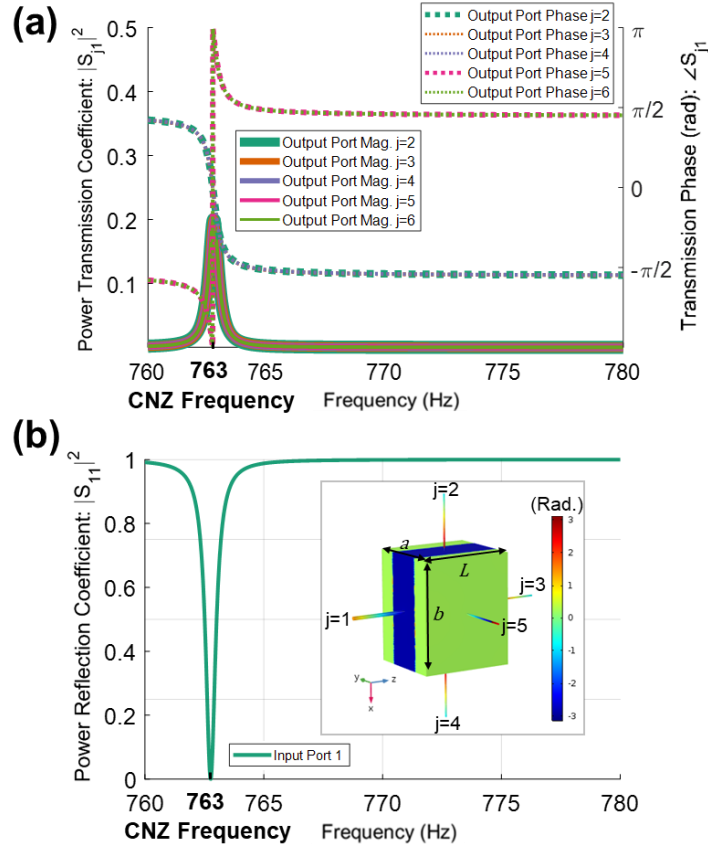


Figure 16. A more general case of the uniform-phase acoustic power divider, in which the height and length of the channel are varied. This example has a total of 5 output ports (one on each opposing face of the intermediate channel). The power divider maintains uniform phase for any port placed within $\lambda/4$ of the center of the channel and the output phase flips by 180 degrees for any output waveguide that is placed elsewhere (see inset-bottom). **(a)** Power is divided evenly among the 5 output ports at the CNZ frequency of 763 Hz. The phase is zero at the CNZ frequency for ports #2, #3, and #4, and the phase is 180 degrees for ports #5 and #6. **(b)** The reflected power remains zero at the CNZ frequency. The dimensions are $a = 0.450\text{ m}$, $b = 0.6\text{ m}$ and $L = 0.5\text{ m}$, $r_i = 6.3\text{ mm}$, and $r_o = 6.3/\sqrt{5}\text{ mm}$.

B. Modeling radiation losses and their relation to geometric scaling

Finally, we study the scalability of the proposed uniform-phase acoustic power divider and explain how choices of geometrical parameters can have significant impact in terms of both the radiation losses and the visco-thermal acoustic boundary layer loss. In this section, we will focus the discussion on radiation losses and will then consider the impact of visco-thermal losses in the following section.

Miniaturization of the power divider is interesting for two reasons: 1) to fit the device into a more compact acoustic system, and 2) to reduce sources of radiation losses compared to those observed experimentally in Section 3.2. To define miniaturization, we explore downscaling the main geometric parameters of the design in Figure 13(e), by a constant value, namely a, b, r_i , and r_o , which represent the width and length of the buffer channel and the radii of the input and output waveguides, respectively. The length L can also be scaled down in size, but this should not have a major impact on performance due to the length-invariance property of the supercoupling channel. Furthermore, it should be noted that downscaling makes it necessary to increase the operating frequency of the device in order to maintain operation at the CNZ mode. Finally, we would like to emphasize a fundamental and practical assumption that will be made below: we will *not* assume that the finite wall thickness scales down proportionally to the remainder of the geometry. This is not relevant in the ideal assumption of a hard wall, but it is important when realistic materials are considered. Because of practical limits in cost and weight, a low-audio-frequency CNZ supercoupling channel may require steel walls with thicknesses exceeding 20 mm in order to keep radiation losses reasonably low. Consequently, by obeying the

requirement that $a = \lambda$, such a device could weigh in excess of 120 kg. We show that, by considering scaling, a CNZ power divider may be constructed for operation at higher frequencies with much more reasonable choices for size, resulting in a device with lower values for radiation loss, weight, material cost, and geometrical footprint.

We can describe the radiation loss in the CNZ channel due to the finite thickness of a nearly sound-hard wall (e.g., a steel wall with $h = 1.5 \text{ mm}$) by characterizing the CNZ channel as a resonant cavity with a total quality factor, sum of a loaded and unloaded quality factor, given by $\frac{1}{Q} = \frac{1}{Q_{\text{loaded}}} + \frac{1}{Q_{\text{unloaded}}}$ [21]. The loaded quality factor represents the case when the input/output waveguides (which act as the load) are attached to the buffer, but the channel has perfect hard boundaries, resulting in no radiation. The unloaded quality factor represents the case when the input/output ports are blocked (in other words, the load is removed) and the boundaries allow for radiation. The former scenario has already been modeled in the numerical results from Figure 13 to Figure 16, where for example in Figure 13(c), the channel has $Q_{\text{loaded}} \equiv \frac{f_r}{\Delta f} \approx 6400$. This value can change slightly depending upon length, height, and number of output ports, however $Q_{\text{loaded}} \approx 6400$ will be used as a benchmark in the following example.

Now, we seek to find an expression for $Q_{\text{unloaded}} \equiv 2\pi \frac{W_{\text{stored}}}{W_{\text{rad}}}$ (where W_{stored} is the stored energy in the cavity per period and W_{rad} is the radiated energy per period). First, we approximate the power lost due to radiation from each transient reflection by using the power transmission coefficient through an acoustic slab with finite thickness h at normal incidence [2]:

$$T_{\pi c} = \frac{4}{4 \cos^2(k_{\text{steel}}h) + \left(\frac{Z_{\text{steel}}}{Z_{\text{air}}} + \frac{Z_{\text{air}}}{Z_{\text{steel}}}\right)^2 \sin^2(k_{\text{steel}}h)}. \quad (3.25)$$

The normal incidence assumption is justified because the monomodal (2,0) mode in the cavity resonates in the direction normal to the boundaries (x -direction as in inset of Figure 13) from which nearly all of the radiation should occur. Hence, a standing wave in the resonator with power $P_{\text{stored}} = \frac{|\bar{a}|^2}{2Z_{\text{air}}}$ will lose an amount of power $T_{\pi c} \frac{|\bar{a}|^2}{2Z_{\text{air}}}$ at the first transient reflection and it will lose $T_{\pi c}(1 - T_{\pi c}) \frac{|\bar{a}|^2}{2Z_{\text{air}}}$ at the second transient reflection (where there are two reflections in each period of the resonance of the intermediate channel and \bar{a} is the wave amplitude in the intermediate channel). If we assume that $(1 - T_{\pi c}) \approx 1$ (for example, for the intermediate channel of Figure 13 to Figure 16, $T_{\pi c} \approx 2.25 \times 10^{-4}$, with $Z_{\text{air}} = 415 \text{ Rayl.}$, $Z_{\text{steel}} = 4.7 \times 10^7 \text{ Rayl.}$, $k_{\text{steel}} = \frac{\omega}{c_{\text{steel}}}$, and $c_{\text{steel}} = 6100 \text{ m/s}$) then the power radiated upon each reflection is $T_{\pi c} \frac{|\bar{a}|^2}{2Z_{\text{air}}}$ with a total of two reflections per period. This results in a radiated power per cycle $P_{\text{rad}} = T_{\pi c} \frac{|\bar{a}|^2}{Z_{\text{air}}}$ and in terms of energy we have $W_{\text{rad}} = \frac{2\pi}{\omega} P_{\text{rad}}$. Next, in order to find W_{stored} , it is assumed that the stored energy per period in the resonator is twice the energy density of a half-period multiplied by the length of the cavity, meaning $W_{\text{stored}} = 2 \frac{P_{\text{stored}}}{c_0} L = 2 \frac{\frac{|\bar{a}|^2}{2Z_{\text{air}}}}{c_0} L = \frac{|\bar{a}|^2 L}{Z_{\text{air}} c_0}$, where c_0 is the speed of sound in the medium. Finally, we find

$$Q_{\text{rad}} \equiv Q_{\text{unloaded}} \equiv 2\pi \frac{W_{\text{stored}}}{W_{\text{rad}}} = \frac{\omega L}{T_{\pi c} c_0} = \frac{2\pi}{T_{\pi c}} \quad (3.26)$$

where again, $T_{\pi c}$ is the power transmission coefficient from Eq. (3.25) and $a = \lambda$ for the (2,0) CNZ mode.

Next, we use coupled mode theory to derive a first-order approximation for the amount of power radiated from the cavity [137]:

$$\frac{d\bar{a}}{dt} = (i\omega_0 - \gamma)\bar{a} + \kappa s_{\text{inc}}. \quad (3.27)$$

Here, \bar{a} is the mode amplitude in the cavity, ω_0 is the cavity resonance frequency, $\gamma = \gamma_{\text{loaded}} + \gamma_{\text{unloaded}} = \frac{\omega_0}{2Q}$ is the total decay rate, κ is the coupling coefficient, and s_{inc} is the input waveform. Assuming that we are operating the cavity at the CNZ frequency, $\omega = \omega_0$ and $s_{\text{inc}} = e^{i\omega_0 t}$. From this, we find

$$|\bar{a}| = \left| \frac{\kappa}{\gamma} \right| \quad (3.28)$$

and, given that $\kappa^2 = 2\gamma_{\text{loaded}}$ and $P_{\text{loss}} = 2\gamma_{\text{unloaded}}|\bar{a}|^2$ [137],

$$P_{\text{loss}} = 2\gamma_{\text{unloaded}} \frac{|\kappa|^2}{\gamma^2} = \frac{4\gamma_{\text{unloaded}}\gamma_{\text{loaded}}}{(\gamma_{\text{unloaded}} + \gamma_{\text{loaded}})^2} = \frac{4Q_{\text{unloaded}}Q_{\text{loaded}}}{(Q_{\text{unloaded}} + Q_{\text{loaded}})^2}, \quad (3.29)$$

where P_{loss} represents the normalized power loss due to radiation and we used the relations

$$\gamma_{\text{unloaded}} = \frac{\omega_0}{2Q_{\text{unloaded}}} \text{ and } \gamma_{\text{loaded}} = \frac{\omega_0}{2Q_{\text{loaded}}}.$$

This expression can now be used to approximate the power radiated from the cavity with an acoustic boundary of finite thickness and finite impedance. For illustrative purposes, we will consider two cases:

1. $f_0 = 763 \text{ Hz}$, corresponding to the examples presented in Figure 13 to Figure 16, with an intermediate channel of width equal to 45 cm , but now with a steel wall of finite thickness equal to 1.5 mm , instead of an ideal hard boundary;
2. $f_0 = 10,000 \text{ Hz}$, corresponding to a power divider that has all dimensions downscaled proportionally to case 1, resulting in a significantly smaller channel width of 3.4 cm , however having the same steel wall thickness of 1.5 mm .

From Eq. (3.25), the first case results in $T_{\pi c} \approx 2.25 \times 10^{-4}$ and $Q_{\text{unloaded}} = 2.80 \times 10^4$. Combining these values with the numerical results of $Q_{\text{loaded}} \approx 6400$, we find from Eq. (3.29) that $P_{\text{loss}} \approx 0.61$, estimating very high radiation loss at this size scale. In the second case, the scalability of the lossless Helmholtz equation ensures that the *loaded* quality factor of the smaller power divider is the same as in case 1. Given the new value of k_{steel} at 10 kHz in Eq. (3.25), we observe that $T_{\pi c} \approx 1.31 \times 10^{-6}$ and $Q_{\text{unloaded}} = 4.80 \times 10^6$, resulting in a much lower $P_{\text{loss}} \approx 0.01$ from Eq. (3.29). The significantly lower value for $T_{\pi c}$ in the second case (with a smaller intermediate channel) is intuitively expected, due to the walls being much thicker with respect to the wavelength, changing from $\frac{\lambda}{l} \approx 300$ in the first case to $\frac{\lambda}{l} \approx 23$ in the second case. These results confirm that downscaling the size of the intermediate channel and consequently increasing the operating frequency, while keeping the wall thickness constant, can significantly reduce radiation loss from the CNZ power divider.

C. Influence of the visco-thermal acoustic boundary layer

Despite the theoretical benefits of downscaling the size of the system, one major barrier that exists is acoustic boundary layer loss, which results from the viscosity of the medium in contact with the boundary as well as the thermal conductivity of the waveguide perimeter. Due to this mechanism, losses within the input and output waveguides are expected to increase as their sizes are decreased [2],[138]. Therefore, one potential problem resides in the fact that the boundary layer loss can become a dominating factor in the power

divider, due to the vanishingly small radii of the input/output waveguides as the entire device is downscaled and we continue to satisfy Eq. (3.24).

In order to mitigate the impact of increased boundary layer loss due to miniaturization of the power divider, we conducted a parametric study to examine the effect of increasing the surface areas of the input/output waveguides relative to the cross-sectional area of the intermediate channel's input face. It was found that, as the size of the input waveguide is increased, both phase uniformity and impedance matching of the CNZ mode begin to degrade. Figure 17(a) and Figure 17(b) show an example in which the radius of the largest waveguide is increased to $a/8$ (where a is the width of the intermediate channel) and the radii of all output waveguides are equal to $a/8\sqrt{5}$ in order to satisfy Eq. (3.23). The increased size of the waveguide radius with respect to the width of the intermediate channel results in degradation of impedance matching, an increase of the reflected power, and uneven power division (with respect to the previous configurations of Figure 13(e) through Figure 16). Here, the power reflection coefficient reaches a minimum value of 0.03 and it can be compared to previous configurations, which fully satisfy Eq. (3.24), and show a minimum reflected power close to 0.

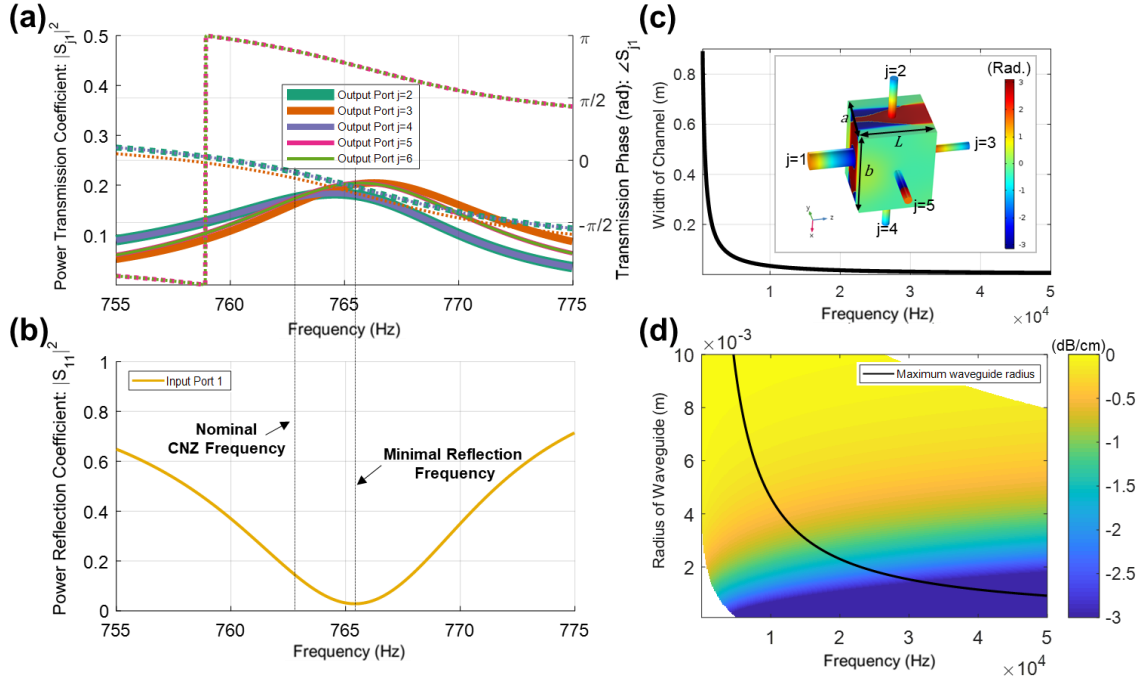


Figure 17. Scaling limitations for the acoustic power divider. Increasing the size of the input waveguide results in a channel that no longer has uniform phase and the power division becomes uneven. **(a)** Power transmission coefficients (left axis, solid lines) and phase (right axis, dashed lines) for ports #2 – #6 when the radius of the input waveguide is $a/8$, where $a = 0.450$ m is the width of the intermediate channel. Note that peak power division no longer occurs at the same frequency for each port, although the output power varies by a maximum of 11.5% in this case. The output transmission phase along the central ports ($j = 2, 3, 4$) has increased from zero in the previous case (Figure 16) to $\sim \frac{\pi}{4}$ and varies by a maximum of 0.15 rad. **(b)** Power reflection coefficient for an input waveguide radius of $a/8$, which has been degraded to 0.03 (compared to the 0 power reflection coefficient of Figure 16) **(c)** Variation of the CNZ frequency for a hard-hard channel (where uniform-phase power division can be achieved) as a function of the width of the channel, a . **(d)** Visco-thermal acoustic boundary layer loss as a function of frequency and waveguide radius. The black curve represents the limit where input radius reaches to $a/8$. Below the black curve, all choices of radius and frequency can result in power dividers with approximately uniform phase and equal power splitting. Note the units of loss are dB/cm as we are interested in centimeter-scale devices.

As dictated by Eq. (3.23), we expect the power to be divided equally among the output ports, with power transmission coefficient of 0.2 for each output channel. However, in this case the power is distributed a bit unevenly at each port, where the minimum power transmission coefficient is 0.181 at port #2 and port #4, and the maximum power transmission coefficient is 0.204 at ports #3, #5, and #6. This corresponds to a maximum variation of power transmission of 11.5% with respect to the expected value of 0.2. Finally, the phase of the outputs along the central channel are no longer close to zero, but each have shifted to approximately $\pi/4$ rad. Therefore, we find a clear trade-off in the performance of the power divider as we explore miniaturization: we can trade uniformity of phase and amount of reflection or transmission, for decreased boundary-layer loss at miniaturized dimensions.

The impact of boundary layer loss at various size scales can also be quantified. By considering the scale invariance of Helmholtz equation in the waveguides and intermediate channel (without boundary layer loss), all dimensions of the power divider can be decreased proportionally while the frequency is increased, such that the size of each dimension with respect to λ stays constant. This theoretically yields a device with identical performance, except for the considerations of visco-thermal loss, which depends upon both the frequency and dimension of each waveguide, and the radiation loss that depends upon the thickness of the waveguide and intermediate channel. Previously we showed that radiation loss can be controlled independently by setting the thickness of the walls of the intermediate channel. Now we can predict the boundary layer loss upon scaling the power

divider by considering the smallest input/output waveguides in the system, which is the limiting factor contributing most to loss.

We can express the particle velocity in the waveguide as $u = u_0 e^{-\alpha z} e^{j(\omega t - \beta z)}$,

where for a gas medium

$$\alpha = -Im \left\{ \frac{\omega / c_0}{\sqrt{1 - \frac{2}{r} \left(1 + \frac{\gamma_{sp}^{-1}}{\sqrt{Pr}} \right) \sqrt{\frac{v}{j\omega}}}} \right\} \quad (3.30)$$

with r being the radius of the cylindrical input/output waveguide, γ_{sp} is the ratio of specific heats, Pr is the Prandtl number, and v is the kinematic viscosity [2]. By assuming standard atmospheric conditions in air, the implications of Eq. (3.30) are considered in Figure 17(d), where we plot the level of insertion loss as a function of waveguide radius and frequency of operation. In particular, we highlight the maximum waveguide radius (black curve) that provides the degradation level in performance reported in Figure 17(a) and Figure 17(b). This result shows that it is possible to construct an acoustic power divider within an acceptable phase and amplitude variation range by selecting any point in Figure 17(d) below the black curve. Increasing frequency will result in downscaling the dimension of the coupling channel (where $a = \lambda$), while reducing the radius of the input/output waveguide will improve the phase uniformity. Improved phase uniformity comes at the cost of increased boundary-layer loss. Therefore, careful consideration of the signal requirements for each application should be made before choosing the channel size, the size of the input/output waveguides, and the frequency of operation. Furthermore, an alternate route for improving phase uniformity is through increasing the height of the

channel (b), which has a negligible impact on the operating frequency of the power divider, as shown in Section 3.2. Finally, it should be noted that the dominant loss mechanism in a given application can be either radiation loss or visco-thermal loss, depending on the requirements in terms of material, boundary thickness, frequency, and required length of the connecting channels.

3.6 CONCLUSIONS

In Section 3.2, we presented theoretical and experimental validation of a straightforward way of realizing zero compressibility acoustic wave propagation in waveguides, by exciting a higher-order mode at the cut-off frequency. Our theoretical results accurately capture the physics behind this anomalous tunneling, and our experiments confirm large phase velocity and anomalous transmission independent of the channel length. In summary, we can describe the supercoupling phenomenon as a dispersive impedance matching condition, which occurs when the coupling channel (with smaller characteristic impedance than the input waveguide) has an input impedance that appears nearly infinitely stiff. At this matching condition, the phase velocity approaches infinity, as long as S_2/S_1 is sufficiently large. Under this condition, we achieve full amplitude transmission and total conservation of the phase, independent of the height and length of the coupling channel.

Moreover, our results show that a hard-wall waveguide, when driven near the cut-off frequency of a higher-order mode, exhibits compressibility-near-zero effective material

properties, and may be thought of as consisting of two effective soft boundaries, along which the pressure field is equal to zero and the uniform phase of the tunneling mode flips by π . Quite surprisingly, it is possible to suppress the excitation of all other modes in the waveguide, including the dominant plane-wave mode, thanks to the largely mismatched cross-section at the connecting interfaces.

We have also shown that an acoustic power divider can be realistically implemented with interesting features, such as the capability of transmitting power with uniform phase to an arbitrary number of output ports, independent of the placement of the ports along the central region of the channel. Furthermore, it was shown that this power divider can maintain its functionality, independent of changes in length and height of the coupling channel, given that there is a large difference between the cross-sectional areas of the input/output waveguides and the cross-sectional area of the coupling channel. Moreover, it is possible to control the amplitude and phase (in increments of π radians) delivered to each output port without compromising impedance matching. This approach also overcomes limitations of traditional meander-line-based series power dividers, which require the output ports to be constrained to specific locations along the length of the component. We have also evaluated the trade-offs between visco-thermal loss, radiation loss, phase uniformity and power splitting in realistic designs, offering a practical avenue towards compact and low-loss CNZ supercoupling power dividers. Our work opens possibilities for centimeter-scale acoustic supercoupling devices with a variety of potential applications. For example, when used in a pulse-echo measurement system (such as for nondestructive evaluation, acoustic imaging, or sonar), this device can be used as a power

divider with near-zero phase filter properties to remove noise or clutter from the received signal without the need for an additional band pass filter in the receive chain. Furthermore, the capability of adjusting the output power levels (as shown in Figure 14), can be leveraged in the design of loss-compensating acoustic interferometers. Finally, the power divider can be used for multiplexing acoustic signals with opposite phases and differing weights. We envision a wide range of applicability of CNZ supercoupling, for use in acoustic sensing [139], for the tailoring of acoustic radiation patterns [27][140], for acoustic lensing [141], and for enhanced acoustic nonlinearities and sound-matter interactions [29],[58].

Chapter IV: Simultaneous Transmit and Receive with Passive Circuit Elements at Ultrasonic Frequencies

4.1 APPROACH

An overview of a Simultaneous Transmit and Receive (STAR) system from Chapter II is reproduced in Figure 18 for convenience. The figure shows STAR operation with a single transducer, such that the STAR system is employed to isolate the transmitted and received signals while the transducer simultaneously sends and receives over the same frequency band.

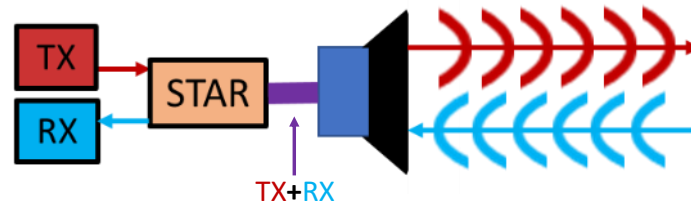


Figure 18. Overview of a single-transducer STAR acoustic system.

Common system design approaches for Simultaneous Transmit and Receive (STAR), which have primarily been implemented in Radio Frequency (RF) systems thus far, leverage the capabilities of difference amplifiers to accurately subtract the transmitted signal from a compensation signal in order to perform Self-Interference Cancellation (SIC), see Figure 19(a). In that approach, the compensation signal is related to the original signal intended for transmission, but it also includes the frequency response of the transmit chain, which considers the impedance of the acoustic transducer, and often includes the response

of the power amplifier. The difference amplifier approach for STAR takes advantage of the amplifier's ability to provide gain and accurate signal subtraction, with typical accuracy around 60 dB. However, a major challenge of implementing this system is that the acceptable phase error in the estimated compensation signal is very small, e.g. even errors of 0.1 deg. can cause the amplifier output to vary by more than 20 dB [90].

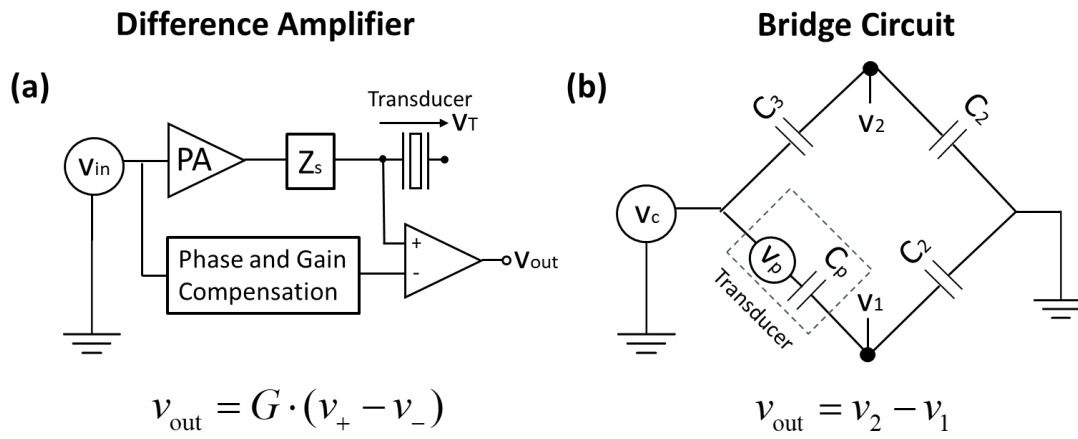


Figure 19. Comparison of analog approaches to self-interference cancellation for acoustic measurement systems. The diagram in (a) is similar to the circuit first proposed for acoustics in [90] and further studied in [22], [71], [86], [88], [91] while the system in (b) is similar to the one proposed for ultrasonic applications in [24] and further studied in [97]–[104].

An alternative approach, which will be explored in this work, is based on a passive bridge circuit first introduced by Dosch and Inman [24], and later expanded upon by Anderson et al. [97] for co-located sensing and control of structural vibrations. These early works implemented the bridge circuit with closed-loop control schemes that modeled the piezoelectric actuator as an ideal capacitor. The passive bridge circuit model is illustrated

in Figure 19(b). The circuit is balanced with external capacitors C_2 and C_3 that match the capacitance of the piezoelectric component, resulting in an output voltage that is proportional only to the signal one seeks to detect, v_p , and independent of the input voltage, v_c . In these circuits, $C_3 \approx C_p$, where C_p is the capacitance of the piezoelectric sensor, and the capacitors on the right side of the bridge are both approximately equal, yielding a compact relationship for the output voltage:

$$v_{\text{out}} = v_2 - v_1 \approx \frac{C_p}{C_p + C_2} v_p. \quad (4.1)$$

There are various advantages and disadvantages of applying a passive bridge circuit approach for STAR, as compared to the difference amplifier approach. The difference amplifier requires the generation of a separate compensation signal, which is achieved by a process called impulse response estimation. This can ideally result in a significant amount of SIC (> 50 dB) [91]. However, some difficulties associated with this approach include the use of an amplifier, which requires additional external power to drive the amplification, and that the amplifier itself can add nonlinearities and noise to the system. Furthermore, limits on the phase noise of the system can have a significant impact on the ability of the difference amplifier to effectively perform broadband cancellation [90]. Therefore, the bridge circuit of Figure 19(b) is considered as an alternative approach for STAR at acoustic frequencies. The bridge circuit leverages a balanced set of impedances to cancel the input voltage signal rather than actively cancelling the transmit voltage, thereby eliminating the need to generate a compensation signal by using any form of impulse response estimation.

Furthermore, all components in the design can be selected to be passive components and, in that case, there will not be any power sources required for the cancellation process.

The principal difficulty of the bridge circuit approach resides in obtaining an accurate measure of the frequency-dependent complex impedance of all circuit components along with any parasitic resistances or reactances that may be present. Addressing these complications is one of the principal objectives of the work presented in this chapter. Furthermore, SIC with a bridge circuit has only been demonstrated for low frequency applications in vibrations and acoustic noise control. Therefore, a more generalized form of the bridge circuit design is explored and its implementation in acoustic measurement systems is considered, leading up to an experimental demonstration (Chapter V) of its use for ultrasonic STAR measurements using an off-the-shelf ultrasonic transducer.

4.1 LINEAR SYSTEM MODELS

A purely passive implementation of the bridge circuit for STAR acoustic applications is proposed, thus avoiding additional complexities in the system response that may result from the introduction of active components. To accomplish this feature while maintaining good electrical coupling to the acoustic transducer, a passive resistor-inductor-capacitor (RLC) impedance-matching circuit was added between the output of the signal source, denoted as v_{in} , and the input of the bridge as shown in Figure 19(a). The components in this model are also assumed to be complex impedances in general, rather than pure capacitances, which allows us to account for internal losses (due to dielectric loss, parasitic

resistances, and mechanical losses in the transducer that are transformed into the electrical domain) and to include a more general model of the acoustic transducer.

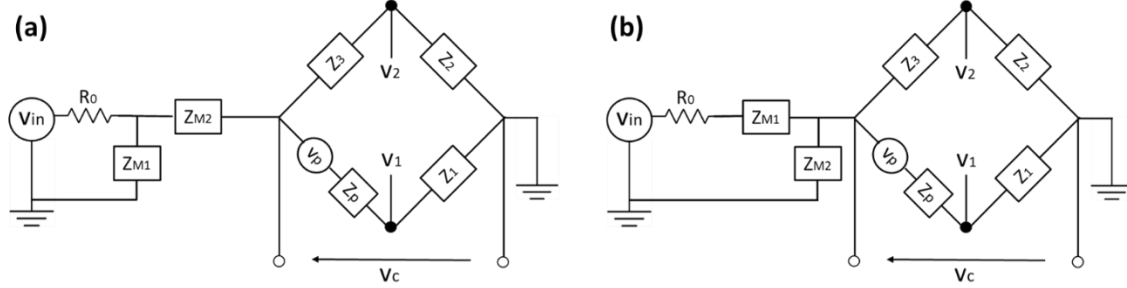


Figure 20. (a) Linear circuit model of the general impedance-matched bridge circuit for an acoustic transducer, which assumes that the real part of the bridge circuit impedance is less than R_0 . (b) Model for when the real part of the bridge circuit impedance is greater than R_0 . For both (a) and (b), the output voltage,

$$v_{out} = v_2 - v_1 \text{ will be independent of the input voltage } v_{in}, \text{ given that } Z_1 / Z_p = Z_2 / Z_3.$$

The circuit model provided in Figure 20(a) introduces Z_{M1} and Z_{M2} as the two passive matching components, which can be selected to be inductors or capacitors to match the impedance of the bridge circuit with that of the signal source. The matching impedances can also contain nonzero real parts, implemented as either parallel or series resistors, in order to adjust the quality factor and/or matching frequency. The layout in Figure 20(a) assumes that the real part of the load impedance is less than the real part of the input impedance of the bridge circuit. If the opposite were true, then the impedance matching solution would require Z_{M1} and Z_{M2} to be swapped (where Z_{M1} and Z_{M2} are passive RLC

components) such that Z_{M1} would be placed in series with R_0 while Z_{M2} would be placed across the termination of Z_{M1} and ground, as shown in Figure 20(b) [21]. The impedance Z_p along with the source v_p represent the complex impedance of the piezoelectric transducer and the voltage generated by the piezoelectric sensing, respectively. Finally, the elements Z_1 , Z_2 , and Z_3 represent RLC components that are used to match the impedance of the acoustic transducer and maintain good power coupling with the matching circuit and source. Solving the circuit in Figure 20(a) for the output voltage, it can be seen that

$$v_{out} \equiv v_2 - v_1 = C \cdot (A - B) \cdot v_{in} + (B + D) \cdot v_p, \quad (4.2)$$

where the coefficients are defined as

$$\begin{aligned} A &= \frac{Z_2}{Z_2 + Z_3}, \\ B &= \frac{Z_1}{Z_1 + Z_p}, \\ C &= \frac{1}{C_1 C_2 C_3}, \\ C_1 &= \frac{1}{Z_{M1}} + \frac{1}{Z_{M2}} + \frac{1}{R_0}, \\ C_2 &= \frac{1}{Z_3 + Z_2} + \frac{1}{Z_p + Z_1} - \frac{1}{C_1 Z_{M2}^2} + \frac{1}{Z_{M2}}, \\ C_3 &= R_0 \cdot Z_{M2}, \\ D &= \frac{A - B}{\frac{Z_p + Z_1}{Z_3 + Z_2} - \frac{1}{Z_{M2} + Z_{M2}^2 / Z_{M1} + Z_{M2}^2 / R_0} + \frac{1}{Z_{M2}} + 1}. \end{aligned}$$

This solution was validated with results from a numerical simulation run with National Instruments (NI) Multisim, shown in Figure 21(a)-(d). The figure displays the magnitude and phase of v_{out} with varied matching of component impedances, corresponding to a mismatch in the parameters A and B . This mismatch can arise due to numerous reasons, including variation in temperature and/or humidity, board parasitics, and variation due to natural manufacturing tolerances. The solution presented in Figure 21(a)-(b) show a variation of Z_p and Z_3 such that $C_3 / C_p = 1, 0.99, \text{ and } 0.95$, which corresponds to $|A / B| = 1, 0.995, \text{ and } 0.977$, respectively. It can be seen that an imperfect match of any of these impedances will result in drastic changes in the magnitude and phase of the output voltage associated with an induced resonance near the matching frequency of 500 kHz. Figure 21(c)-(d) present the magnitude and phase of v_{out} with varied matching of Z_1 and Z_2 , such that $C_3 / C_p = 1, 0.99, \text{ and } 0.95$, which correspond to a mismatch in the parameters A and B such that $|A / B| = 1, 1.005, \text{ and } 1.025$, respectively. In this case, the impedance mismatch again results in resonance for the output voltage at 500 kHz, however the antiresonance now follows the resonance in frequency, rather than preceding it.

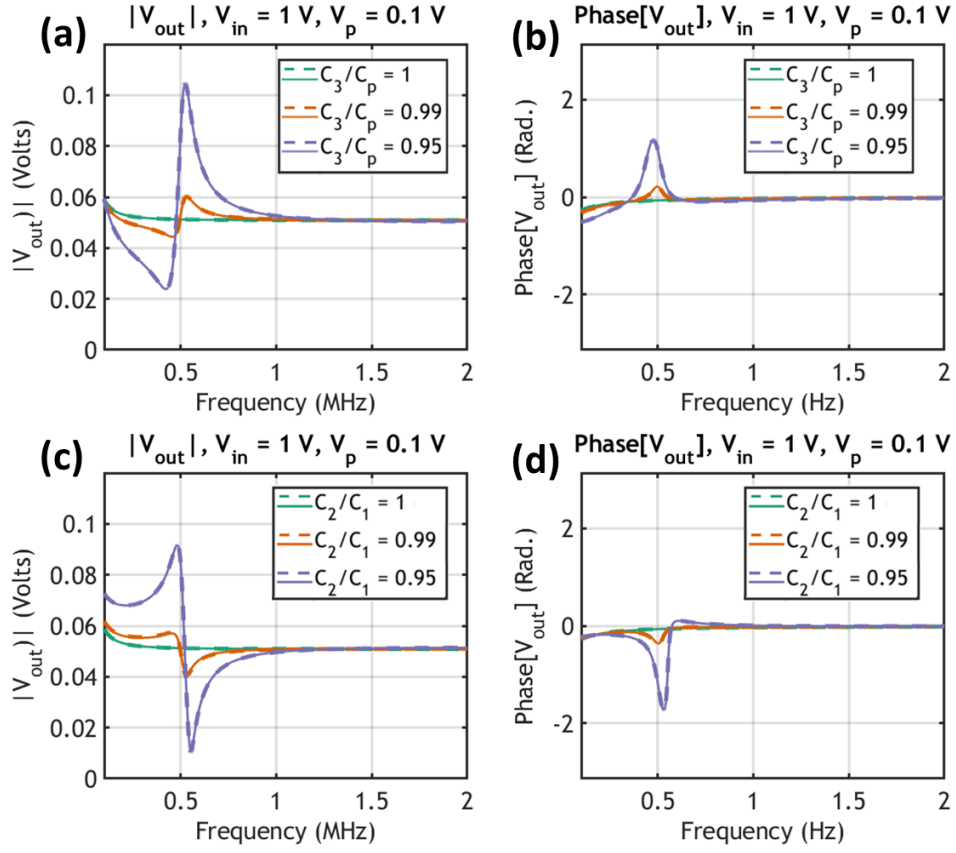


Figure 21. Analytical solution for the output voltage of the bridge circuit during STAR operation (solid line) overlaid with the numerical solution from National Instruments (NI) Multisim software (dashed line). **(a)-(b)** Magnitude and phase of v_{out} with varied matching of Z_p and Z_3 , corresponding to a mismatch in the parameters A and B such that $|A/B| = 1, 0.995$, and 0.977 . **(c)-(d)** Magnitude and phase of v_{out} with varied matching of Z_1 and Z_2 , which corresponds to a mismatch in the parameters A and B such that $|A/B| = 1, 1.005$, and 1.025 . Input parameters for (a)-(d) are presented in Table 3.

Table 3. Component values used to compute the output of the LC-matched bridge circuits as presented in the corresponding figures listed on the leftmost column.

All configurations assume that $v_{in} = 1.0v_{pk}$, $R_0 = 50\Omega$, $v_p = 0.1v_{pk}$,

$Z_p = 579pF \parallel 3.85k\Omega$, $Z_1 = 560pF$, and use the layout of Figure 20(a).

Figure	Z_{M1}	Z_{M2}	Z_2	Z_3
Figure 21(a)-(b)	3.48 nF ($m=1$) 3.38 nF ($m=0.99$) 2.89 nF ($m=0.95$)	183 μH ($m=1$) 183 μH ($m=0.99$) 184 μH ($m=0.95$)	560 pF	$m^*579 \text{ pF} \parallel$ $m^*3.85 \text{ k}\Omega$, $m=\{1, 0.99, 0.95\}$
Figure 21(c)-(d)	$m^*579 \text{ pF} \parallel$ $m^*3.85 \text{ k}\Omega$, $m=\{1, 0.99, 0.95\}$	183 μH ($m=1$) 183 μH ($m=0.99$) 185 μH ($m=0.95$)	$m^*560 \text{ pF}$, $m=\{1, 0.99, 0.95\}$	579 pF \parallel 3.85 k Ω
Figure 23(a)-(c)	3.49 nF ($m=1$) 3.47 nF ($m=0.998$) 3.43 nF ($m=0.995$) 3.38 nF ($m=0.99$) 3.26 nF ($m=0.98$)	183 μH ($m=1$) 183 μH ($m=0.998$) 183 μH ($m=0.995$) 183 μH ($m=0.99$) 184 μH ($m=0.98$)	559 pF	$m^*579 \text{ pF} \parallel$ $m^*3.85 \text{ k}\Omega$, $m=\{1, 0.998, 0.995, 0.99, 0.98\}$

It should be noted that, when $A \approx B$, the first term in Eq. (4.2) approaches zero while D also goes to zero, thus resulting in the much simpler expression

$$v_{out} \approx \frac{Z_1}{Z_1 + Z_p} \cdot v_p. \quad (4.3)$$

Equation (4.3) shows that the output voltage is now approximately independent of the input voltage, and it is analogous to Eq. (4.1), which originates from [24]. The approximately equal symbol is used to emphasize that it is impossible to exactly match A and B in practice. Any small difference between the real or imaginary parts of A and B can have a significant impact on the output voltage, which depends upon the magnitude of C , as

illustrated in Figure 22. As it can be seen from this figure and Eq. (4.2), the presence of the matching components attenuates the output of the bridge circuit near the matching frequency, which is 500 kHz in the example case provided. Figure 22(a) shows how the sensed amplitude varies as $|A/B|$ gets further from its ideal value of 1. The orange curve demonstrates that the received voltage can be significantly attenuated, even with a value of $|A/B| \approx 0.99$. By comparing this result with the magenta and purple curves, it can be seen that $|Z_3| \approx |Z_p|$ is insufficient for optimal sensing, and it is necessary to have both the real and imaginary parts match, i.e. $C_3 \approx C_p$ and $R_3 \approx R_p$. Figure 22(b) displays the frequency dependence of the amplitude coefficient C , which is defined in Eq. (4.2). This coefficient can grow large near the resonance of the LC matching components, which will act to amplify the self-interference signal. All baseline parameter values used for the results shown in Figure 22 are those provided in Table 3.

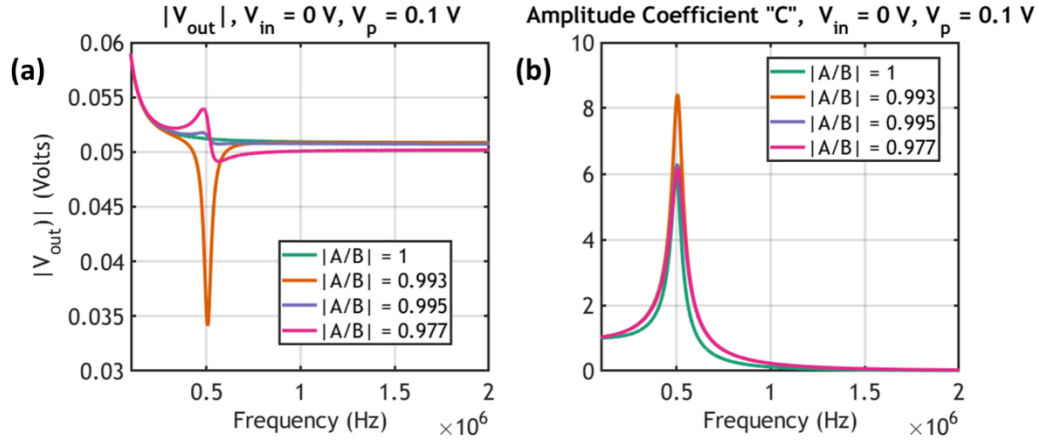


Figure 22. Effect of the impedance matching layer on the sensing amplitude. **(a)** The sensed amplitude varies as $|A/B|$ gets further from its ideal value of 1. Parameters for $|A/B| = 1$ are C_3/C_p and $R_3/R_p = 1$; for $|A/B| = 0.993$: $R_3 = \infty$ (open circuit) and $C_3/C_p = 1$, for $|A/B| = 0.995$: are C_3/C_p and $R_3/R_p = 0.99$, and for $|A/B| = 0.977$: C_3/C_p and $R_3/R_p = 0.95$. **(b)** Frequency dependence of the amplitude coefficient C , which is defined with Eq. (4.2).

In solving the expression $A \approx B$, there are three cases of particular interest: (1) the general solution $Z_1/Z_p \approx Z_2/Z_3$, and the specific cases (2) $Z_p \approx Z_3$ and $Z_2 \approx Z_1$, and (3) $Z_2 \gg Z_3$ and $Z_1 \gg Z_p$. Case 2 is notable because it was emphasized in earlier works on self-sensing actuators. It is worth pointing out that STAR (i.e., self-sensing) with a bridge circuit does not require an exact match of the complex impedance of the acoustic transducer, Z_p , with that of Z_3 , but rather that the ratio of the impedances of the left and right elements in the bridge circuit be approximately equal, as expressed in Case 1. Furthermore, in the case of the third solution for $A \approx B$, it is shown that

$$v_{\text{out}} \approx v_p, \quad (4.4)$$

yielding $Z_1/(Z_1 + Z_p) \rightarrow 1$ in Eq. (4.3), which is the optimal condition for sensing. However, in this case there is a performance tradeoff: since both the elements on the right-hand side of the bridge circuit have much larger impedances than those on the left, the voltage across the right-handed elements will be much larger than the voltage across the left-handed elements. This results in a smaller drive voltage for actuation of the transducer, and consequently a smaller value of v_p , if one assumes that v_p results from the signal generated by the transducer in the bridge circuit and it is not sensing any other externally-generated acoustic signal. Thus a tradeoff exists between having a larger value for the coefficient of v_p in Eq. (4.3) and having a larger value of v_p itself, which ultimately depends upon the acoustic environment as well as specific parameters of the transducer.

In terms of STAR terminology, the signal-to-interference ratio (SIR) is defined as

$$\text{SIR} \equiv 20 \log_{10} \left| \frac{(B+D) \cdot v_p}{C(A-B) \cdot v_{\text{in}}} \right| = 20 \log_{10} \left| \frac{B+D}{C \cdot (A-B)} \right| + \text{DIR}, \quad (4.5)$$

where the denominator and numerator of the left expression are the first and second terms from Eq. (4.2), respectively. This ratio represents the portion of the output voltage resulting from the sensing signal divided by the portion of output resulting from the input signal. The latter term is also referred to as the residual signal, which is the remaining portion of the self-interfering signal after cancellation has been performed. The detection-to-input level ratio (DIR), which is included in the right-most expression of Eq. (4.5), is defined as

$$\text{DIR} \equiv 20 \log_{10} \left| \frac{v_p}{v_{\text{in}}} \right|. \quad (4.6)$$

Defining the DIR as a separate term in Eq. (4.5) is useful as it makes the first term dependent only upon the impedances of the circuit elements, while the second term only depends on the amplitudes of the incident and received signals. Furthermore, self-interference cancellation (SIC) is then defined as

$$\text{SIC} \equiv 20 \log_{10} \left| \frac{v_1}{C(A-B) \cdot v_{\text{in}}} \right|, \quad (4.7)$$

where v_1 represents the self-interfering signal given that the cancellation process is applied to the signals at the nodes of v_1 and v_2 in the bridge circuit (which both have similar amplitudes) and v_1 is the voltage on the transducer side of the bridge.

4.3 EVALUATION OF SIC AND SIR

The relationship between SIC, SIR, and the circuit parameters from Eqns. (4.5)-(4.7) was evaluated and plotted for a transducer response that is independent of frequency in Figure 23(a)-(c). Here the thresholds established for achieving various levels of SIR are shown, given the closeness of the match of the parameters that determine A and B . Figure 23(a)-(b) show values of the SIC and SIR spectra as C_3 and R_3 are varied from their optimal values, where it is assumed that the piezoelectric voltage source $v_p = v_{\text{in}} / 10$, and that the acoustic transducer can be idealized as a parallel RC circuit with values of $C_p = 579 \text{ pF}$ and $R_3 = 3.85 \text{ k}\Omega$. The results display the case with perfect impedance matching, corresponding to the top curve in (a) and (b), as well as cases where both the

capacitance and resistance are mismatched by 0.2%, 0.5%, 1%, and 2%. Figure 23(c) presents the first and second terms in Eq. (4.2), which are used to compute the results for SIR and SIC in Figure 23(a)-(b). The flat curve at the top of Figure 23(c) represents v_p while the lower curves represent the amplitude of the residual signal for the various values of impedance mismatch. The lowest curve in Figure 23(c) represents the case where C_p and R_3 perfectly match the transducer impedance, which corresponds to the highest values of SIC and SIR shown in Figure 23(a)-(b).

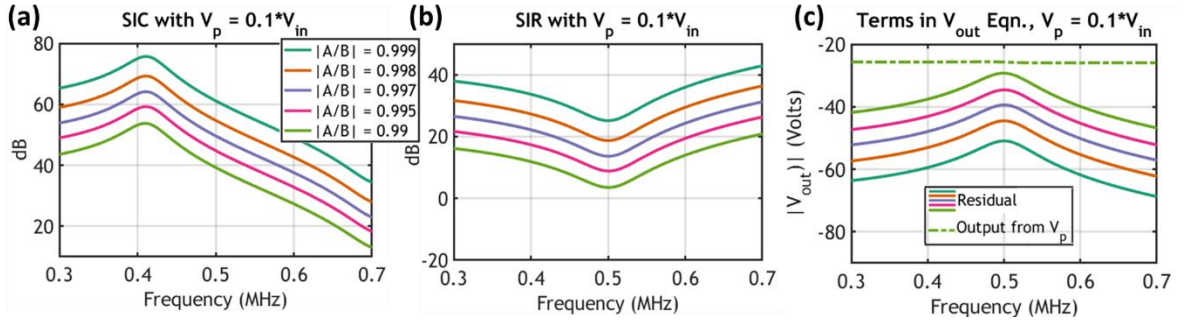


Figure 23 (a)-(b) Values of the SIC and SIR spectra as A and B are varied from their optimal values, where it is assumed that the piezoelectric voltage source $v_p = v_{in} / 10$, and the circuit parameters are specified in Table 3. (c) The first and second terms in Eq. (4.2) which are used to compute the results for SIR and SIC in (a)-(b). Parameters for $|A/B| = 0.999$ are C_3 / C_p and $R_3 / R_p = 1$; for $|A/B| = 0.998$: C_3 / C_p and $R_3 / R_p = 0.998$; for $|A/B| = 0.997$: C_3 / C_p and $R_3 / R_p = 0.995$; for $|A/B| = 0.995$: C_3 / C_p and $R_3 / R_p = 0.99$; and for $|A/B| = 0.99$: C_3 / C_p and $R_3 / R_p = 0.98$.

4.4 CHAPTER SUMMARY

In this chapter we have shown theoretically that a fully passive LC-matched bridge circuit model can be used to achieve broadband SIC in acoustic measurement systems. We have also shown that, with the proper choice of circuit parameters, large positive values of SIR can be achieved. However, the analysis shows that small imbalances of the impedance values within the bridge circuit can lead to significant degradation of the SIR and SIC. As shown in Figure 23(a)-(c), a one percent mismatch in the parameters A and B (which represents a 2-percent mismatch in both capacitance and resistance for a parallel RC model) can result in a performance degradation of approximately 40 dB for both the SIC and SIR. Therefore, when building such a circuit it is critical to ensure not only tight matching of the nominal impedance values of each component, but also to consider any imbalances that could be a result of parasitic resistance, capacitance, or inductance in the breadboard and cables, as well as any impedance variation that could be due to environmental parameters such as temperature and/or humidity.

Chapter V: Experimental Results and Applications of Acoustic STAR

5.1 MEASUREMENT APPROACH AND SETUP

In this chapter, an experimental study of acoustic STAR is presented to demonstrate a practical implementation of an acoustic STAR system and elucidate realistic values for parameters that are critical to success of the SIC. When considering a lab setup, one important consideration is to evaluate assumptions with regard to prediction of the sensing voltage, v_p ; As described in Chapter IV, for some problems it may be sufficient to consider v_p as a flat broadband excitation proportional to v_{in} . However, in general there will be frequency dependence that can greatly vary as a function of the particular signal source, cables, connectors, circuit components, and transducer chosen for the measurement. All of these effects can be accounted for by measuring a single system response function. When the system response in a standard reference configuration, including the influence of electroacoustic loading, is known, then the system function can be determined as the ratio

$$s(\omega) = \frac{v_{out,ref}(\omega)}{t_{A,ref}(\omega)}, \quad (5.1)$$

where $s(\omega)$ is the system function that is independent of the acoustic environment, $v_{out,ref}(\omega)$ is v_{out} from Eq. (4.2) without self-interference present, and $t_{A,ref}(\omega)$ is the acoustic transfer function corresponding to the given reference configuration [142]. The

received voltage signal with the given system can therefore be predicted in an arbitrary acoustic environment by writing

$$v_{\text{out,m}}(\omega) = s(\omega)t_A(\omega), \quad (5.2)$$

where $v_{\text{out,m}}(\omega)$ is v_{out} received by the bridge circuit in the new configuration, *where the incident and received signals are completely separated in time*, and $t_A(\omega)$ is the acoustic transfer function corresponding to the new acoustic environment.

5.2 PREDICTING SIC AND SIR WITH THE SYSTEMFUNCTION

Figure 24(a)-(b) show the results for the SIC and SIR, respectively, when considering the system function of the transducer and measurement configuration detailed in the following paragraphs. These results indicate that the potential bandwidth for SIC is limited by the combined response of the transducer, the matching components, and the parasitics in the measurement. It can also be seen that SIR greater than 10 dB can be achieved with the given test setup, as long as the capacitance and resistance are both within 0.5% of the corresponding RC values from the transducer model. Finally, Figure 24(c) shows empirically determined value of v_p along with the residual signals that correspond to a mismatch of R and C by 0.2%, 0.5%, 1%, and 2% from the ideal values in the transducer model. These ratio of these two curves are used to compute the SIR which varies from near infinity with an ideal match of R and C , to as low as -2 dB when the mismatch for both components increases to 2%.

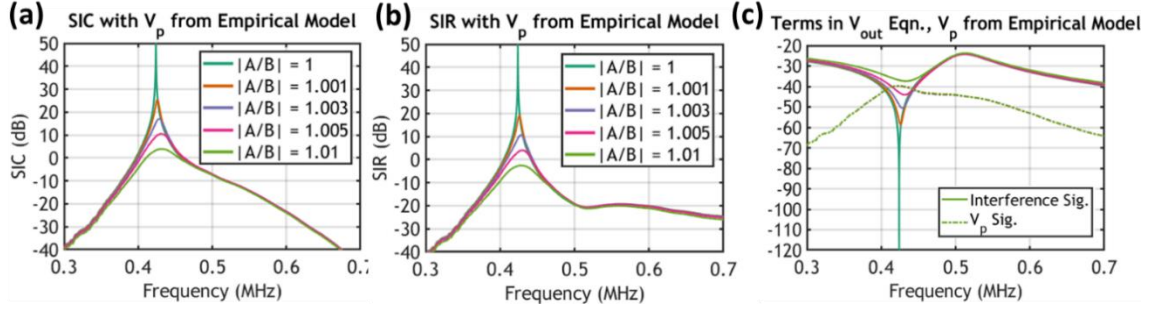


Figure 24. (a)-(b) Values of the SIC and SIR spectra as A and B are varied from their optimal values, where the transducer impedance, Z_p is now represented by measured impedance values, and v_p is based on empirical results according to Eqn. (5.2). **(c)** The first and second terms in Eq. (4.2) which are used to compute the results for SIR and SIC in (a)-(b). Parameters for $|A/B| = 1$ are C_3/C_p and $R_3/R_p = 1$; for $|A/B| = 1.001$: C_3/C_p and $R_3/R_p = 0.998$; for $|A/B| = 1.003$: C_3/C_p and $R_3/R_p = 0.995$; for $|A/B| = 1.005$: C_3/C_p and $R_3/R_p = 0.99$; and for $|A/B| = 1.01$: C_3/C_p and $R_3/R_p = 0.98$. The circuit parameters are specified in Table 3.

The experimental setup depicted in Figure 25(a) represents a standard reference configuration of interest for common ultrasonic nondestructive evaluation (NDE) measurements and used here to demonstrate a practical implementation of STAR for acoustical applications. A Panametrics V318 immersion transducer is positioned near a water-air interface, which is employed as a reference reflector with the water-air interface acting as a nearly ideal pressure-release acoustic boundary. This means that the acoustic pressure approaches zero at the interface, resulting in near-perfect reflection (at normal incidence the acoustic power transmitted to the air is 60 dB down from the incident intensity) [2]. A short-duration signal is transmitted such that the signal ends before any

reflection occurs, which permits easy separation of the incident and reflected signals in the time domain. Figure 25(b) depicts the same physical setup as Figure 25(a), but where a longer duration signal is transmitted, such that the incident signal is still transmitting when the signal reflected from the interface reaches the transducer. In this case, the STAR system can be used to separate the incident and reflected signals in the measurement.

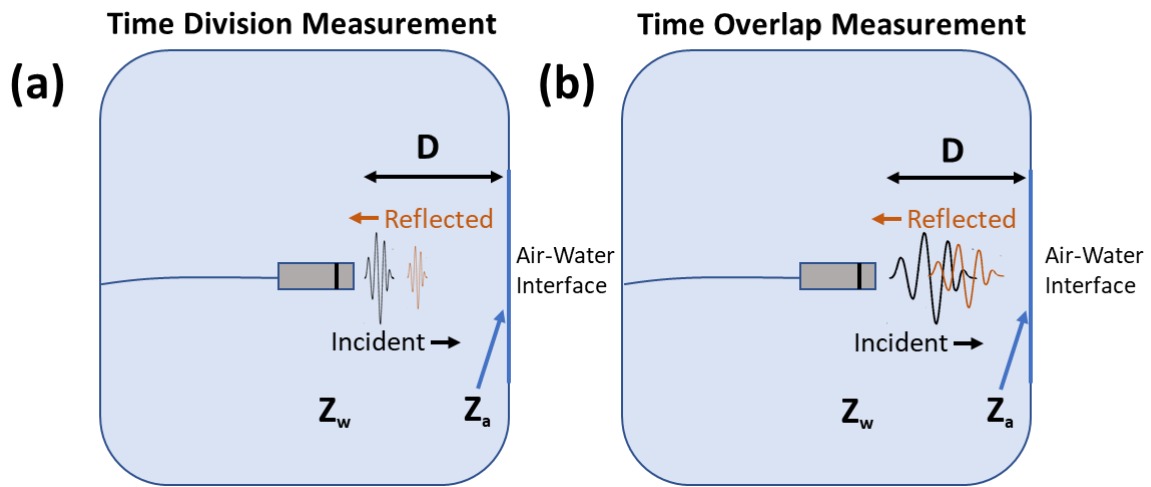


Figure 25. Reference measurement configuration for STAR measurements with an immersion transducer. **(a)** A short-duration signal is transmitted such that the signal ends before any reflection occurs, which permits easy separation of the incident and reflected signals in the time domain. **(b)** A signal with longer duration and same center frequency is transmitted such that the incident signal is still transmitting when the signal reflected from the interface reaches the transducer. In this case, the STAR system can be used to separate the incident and reflected signals in the measurement.

The V318 transducer was selected because its nominal resonance frequency, 500 kHz, is low enough to avoid significant effects from cable length and/or positioning, while the acoustic attenuation in water is negligible at this frequency over short distances.

Furthermore, the response of the V318 is well-damped, such that it can be operated effectively over a broad frequency range. These characteristics can be observed in the electrical impedance data shown in Figure 26(a)-(d). That figure shows measurements of the complex impedance of the V318 compared to a parallel RC circuit model and a higher-order RLC model of a piezoelectric transducer from Sherman and Butler [143], which is reproduced in Figure 27 for convenience and will be referred to as the S&B model from this point forward. Figure 26(a) displays the magnitude of the transducer impedance, where the measured impedance is compared with both the parallel RC model and the S&B model. While both models match the magnitude data fairly well above 450 kHz, the main differences are caused by the higher-order terms in the frequency dependence of the real part of the transducer impedance, shown in Figure 26(b). Figure 26(c) and (d) plot the phase and imaginary parts of the transducer's impedance, respectively, including measured values and results from both transducer models. The accuracy of modeling both real and imaginary parts can have a significant impact on the balancing of the complex parameters A and B , which ultimately determine the efficacy of the SIC process.

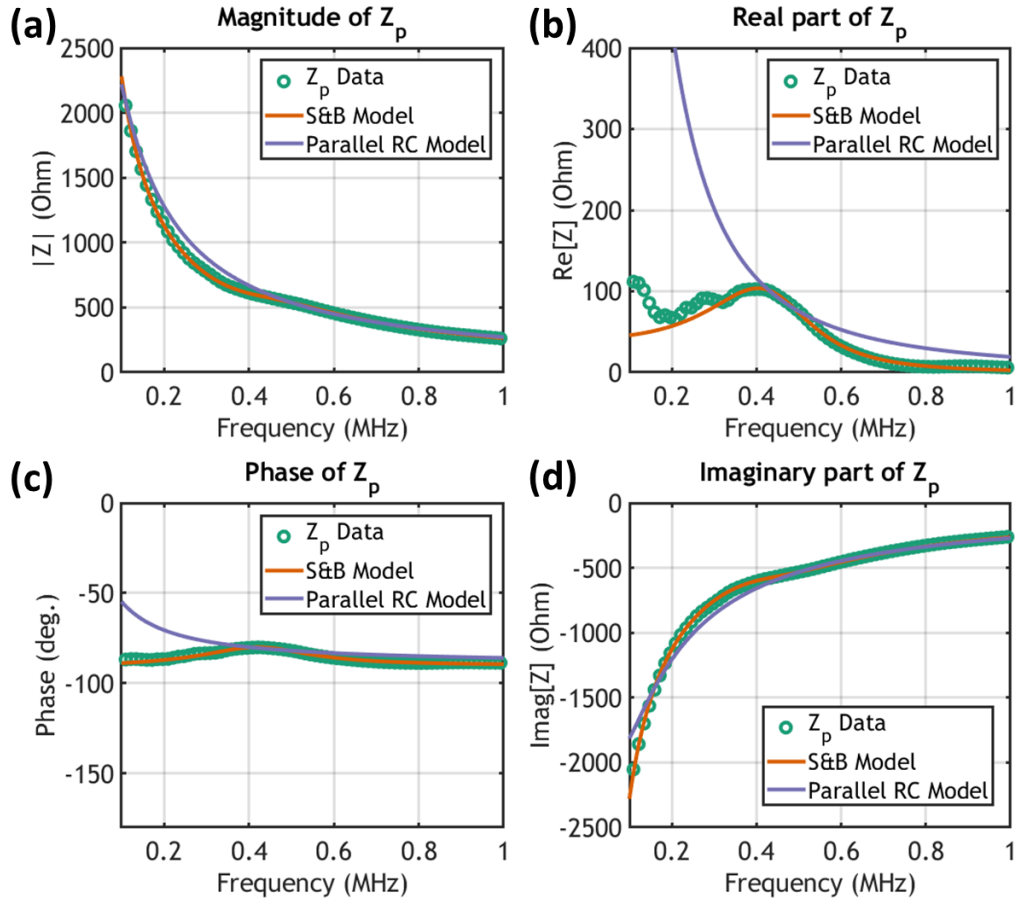


Figure 26. Measurements of the complex impedance of the V318 immersion transducer compared to a parallel RC circuit model and a higher-order RLC model of a piezoelectric transducer suggested by Sherman and Butler (S&B model) [143] and reproduced in Figure 27. The S&B model consists of a series RLC circuit in parallel with a capacitance and a conductance. (a) Magnitude of the transducer impedance. (b) Real part of the transducer impedance. (c) Phase of the transducer's impedance. (d) Imaginary part of the transducer's impedance.

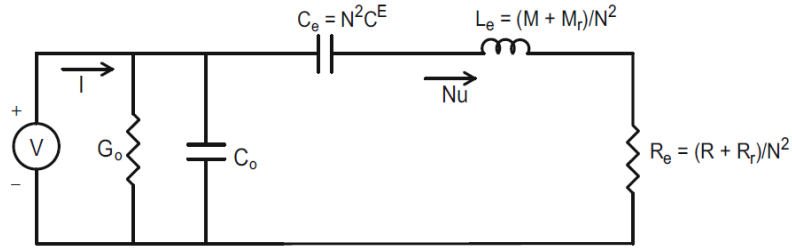


Figure 27. RLC model of a 1-dimensional piezoelectric transducer, reproduced from Figure 3.16 of [143].

5.3 EVALUATING THE TRANSDUCER AND ACOUSTIC RESPONSE

The acoustic transfer functions from Eq. (5.1)-(5.2) are represented by the ratio of the average blocked force (force when the transducer is constrained to have zero velocity) on the surface of the transducer during reception to the average force over the face of the transducer during transmission. It was verified that the V318 transducer can be accurately modeled as a piston source [142] from measurements of the surface velocity made using a Polytec PSV-500-M Scanning Laser Doppler Vibrometer (SLDV) system. Figure 28(a) shows the measured surface velocity of the V318 transducer at 500 kHz and Figure 28(b) provides a cross section of the pressure field that was computed using a numerical implementation of the angular spectrum method, also known as Fourier Acoustics (FA), to estimate the complex field radiated by a source with known surface velocity. In this case, the SLDV data is used as the boundary condition for the FA code. The results from the data-based propagation model are assessed in Figure 28(c). Here the on-axis acoustic pressure along the line $(x, y, z) = (0, 0, z)$, predicted using the FA model, is compared with

measured hydrophone data and the analytical result for radiation from a hard piston with uniform velocity in a rigid baffle. It can be seen that the piston assumption captures the pressure amplitude within approximately 2 dB in the far field. Therefore, the analytical solution for radiation from a piston can be substituted for the FA model solution with a small impact on the accuracy of the predictions. This approximation is most accurate when the acoustic reflection takes place in the far field of the transducer ($z > 4$ cm), because in that case it is known that radiated pressure varies smoothly as a function of distance, and it will not exhibit rapid fluctuations as shown in Figure 28(c) for $z < 4$ cm. The distance $z = 4$ cm was determined to be the near field distance of the V318.

In order to make time-overlap STAR measurements in the far field with the V318, it was necessary to use an arbitrary waveform generator, rather than pulser-receiver hardware that is often paired with for NDE measurements [142]. This is due to the fact that a pulser-receiver is only capable of transmitting short duration pulses on the order of $10\ \mu\text{s}$, whereas the far field distance of 4 cm requires significantly longer signal durations for transmit/receive overlap to occur. A standard laboratory function generator (Agilent 33210A) was used as the signal source, allowing us to set the value of R_0 to $50\ \Omega$. The matching impedances, Z_{M1} and Z_{M2} , were determined based upon the effective complex impedance of the bridge circuit, which acts as the load.

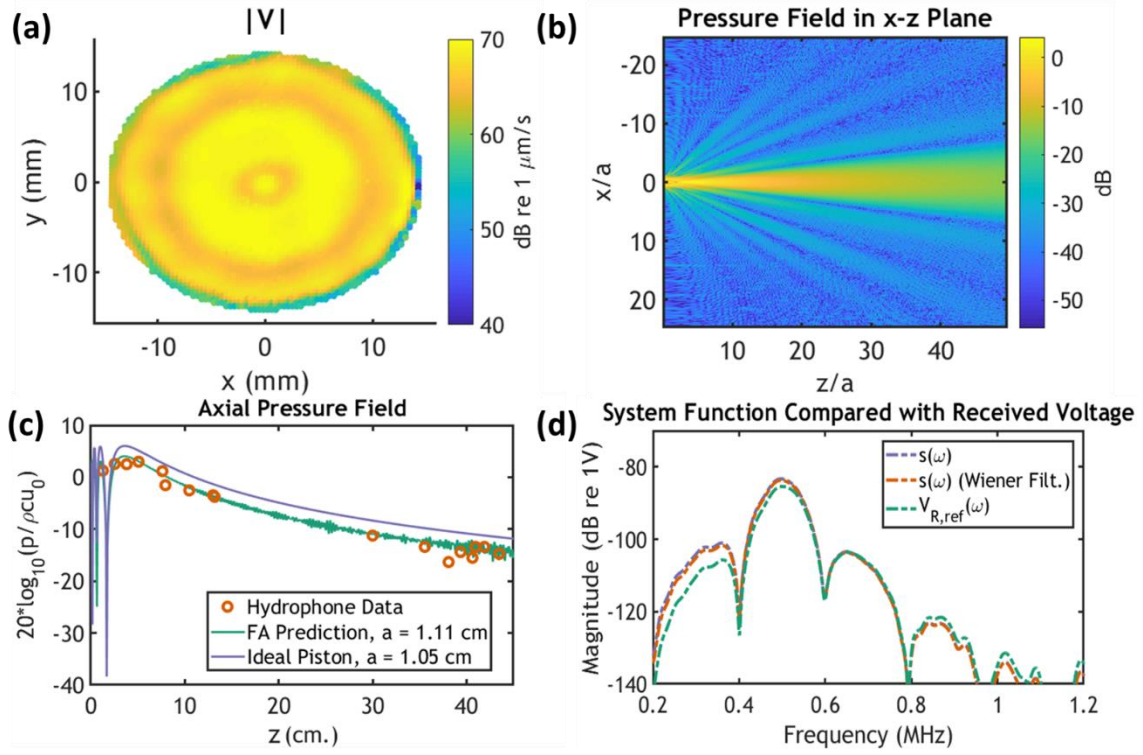


Figure 28. (a) SLDV measurement of an air-loaded V318 transducer with 500 kHz sinusoidal excitation. (b) Pressure field in the x - z plane through on the transducer axis computed using SLDV transducer velocity data and a Fourier Acoustics solver at 500 kHz. (c) On-axis acoustic pressure along the z -axis at 500 kHz. Data is overlaid with the Fourier Acoustics (FA) prediction and the analytical result for piston with uniform velocity in rigid baffle. The data and FA prediction are in good agreement, within approximately 2 dB for all axial positions measured. (d) System function computed from measurement at $z = 10$ cm, which assumes that the V318 can be modeled as an ideal piston. The Wiener filter was computed with $\varepsilon = 0.1$ as defined in [142].

5.4 ASSESSING THE EFFECT OF COMPONENT PARASITICS

When constructing an impedance-matched bridge circuit in the lab, the parasitic resistances and capacitances of components and measurement cables can potentially have a major impact on the output of the circuit. The values of these parasitics are difficult to predict *a-priori*, and so the best way to assess their impact is to measure the parasitics in the lab and then feed that data back into the model equations. Figure 29 shows the power delivery from the signal source to the acoustic transducer (through resistor R_p). The results confirm that the parasitic resistances of the lab components have a significant impact on the power delivery to the transducer. When the parasitics are measured and included in the system model, the model predicts a 57% decrease in the amount of power delivered to the transducer (red curve), in comparison with the model having ideal assumptions of zero series resistances for all LC components (purple curve). It is also seen that balancing all four elements on the bridge with equal resistances results in a reduction of the power delivered into the transducer (green curve).

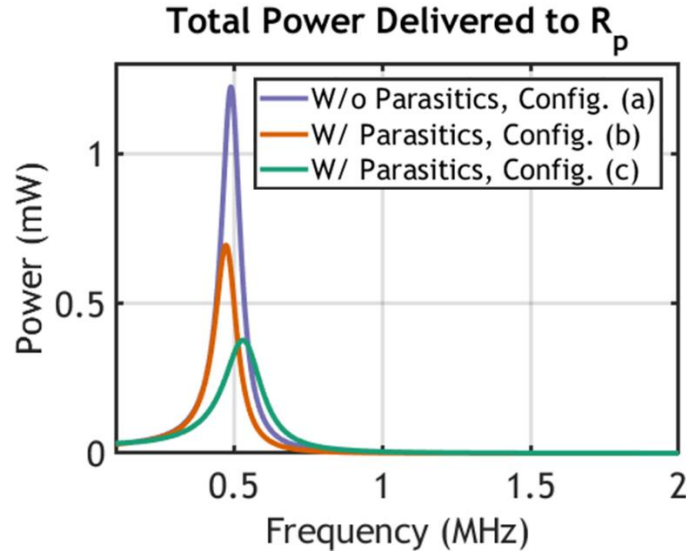


Figure 29. Multi-sim circuit models of the bridge circuit with measured values for the components, under configurations that consider the parasitic resistance, and various forms of balancing the real part of the impedances in the bridge. These changes impact the power delivered to the transducer through resistor R_p . The effect of parasitic resistance on power delivery can be seen by comparing the purple and red curves. It is also seen that balancing all four elements on the bridge with equal resistances results in a reduction of the delivered power to the transducer (green curve), and it was subsequently determined that this did not lead to any improvement in operating bandwidth. Parameter values for each of these configurations are reported in Table 4.

Table 4. Component values used to compute the output of the LC-matched bridge circuits as presented in the corresponding figures listed on the leftmost column. The first two rows use the topology of Figure 20(a) and the last row uses that of Figure 20(b).

Fig.	V_{in}	R_0	Z_{M1}	Z_{M2}	V_p	Z_p	Z_1	Z_2	Z_3
Figure 29(a)	1.0 V_{pk}	50 Ω	3.3 nF	185 μH	0 V_{pk}	579 pF 3.85 k Ω	559 pF	560 pF	565 pF 3.85 k Ω
Figure 29(b)	1.0 V_{pk}	50 Ω	3.3 nF + 0.10 Ω	184 μH + 28.2 Ω	0 V_{pk}	579 pF 3.85 k Ω	559 pF + 0.11 Ω	560 pF + 0.11 Ω	565 pF 3.85 k Ω
Figure 29(c)	1.0 V_{pk}	50 Ω	184 μH + 23.3 Ω	124 pF + 1.27 Ω	0 V_{pk}	579 pF 3.85 k Ω	559 pF 3.85 k Ω	560 pF 3.85 k Ω	565 pF 3.85 k Ω

Measurements were made using a physical embodiment of the setup shown in Figure 25, which is pictured in Figure 30. A circuit with parameters defined in the second row of Table 4 was interfaced with a Panametrics V318 immersion transducer; the signal source used was an Agilent 33210A Arbitrary Waveform Generator and signals were measured with a Keysight DSOX2004A oscilloscope in high-resolution mode (12-bit). To first characterize the system response, the acoustic-independent system function was measured as described by Eq. (5.1), using a frequency sweep of sinusoidal bursts, each with a duration of 40 cycles, and periodic square pulse input. The measured system response function is shown in Figure 28 (d).

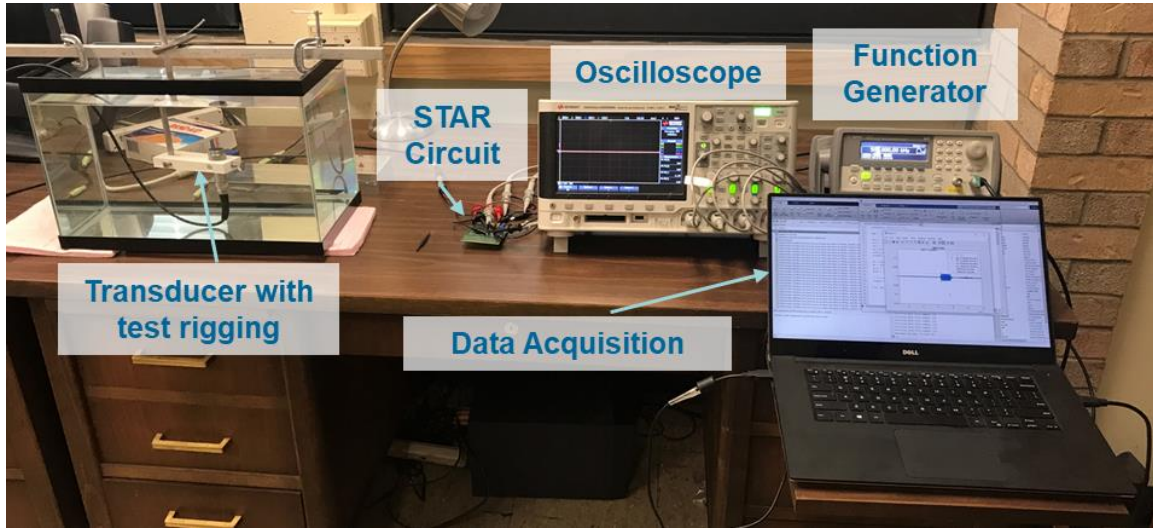


Figure 30. Photograph of experimental setup.

5.5 PREDICTING THE SIR AND MEASURING THE SINR

In this Section we show that analytical modeling and system function can be combined to predict SIC and SIR of the impedance-matched bridge circuit, which has a center frequency that can be selected by proper choice of RLC values in the bridge. Modeled and measured results are provided in Figure 31, which shows the results of tuning the peak SIR frequency. Figure 31(a) depicts ideal SIR in the absence of any external noise in the system, where Z_3 is modeled as a parallel RC circuit. The curves in that subfigure correspond to the values of C_2 , R_3 , and C_3 reported in Table 5. These choices of parameters result in $A(f_0) = B(f_0)$ in Eq. (4.2), where f_0 is the peak SIR frequency. In comparison, Figure 31(b) shows practical limitations when a small amount of white noise (-54 dB re 1V) is

added to the interference signal, which allows us to compute the signal-to-interference-plus-noise ratio (SINR). The noise level used was selected as a reasonable match to the noise in the experimental setup used in this work. The SINR demonstrates that the influence of even low levels of noise within the interfering signal will significantly limit detection levels of the received signal. Further, it is noted that the choice of SIR peak frequency has an impact on the positive SIR bandwidth, which varies from 9 kHz to 25 kHz in the predictions for SIR and from 9 kHz to 22 kHz for SINR. Figure 31(c) shows the estimated residual voltage and received voltage at the output of the bridge circuit, which are used to compute the SIR shown in Figure 31(b). Finally, experimental measurements of SIR, including frequency tuning, are presented in Figure 31(d). These measurements are in good agreement with the predictions plotted and shown in Figure 31(b). The circuit parameters used are listed in Table 5 and correspond to the “x” markers on Figure 35 (a)-(b). The maximum 6-dB SINR bandwidth measured was 16 kHz with center frequency of 510 kHz for a 3% fractional bandwidth (which is about triple the fractional bandwidth of an 802.11n Wi-Fi system).

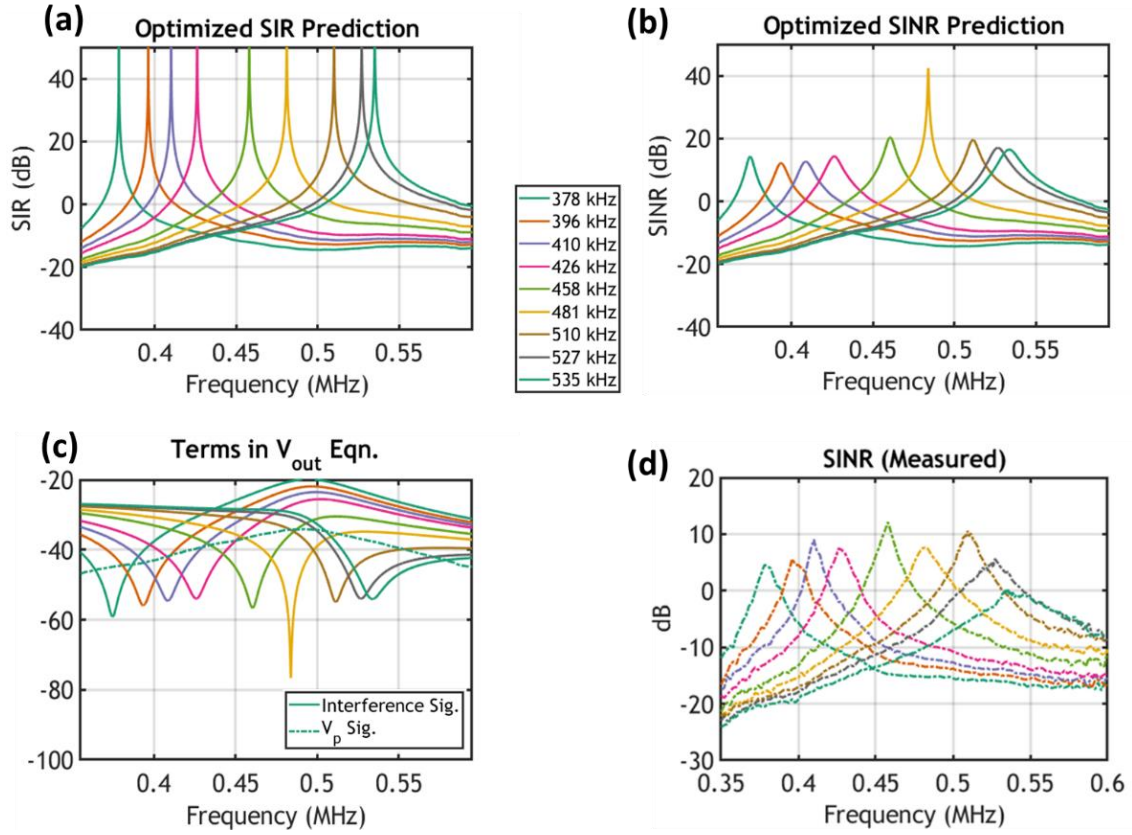


Figure 31. Tuning the peak SIR frequency of the STAR system. **(a)** Predicted SIR with Z_3 modeled as a parallel RC circuit **(b)** Predicted signal-to-interference plus noise ratio (SINR), where -54 dB re 1V of white noise is added to the interference signal (matching noise level in the lab measurements). **(c)** Predicted interference spectra (solid lines) and received voltage spectra (dot-dashed lines), for the SINR predictions of plot (b). **(d)** Measurements of SINR at frequencies corresponding to predictions in (b). Parameters used for these measurements are reported in Table 5.

Table 5. Experimental parameters used for measurements shown in Figure 31(d). All measurements used the layout of Figure 20(a) with $v_{in} = 1.2V_{pk-pk}$, $R_0 = 53\Omega$, $Z_{M1} = 3.3nF + 0.1\Omega$, $Z_{M2} = 184\mu H + 28.2\Omega$, $Z_1 = 560pF + 0.1\Omega$, $Z_2 = 1/j\omega C_2$, $Z_3 = (1/j\omega C_3) \parallel R_3$, and Z_p representing the V318 transducer with impedance values described in Figure 34. Parasitic resistances for all capacitors were measured as less than 0.2Ω .

Peak Freq. (kHz)	378	396	410	426	458	481	510	527	535
C₂ (pF)	559	559	559	559	615	615	615	615	615
C₃ (pF)	583	576	572	563	598	594	585	580	575
R₃ (Ohm)	5512	5156	4878	4679	4445	4382	4770	5003	5347

Figure 32(a) displays the residual input signal amplitude predicted by Eq. (4.2) for two different sets of impedance values: the purple curve uses nominal RLC component values and values of the measured impedance of the transducer, Z_p . The green curve uses the same impedance measurement for Z_p but also uses measured values of complex impedance for all other RLC components. Figure 32(b)-(c) are used to compare the residual input amplitude with complex values of parameters A and B for the as-built STAR system. These plots show that the high-Q nature of the SIR peaks can be explained by crossing of the real part of A and B (green and orange lines) in Figure 32(b) at a single point, which also occurs similarly in the solutions shown in Figure 23(d)-(f) and Figure 31(a)-(d). This point is denoted by the vertical dashed line connecting Figure 32(a)-(c).

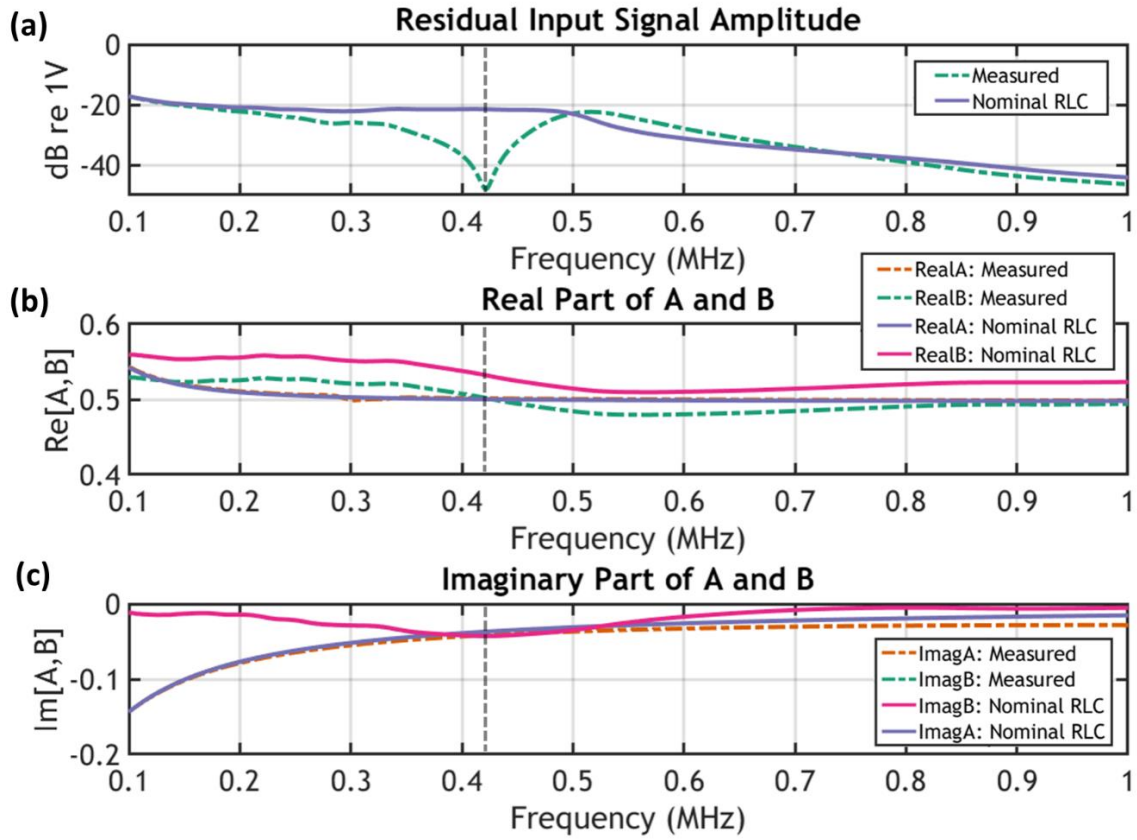


Figure 32. (a) Amplitude of the residual input signal as predicted by Eq. (4.2). The solid purple curve uses nominal RLC component values and values of the measured impedance of the transducer, Z_p . The green curve uses measured values of complex impedance for all components. (b)-(c) The real and imaginary parts of the parameters A and B from Eq. (4.2). The vertical dashed line of each subfigure denotes the frequency of maximum SIC, which occurs where both the real and imaginary parts of A and B are nearly equal.

5.5 PARASITIC MODELING WITH A LEAST-MEAN-SQUARES FIT

In this section, we show that experimental parasitics have a major impact on the output of the STAR system, but that these can nevertheless be accounted for in the modeling to achieve significantly more accurate predictions of SIC. The parasitic values of principal concern result from the circuit board interconnects, the wires, and the measurement probe cables used with the Keysight DSOX2004A oscilloscope. The impact of the measurement parasitics is captured in the results presented in Figure 33(a)-(i), which plot the measured residual input signal amplitude for each peak frequency listed in Table 5 and predictions from Eqn. (4.2). It can be seen from the figure that the analytical solutions have significant disagreement with experimental observations, despite the complex impedance spectrum of each component in the model being accurately determined by the Keysight E4990A impedance analyzer before being placed into the circuit. The differences in predicted and measured values are due to the fundamental sensitivity of the bridge circuit to small changes of resistance and reactance, which are caused by the measurement cables, wires, connectors, and solder on the board. To compensate for these parasitics, Z_p was recast as an effective impedance, such that any series or parallel parasitics from the board would be included within Z_p . This approach is consistent with the assumption that front-end and amplifier electronics in a transducer can be considered part of the transducer itself [143]. A least-squares algorithm was implemented with all of the experimental observations from Table 5 to provide a global fit for a single effective value of Z_p , which is compared with

measured values and shown in Figure 34(a)-(b). It can be seen that, while the changes to Z_p due to the least-squares fit were relatively small, this new parameter value resulted in significant improvements for the prediction of SIR as a function of frequency, as can be seen in Figure 33(a)-(i). The real part of the effective Z_p presented in Figure 34(a) differed by -1.8Ω on average (-2.5% from measured), with a maximum difference of 8.5Ω (-9.5% from measured), and a standard deviation of 2.5Ω , over a frequency range of 350 kHz to 600 kHz. The imaginary part of the effective Z_p presented in Figure 34(b) has a mean difference of -45.6Ω (-8.3% from measured), with a maximum difference of -61.0Ω (9.1% from measured), and a standard deviation of 8.0Ω , over the same frequency range.

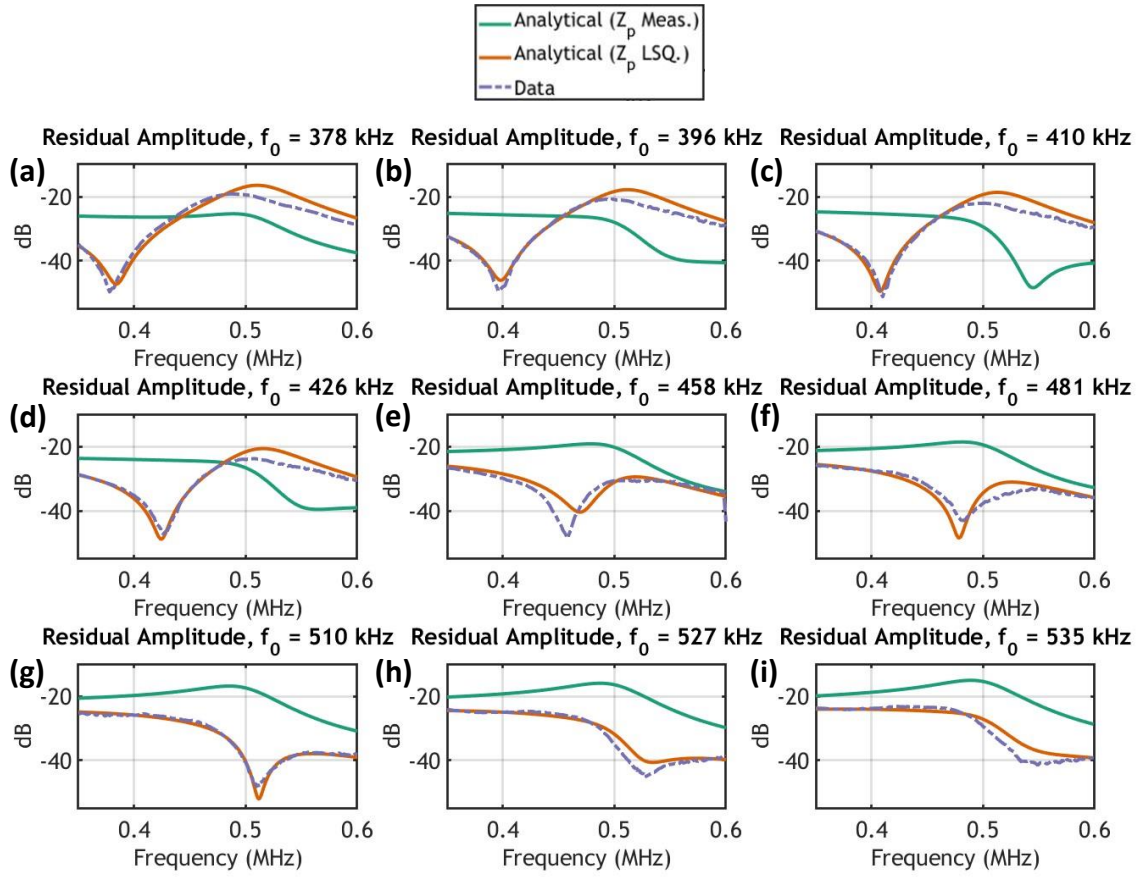


Figure 33. Measured residual voltage amplitude and predictions from Eqn. (4.2) with values of Z_p as described in Figure 34. Predictions and measurements in plots (a)-(i) have parameters that are listed for the corresponding peak frequencies in Table 5. It can be seen that the predictions for residual amplitude are significantly more accurate when Z_p values are determined by the best-fit choice of parameters.

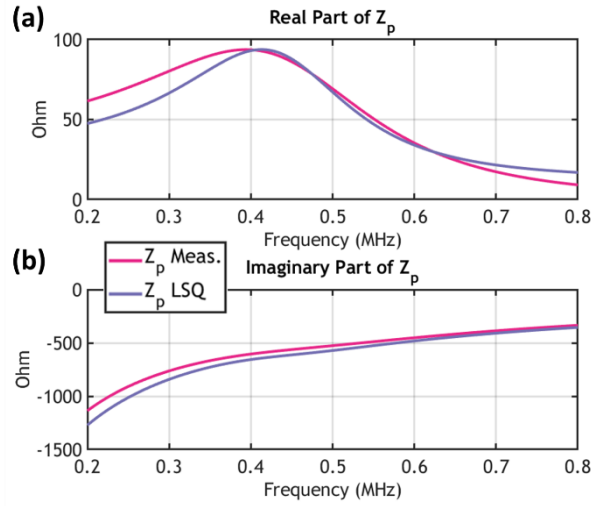


Figure 34. (a)-(b) Real and imaginary parts of the measured transducer impedance, Z_p , in comparison with an effective impedance including parasitics in the bridge.

Figure 35(a)-(b) show values of the real and imaginary parts of Z_3/Z_2 computed for peak SIR at each center frequency (simulated and measured). Each “×” is a measured value that also corresponds to the measurements presented in Figure 31(d). The magenta curves represent predictions from Eqn. (4.2) with all impedances represented by measured data from the E4990A impedance analyzer, which is shown in Figure 34(a)-(b). The purple curves in Figure 35(a)-(b) represent predictions from the same equation, but with the new effective value of Z_p from the least-mean-squares fit, which is also presented in Figure 34(a)-(b). Significant improvements of the SIR predictions with the use of the effective transducer impedance can also be seen in Figure 35(a)-(b), where greatest difference is observed in Figure 35(a) with an average difference between model and measurement

decreasing from -10.1% to -1.5% for the predictions with the measured Z_p and effective Z_p , respectively.

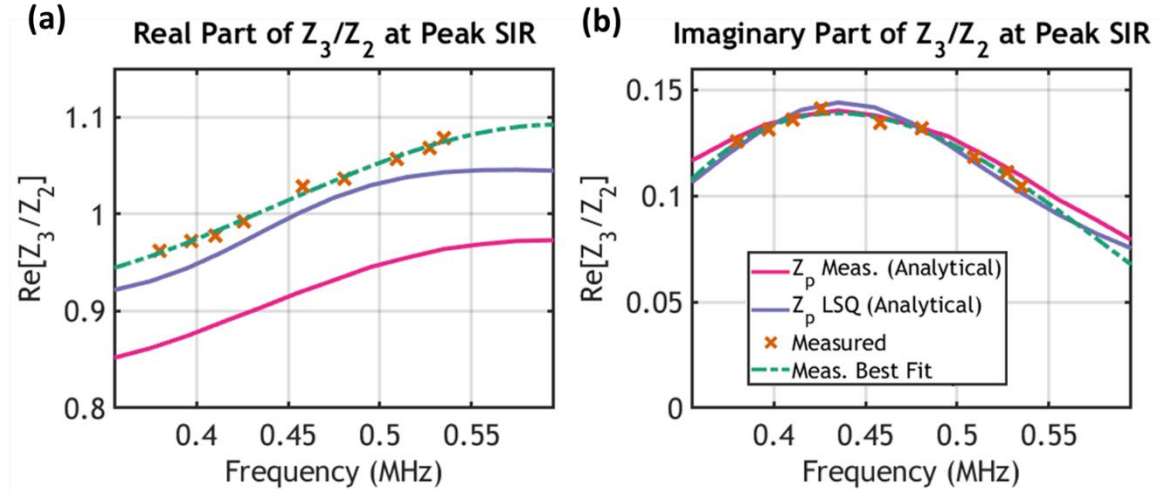


Figure 35. (a)-(b) Values of the real and imaginary parts of Z_3/Z_2 that result in peak SIR at each center frequency (simulated and measured), with each measurement corresponding to parameter values reported in Table 5.

5.6 BROADBAND SIC AND SIR WITH THE LEAST-MEAN-SQUARES FIT SOLUTION

Broadband performance of the STAR circuit can be extended by utilizing a slightly more complex compensation circuit represented by the S&B model of Figure 27 in the place of the previously used parallel RC model for Z_3 . This updated model for Z_3 leads to a predicted increase in the maximum 6-dB SIR bandwidth by more than an order of magnitude, from a maximum of 28 kHz (6% fractional bandwidth) when using a parallel RC model of the transducer to a new maximum of 298 kHz (60% fractional bandwidth), as seen in Figure 36(a). However, the predicted SIR bandwidth rapidly decreases with small increases of parameter mismatch, as described below.

Figure 36(a) shows the SIR with Z_3 and Z_p represented by the least-squares fit to the S&B model, as presented in Figure 34(a)-(b). Results are shown for a parameter sweep for all RLC elements comprising Z_3 , which is represented as an effective impedance for the S&B model of Figure 27, with $G_0 \rightarrow \infty$, such that

$$Z_3 = \left(\frac{1}{C_0} \right) \left(\frac{1}{j\omega C_e} + j\omega L_e + R_e \right) / \left(\frac{1}{C_e} + \frac{1}{C_0} - \omega^2 L_e + j\omega R_e \right).$$

The parameter sweep considers a mismatch of $X_n / X_{n,0}$ by 0.2%, 0.5%, 1%, and 2%, where $n = \{1, 2, 3, 4\}$; $X_1 = C_e$; $X_2 = L_e$; $X_3 = R_e$; and $X_4 = C_0$ as defined in the S&B model diagram. The top and bottom dashed curves represent maximum and minimum bounds on the SINR predicted by a Monte Carlo model that varied these four parameters, in addition to C_2 , by +/- 2%. All predictions assume that the noise level is -54 dB re v_{in} ,

which matches the noise level in the measured data. The 6-dB bandwidths for the top three curves in Figure 36(a) (0%, 0.2% and 0.5% mismatch) are 298 kHz (60% fractional bandwidth), 210 kHz (42% fractional bandwidth), and 96 kHz (19% fractional bandwidth) respectively, while the last two curves do not have a 6-dB bandwidth as they never exceed an amplitude of 6-dB. Figure 36(b) presents the SIR predicted with Z_3 represented by the S&B transducer model and Z_p represented by its measured impedance data with the same parameter sweep for the RLC components within Z_3 as described above for Figure 36(a). The 6-dB bandwidths of the top four curves (0%, 0.2%, 0.5%, and 1% mismatch) are 143 kHz (29% fractional bandwidth), 130 kHz (26% fractional bandwidth), 84 kHz (17% fractional bandwidth), and 69 kHz (14% fractional bandwidth), respectively. The last curve in Figure 36(b) (2% mismatch) does not have a 6-dB bandwidth as it never exceeds an amplitude of 6-dB.

Furthermore, a circuit containing RLC components was constructed for testing, with values close to those used for theoretical predictions, as presented in Table 6. The measurement result is plotted in Figure 36(a)-(b), where the data for SINR amplitude is repeated in both plots for ease of comparison with all predictions. We can see that the results in Figure 36(b) generally have a sharper roll off away from the peak frequency, which better matches the data. However, the observed bandwidth gain was shy of expectations, with a 6-dB bandwidth of 26 kHz (5% fractional bandwidth). Nevertheless, the maximum 6-dB bandwidth increased in this case by 63% compared to the maximum

6-dB bandwidth with the parallel RC model from Figure 31(d), which was 16 kHz (3% fractional bandwidth).

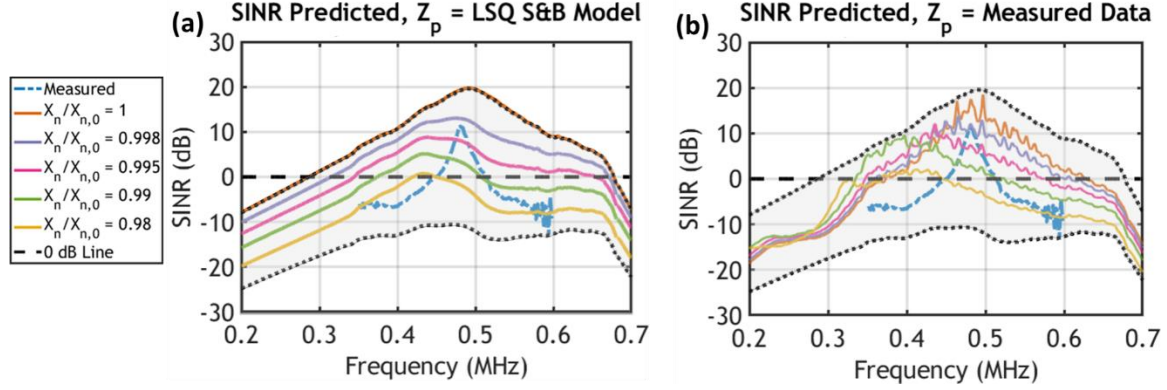


Figure 36. Extending the positive SIR bandwidth. Results are shown for a parameter sweep with a mismatch of $X_n / X_{n,0}$ by 0.2%, 0.5%, 1%, and 2%. In this notation, $n = \{1, 2, 3, 4\}$; $X_1 = C_e$; $X_2 = L_e$; $X_3 = R_e$; and $X_4 = C_0$ as defined in the S&B model of Figure 27 (with $G_0 \rightarrow \infty$). The top and bottom dashed curves represent maximum and minimum bounds on the SINR predicted by a Monte Carlo model that varied these four parameters, in addition to C_2 , by $\pm 2\%$. All predictions assume that the noise level is -54 dB re v_{in} , which matches the noise level in the measured data. Parameters used for these predictions and measurement are reported in Table 6. **(a)** Broadband SIR with Z_3 and Z_p represented by the least-squares fit to the S&B model, as presented in Figure 34(a)-(b), with the RLC parameters comprising Z_3 being varied as described above. These are compared with a measured result having a peak frequency of 481 kHz. **(b)** Predicted SIR with Z_3 represented by the S&B model and Z_p represented by its measured impedance data, with the RLC parameters comprising Z_3 being varied as described above. These are compared with the same measurement result plotted in (a).

Table 6. Parameter values used for the measurement and predictions shown in Figure 36(a)-(b). v_p was determined by the measured system function at $D = 10\text{cm}$. The measurement employed a 50 Ohm multiturn potentiometer in series with Z_3 to compensate for parasitic loss in the breadboard, cables, and wires. Maximum SIR was observed for the series resistance value reported in the table of $30.6\ \Omega$.

Fig.	V_{in}	R_0	Z_{M1}	Z_{M2}	Z_p	Z_1	Z_2	Z_3
Figure 36(a), Predictions	1.0 V_{pk}	52.8 Ω	3.3 nF	180 μH +3.0 Ω	LSQ Fit to S&B Model, Figure 34	571 pF	571 pF	LSQ Fit to S&B Model, Figure 34
Figure 36(b), Predictions	1.0 V_{pk}	52.8 Ω	3.3 nF	180 μH +3.0 Ω	Measured Values, Figure 34	571 pF	571 pF	LSQ Fit to S&B Model, Figure 34
Figure 36(a)-(b), Measurement	1.0 V_{pk-pk}	52.8 Ω	3.3 nF	180 μH +3.0 Ω	V318 Transducer	571 pF	570 pF	S&B Model: $C_0=577\ \text{pF}$ $R_e=5035\ \Omega$ $L_e=3028\ \mu\text{H}$ $C_e=44\ \text{pF}$ + $30.6\ \Omega$ (in series with Z_3)

Furthermore, although the measured SINR in Figure 36(a)-(b) falls within the bounds of the Monte Carlo simulation at all frequencies, it is worth noting that the measured 6-dB bandwidth is smaller than predicted results for $X_n / X_{n,0} = 1$, $X_n / X_{n,0} = 0.998$, and $X_n / X_{n,0} = 0.995$, as presented in Figure 36(a), and moreover it has a faster roll off away from the peak frequency, compared to most of the predicted SINR spectra. Therefore, it was of interest to determine whether the measured result for SINR could be

explained by the analytical model, with the S&B model representing Z_3 as described above. To help answer that question, a least-mean-squares solution was developed to attempt to fit the measured results to Eq. (4.2), where C_e , L_e , R_e , and C_0 are assumed to be unknowns with a maximum variation from their measured values as $\pm 2\%$, $\pm 5\%$, $\pm 10\%$, $\pm 20\%$, and $\pm 50\%$. The results are presented in Figure 37, where it can be seen that the model is able to match the measured data within 2.9 dB at all frequencies between 400 kHz and 550 kHz, given a maximum variation of $\pm 10\%$ in the least-mean-square fit. The model matches the measurement within 2.2 dB at all frequencies between 400 kHz and 550 kHz, given a maximum variation of $\pm 20\%$, and matches within 1.0 dB given a maximum variation of $\pm 50\%$. The parameters used to compute these solutions are reported below in Table 7.

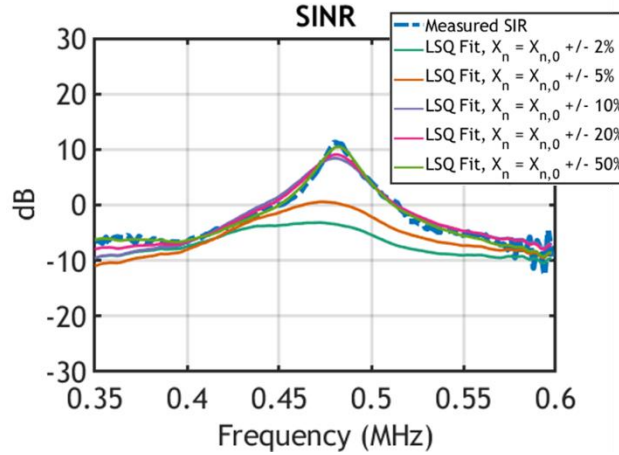


Figure 37. Best fit solutions of Eq. (4.2) to the measured broadband SINR for selected tolerances on the RLC components contained within Z_3 . Here, Z_3 is represented by the S&B model of Figure 27 and $Z_2 = 1/j\omega C_2$ is treated as an ideal capacitor. Parameters used to generate these solutions are reported in Table 7.

Table 7. Parameter values used to fit the analytical model to the measured data, as described in Figure 36. All table entries (except for the first column) list the parameter value and the percent change from the corresponding value used in the measurement of SINR. In these predictions, Z_3 is represented by the S&B model from Figure 27 (with $G_0 \rightarrow \infty$) plus a series resistance, R_s . Other parameters used were $R_0=52.8 \Omega$, $Z_{M1}=3.3$ nF, $Z_{M2} = 180 \mu\text{H} + 3 \Omega$, $Z_1= 571$ pF, and Z_p = LSQ S&B Model (reported in Figure 34).

Max. Variation	C_0	R_e	L_e	C_e	R_s	Z_2
$\pm 2\%$	589 pF (+2%)	5136 Ω (+2%)	3089 μH (+2%)	44.8 pF (+2%)	30.0 Ω (-2%)	580 pF (+2%)
$\pm 5\%$	600 pF (+4%)	5211 Ω (+4%)	3146 μH (+4%)	46.0 pF (+5%)	29.1 Ω (-5%)	589 pF (+3%)
$\pm 10\%$	609 pF (+5%)	5539 Ω (+10%)	3331 μH (+10%)	43.7 pF (-0.6%)	27.5 Ω (-10%)	600 pF (+5%)
$\pm 20\%$	636 pF (+10%)	5125 Ω (+2%)	3634 μH (+20%)	40.3 pF (-8.2%)	27.9 Ω (-8.9%)	622 pF (+9%)
$\pm 50\%$	655 pF (+13%)	5581 Ω (+11%)	4303 μH (+42%)	33.9 pF (-32.8%)	32.6 Ω (+6%)	641 pF (+13%)

5.7 TIME DIVISION AND TIME OVERLAP MEASUREMENTS

The results of peak SIR measurements were verified by acoustical measurements using tone burst signals. The results of these measurements are displayed in Figure 38 and Figure 39 for time division and time overlap cases, respectively. Figure 38(a) shows the excitation (interfering) waveform, separated in time from the much smaller signal that is reflected from the air-water interface and received by the V318 transducer. Note that the reflected signal is expected to be significantly smaller, due to the physics of transduction: The primary loss results from electromechanical coupling in the conversion of the input excitation from an electrical signal to a mechanical vibration and the subsequent conversion of the mechanical motion of the piezoelectric source into a propagating acoustic

wave. With the chosen distance, $D = 10$ cm, the loss from acoustic propagation (diffraction) is expected to be approximately 2 dB, with almost zero additional loss from the reflection due to the strong impedance contrast at the water-air interface. The returning signal then undergoes loss once again as it is converted from an acoustic wave to a mechanical vibration, and finally transduced back into an electrical signal.

In this baseline case, the signal-to-interference ratio (SIR) is -52 dB, which is determined by the ratio of the amplitude of the reflection signal to the interference signal, as shown in Figure 38(a). The second plot in Figure 38(b) displays v_{out} , which includes the SIC resulting from the bridge circuit output. Here it can be seen that an SIR of 17 dB is achieved, resulting from 56 dB of SIC on the incident signal. The parameters were $f = 459$ kHz, $R_3 = 4558 \Omega$, $C_3 = 554$ pF, and $C_2 = 560$ pF, with all other parameters matching those described in Table 5. The SIC was computed after excluding the two transient spikes at the beginning and end of the incident signal. These spikes result from the high-frequency content associated with system transients excited at the beginning and end of the burst waveforms. Figure 38(c) shows that these transients can be largely suppressed with a suitable digital filter, which in this case was implemented in post-processing with Matlab. The filter used was a causal FIR Equiripple Bandpass filter with a passband from 449 kHz to 469 kHz and order $N = 137$. Transient suppression with a bandpass filter is fundamentally limited by the finite amplitude of the impulse response of the filter, which in this case limited the amplitude suppression to 19 dB. The filtering resulted in a positive value of SIR across the entire duration of the signal. The transient problem could also be

reduced by tailoring the excitation signal with a window function, to ensure that most or all of the excitation spectrum is contained within the frequency range of positive SIR for the STAR system. However, this solution may not be possible for all signal sources.

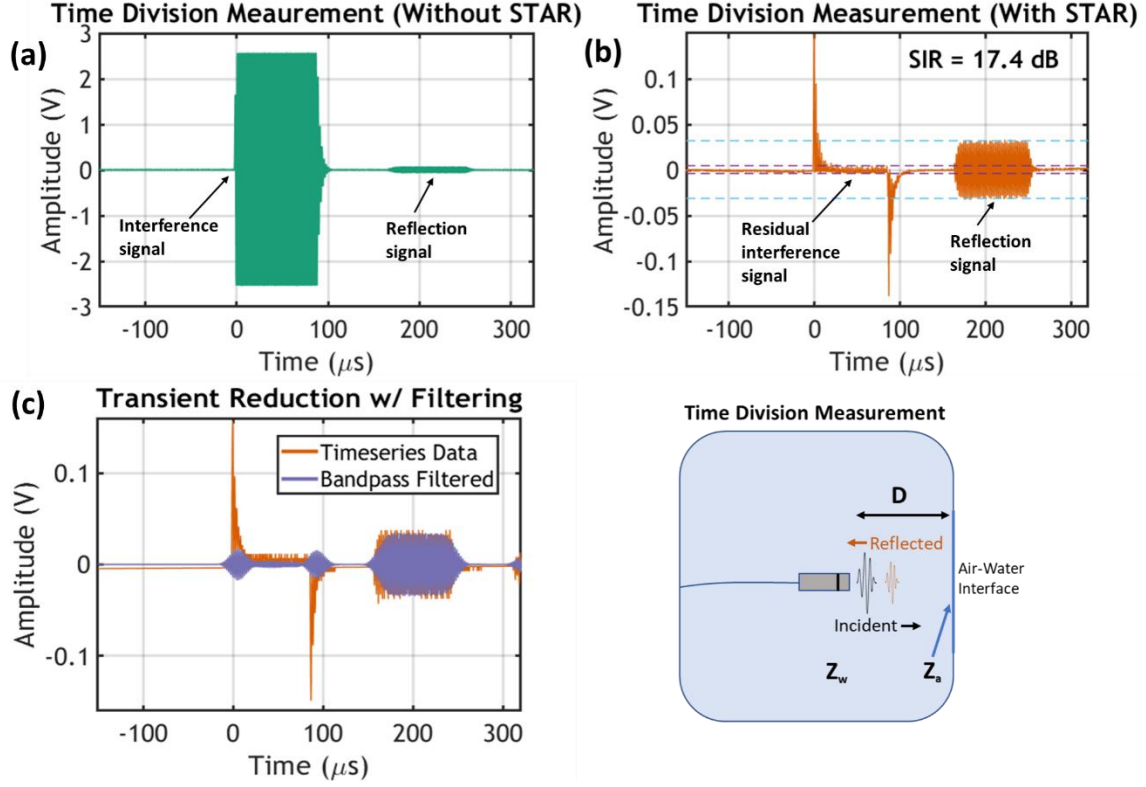


Figure 38. (a) Time division measurement without STAR cancellation. In this baseline case, the signal-to-interference ratio (SIR) is -52 dB. (b) STAR measurement with a 459 kHz sinusoidal burst having a duration of 40 cycles. This achieves an SIR of 17 dB, resulting from 56 dB of self-interference cancellation (SIC) on the incident signal. The parameters were $f = 459$ kHz, $R_3 = 4558$ Ohm, $C_3 = 554$ pF, and $C_2 = 560$ pF. (c) The time domain data from (b) is convolved with a causal digital bandpass filter in Matlab. A reduction of 19 dB is observed in the transient amplitude, which results in a positive value of SIR across the entire duration of the signal.

Finally, a time-overlap measurement is presented in Figure 39, which demonstrates a true continuous STAR measurement at ultrasonic frequencies. Figure 39(a) displays the

data corresponding to the base case, which is a burst waveform used for time-division. Time division here was achieved by shortening the number of cycles in the tone burst, rather than moving the transducer farther away, because this avoided introducing additional uncertainty that could result from small shifts in the alignment or positioning of the transducer. Figure 39(b) and (c) display longer versions of the sinusoidal burst at the same frequency, which demonstrates an ability to resolve the reflected signal at the same time that the signal is being transmitted. Various portions of the signal are highlighted, where the amplitude shifts can be attributed to interference from higher-order reflections (resulting from the normal-incidence acoustic path between the water-air interface and the stiff transducer surface). The overlapping signals can be understood as a combination of the residual input signal at the output of the bridge and the phase-shifted acoustic response of each reflection. Figure 39(b) shows that the amplitude of the first reflection is reduced by about 2 dB as compared to the same measurement in the time division case due to the partial overlap of the first reflection with the incident signal. Figure 39(c) shows that the first reflection can be observed for its entire duration while the system is continuously outputting the sine burst waveform at the same frequency, thus experimentally confirming a timeseries STAR measurement in an ultrasonic measurement system. In Figure 39(b)-(c), the SIR is still 17 dB, and the overall fluctuation in amplitude of the received signals is attributed to interference with the residual voltage signal.

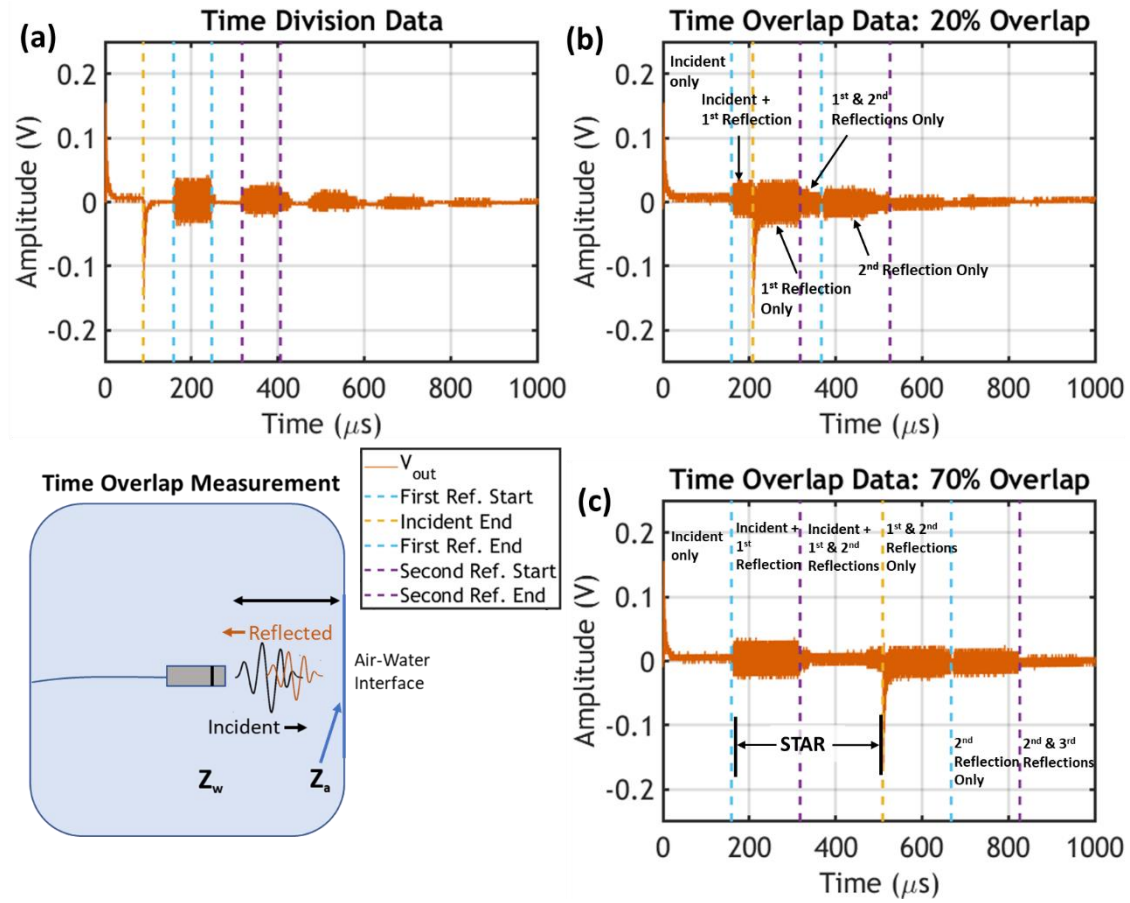


Figure 39. (a) Time-division measurement with the STAR circuit (baseline). (b) Time-overlap measurement with the STAR circuit. The incident burst has a 94-cycle duration at 452 kHz, which results in approximately a 20% overlap of the first reflection and the incident signal in the time domain. (c) Time-overlap measurement with a 230-cycle period, resulting in approximately 70% overlap of the first reflection and the incident signal.

5.8 CONCLUSIONS

In this chapter, we have shown that a fully passive LC-matched bridge circuit model can be used to achieve broadband SIC in acoustic measurement systems. Good agreement was demonstrated between linear system models and an experimental proof-of-concept. It was shown that with the proper choice of circuit parameters, large positive values of SIR can be measured, and that the peak SIR frequency can be tuned. It was further demonstrated that higher-order RLC transducer models could significantly extend the useful bandwidth of the system to as high as 298 kHz (60% fractional bandwidth) with the V318 immersion transducer, although a more realistic model places the upper bound for bandwidth at 143 kHz (29% fractional bandwidth). These results can be viewed as a first important step towards more robust acoustic STAR systems, which may include an additional digital cancellation stage for dynamically optimizing SIC. Future work may incorporate detailed propagation models in order to extend the functionality of STAR for near-surface imaging, as an alternative or supplement to matched filtering approaches in order to directly address problems in ultrasonic NDE and biomedical imaging. Further extensions of these models are expected to result in a broad variety of applications for acoustic STAR, including Doppler ultrasound, ballistocardiography, phonocardiography, simultaneous microphone transceivers, and full-duplex underwater communication systems.

Chapter VI: Conclusions and Future Directions

6.1 CONCLUSIONS AND CONTRIBUTIONS

The principal objective of this dissertation is to determine with analytical, numerical, and experimental investigations the feasibility of extraordinary acoustic transmission phenomena, such as membrane-free acoustic supercoupling and acoustic self-interference cancellation.

The principal research objective, as originally stated in Chapter I, was satisfied through successful investigations of both membrane-free acoustic supercoupling and acoustic self-interference cancellation, as presented in Chapters III-V. Satisfaction of this objective was also supported by a review of the fundamental concepts and background works, presented in Chapter II, which motivated the usefulness of membrane-free acoustic supercoupling and self-interference cancellation (SIC) for acoustic measurement systems. Chapter II is also the first work known to us to have unified concepts regarding self-interference cancellation from diverse fields of study including radio frequency communications, Wi-Fi, acoustic nondestructive evaluation, underwater acoustic communications, vibration control, and self-sensing actuators.

In Chapter III, we presented theoretical and experimental validation of a straightforward way of realizing zero compressibility acoustic wave propagation in waveguides, by exciting a higher-order mode at the cut-off frequency. Our theoretical results accurately capture the physics behind this anomalous tunneling, and our

experiments confirm large phase velocity and anomalous transmission independent of the channel length. We have also shown that an acoustic power divider can be realistically implemented with interesting features, such as the capability of transmitting power with uniform phase to an arbitrary number of output ports, independent of the placement of the ports along the central region of the channel. Practical limitations in terms of scaling the size of the device were considered, including trade-offs between visco-thermal loss and the uniformity of power and phase. This approach to dividing acoustic power allows for great flexibility in design, given the length-independent properties of the supercoupling channel.

Chapter IV presented system models that demonstrated a fully passive LC-matched bridge circuit can achieve broadband SIC in acoustic measurement systems. It was shown that a signal-to-interference ratio (SIR) of greater than 20 dB can be achieved in a model problem with proper choices of parameter values in the cancellation circuit. Furthermore, the sensitivity of the design equations to various configurations with impedance mismatch were assessed, and this was shown to be a significant factor for SIC system design and implementation. These concepts were further developed in Chapter V, where an experimental design was described, and successful measurement results were presented. Good agreement was demonstrated between linear system models and an experimental proof-of-concept. It was shown that with the proper choice of circuit parameters, large positive values of SIR of greater than 17 dB can be measured (corresponding to 56 dB of SIC) and that the peak SIR frequency can be tuned. It was further demonstrated that higher-order RLC transducer models could significantly extend the useful bandwidth of the simultaneous transmit and receive (STAR) acoustic system.

The work presented in this dissertation led to the publication of three conference presentations, two peer-reviewed journal publications [144],[145], and two additional manuscripts in preparation for STAR acoustics.

6.2 FUTURE DIRECTIONS

Our work on compressibility-near-zero acoustic supercoupling opens possibilities for acoustic supercoupling devices with a variety of potential applications. We envision a wide range of applicability of CNZ supercoupling, for use in acoustic sensing [139], for the tailoring of acoustic radiation patterns [27][140], for acoustic lensing [141], and for enhanced acoustic nonlinearities and sound-matter interactions [29],[58]. The length-independent power divider can be used for multiplexing acoustic signals with opposite phases and differing weights, with potential applicability to feeding passive acoustic arrays, and in loss-compensating interferometry [136].

The results for SIC in acoustic measurement systems can be viewed as a first important step towards more robust acoustic simultaneous transmit and receive (STAR) systems, which may include an additional digital cancellation stage for dynamically optimizing SIC. Future work may incorporate detailed propagation models in order to extend the functionality of STAR for near-surface imaging, as an alternative or supplement to matched filtering approaches in order to directly address problems in ultrasonic NDE and biomedical imaging. Further extensions of these models are expected to result in a broad variety of applications for acoustic STAR, including doppler ultrasound, ballistocardiography, phonocardiography, simultaneous microphone transceivers, and full-

duplex underwater communication systems, as discussed in Section 2.2.3. Further avenues for development of STAR acoustics are discussed below.

6.2.1 Near-Surface Acoustic Imaging with Self-Interference Cancellation

One of the promising applications of STAR or SIC in acoustics is the possibility of leveraging the cancellation process to improve near-surface imaging resolution of ultrasonic measurement systems, as discussed in Section 2.2.3. Presently, near-surface ultrasonic imaging is conducted with a few common approaches: 1) the use of a delay line or “stand-off” medium to delay the reflection from the surface, thereby reducing the duration of the acoustic “blind zone” in the timeseries echo, 2) signal processing techniques such as deconvolution (similar to matched filtering or pulse compression), wavelet transforms, and/or machine learning [146], and 3) diffuse field reconstruction [128] or alternative time of flight detection [147].

The use of delay lines has drawbacks, including reduced acoustic coupling, the introduction of additional acoustic modes that may interfere with measurements, and an increased physical profile of the transducer. Signal processing approaches generally assume that either an accurate propagation model of the medium is already known, or that one can be trained with machine learning approaches. However, machine learning can require large and diverse training datasets in order to accurately model a system, which is not always feasible when there are constraints on time, physical space, and/or financial resources to conduct sufficient testing. The third method, diffuse field reconstruction,

assumes that an inverse model can be solved to reconstruct a scattering solution from near-surface defects using the “diffuse” portion of the excitation, *i.e.* the portion of the excitation that is not in the blind zone. While the last two methods have shown good success in uncovering flaws in simple materials, additional challenges exist in resolving defects within materials that have more complex acoustic properties, such as carbon fiber reinforced polymer (CFRP) [128]. CFRP has strong acoustic scattering and absorption which makes it a challenging material to image, but yet it is highly sought after for its high strength-to-weight ratio and stiffness.

As an alternative approach for near-surface imaging, acoustic SIC can be employed to resolve the echo return from a near-surface defect while it is within the blind zone of the transducer. This approach assumes, different from the prior three approaches, that the input impedance of the device under test (DUT) is known or can be accurately measured. The input impedance can alternatively be expressed as an acoustic radiation impedance in a transducer model [143]. Although this method also fundamentally relies on a propagation model, which is used to define the input impedance, it is the objective of this current effort to determine whether the SIC approach to near-surface imaging has any advantages. For example, it is possible that this approach would introduce less error into the image processing algorithm as compared to other model-based approaches.

To test these assumptions, an experimental setup was constructed from aluminum, with six cylindrical defects engineered at various distances offset from the flat surface of the material, as shown in Figure 40(a) and pictured in Figure 40(b). The sample was designed to be measured in water for increased confidence in coupling from the transducer

to the solid material sample and better measurement repeatability, as compared to in-air testing with an ultrasonic coupling gel. The top cover of the sample was epoxied to the bottom section to seal the defects from water penetration, which will better mimic an internal crack in the material and also result in a stronger echo return from the flaw (as compared to a water-filled flaw that is measured while submerged in water). Finally, a test rig was designed and 3D-printed to support an ultrasonic immersion transducer to make normal incidence measurements of each flaw, as shown in Figure 41(a). The test rigging was designed to minimize the amount of material surrounding the top of the test sample, which should reduce multiple scattering in the echo data. Rectangular notches were designed to hold the transducer at normal incidence to the face of the test sample, shown in Figure 41(b). Figure 41(c) shows the 3D-printed test rigging without the aluminum sample present. *Measurement results and analysis of this near-surface imaging approach are planned for a future publication.*

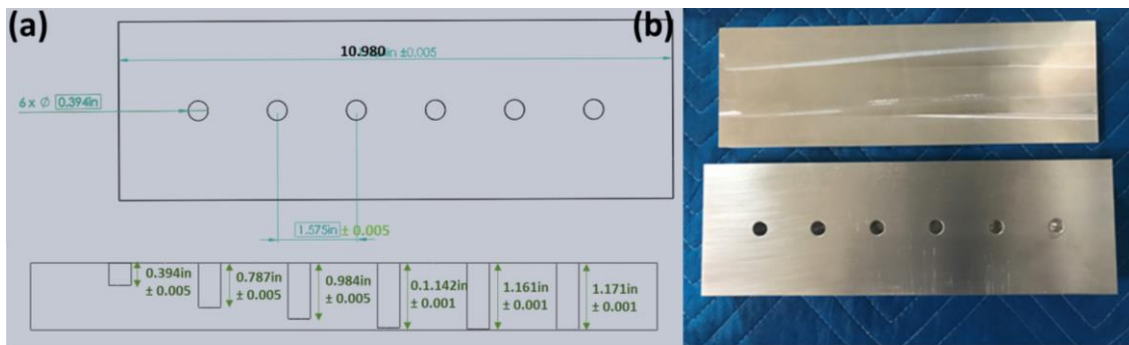


Figure 40. (a) Schematic of near-surface test sample. Transducer measurements are made from the bottom side of the test sample as shown at the bottom of (a). Distances to each flaw are 20 mm, 10 mm, 5 mm, 1 mm, 0.5 mm, and 0.25 mm. Lateral hole spacing was designed to be 5λ at 1 MHz. (b) Picture of the test sample, including top cover which is used to seal the sample from water.

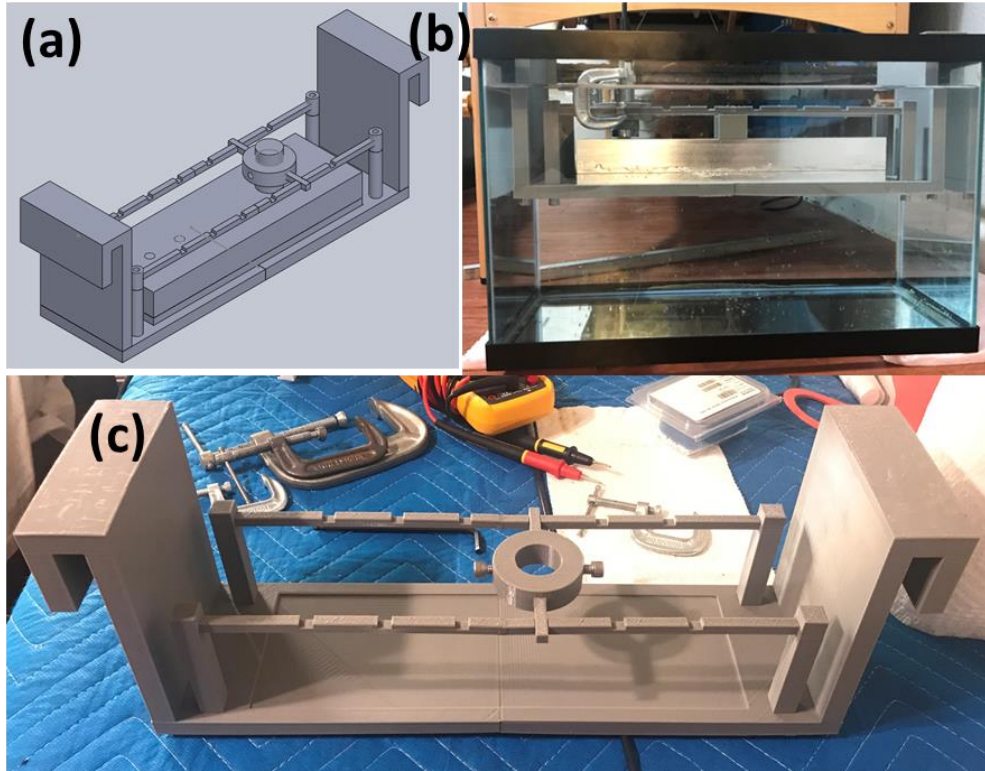


Figure 41. Experimental setup for near-surface acoustic imaging with self-interference cancellation.

6.2.2 Enhancing Doppler Shift Detection with Acoustic Self-Interference Cancellation

Another interesting avenue for the application of acoustic SIC is in measurements of the acoustic doppler shift. Doppler measurements in acoustics are most commonly used in a medical setting to non-invasively measure the flow of blood [148]. However, acoustic doppler measurements have also been used for measurement of wind velocity in the atmosphere [149] and the flow of rivers for geological studies [150]. When determining velocity with a doppler measurement, the size of the doppler shift represents the amplitude of the change that is detected by the doppler sensor. If the amplitude of that change can be

increased, this will effectively result in an increased signal-to-noise ratio (SNR) of the doppler measurement (although this would not affect the amplitude of the signal, but rather the amplitude of the detected quantity). To see how the SNR of a doppler system can be increased with acoustic SIC, consider the expression for doppler shift in a volumetric blood flow measurement, as given by [151]:

$$\bar{V} = \frac{\overline{\Delta f} c}{2 f_{tr} \cos \theta} \quad (6.1)$$

where \bar{V} is the volumetric flow rate of the blood, $\overline{\Delta f}$ is the average doppler shift measured due to the blood flow measured from an angle θ with respect to direction of flow, c is the speed of sound in the blood, and f_{tr} is the frequency of the transmitted wave. Re-arranging expression (6.1) yields

$$\frac{\overline{\Delta f}}{2 f_{tr} \cdot \bar{V} / c} = \cos \theta \quad (6.2)$$

Here, $\overline{\Delta f} / (2 f_{tr} \cdot \bar{V} / c)$ is the doppler shift normalized by three parameters which can all be held constant in a given measurement. It can be seen that the normalized doppler shift is simply a cosine function, as shown in Figure 42. From this result, we see that the doppler shift is maximized with the choice of $\theta = 0$ deg., and that the magnitude of the shift is decreased if we must measure at a greater angle. For example, if $\theta = 60$ deg., then the normalized doppler shift is 0.5, which represents a 6 dB reduction in the magnitude of the shift.

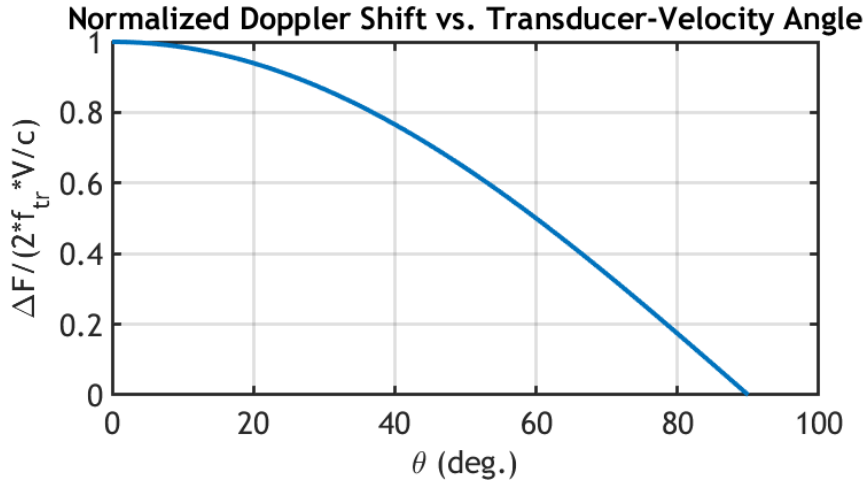


Figure 42. Normalized doppler shift plotted against the angle of the transducer from the blood vessel.

Now, consider a bi-static doppler measurement system, as displayed in Figure 43(a), which sends a doppler pulse with the transducer labeled TX and receives the echo with the transducer labeled RX. In this case, maximal doppler shift will be observed when $\phi = 90$ deg, which corresponds to $\theta = 0$ deg. in (6.2). This case represents a monostatic measurement, meaning that both the TX and RX transducers are co-located at the point M in Figure 43(a). However, in many applications it may not be possible to co-locate the TX and RX transducers, as doing so could result in the measurement taking place in the acoustic blind zone, (defined in Section 6.2.1). Bi-static acoustic measurements can avoid the blind zone by using directivity of the acoustic beam to isolate the TX and RX nodes from direct path interference and then leveraging the larger path length of the bi-static echo return. However, this comes at a cost, as increasing the bi-static angle also reduces the amount of doppler shift observed. *This limitation can be overcome with acoustic SIC, as the blind zone can be avoided by the removal of the self-interfering signal with a system*

similar to the one presented in Chapters IV-V, and therefore a monostatic configuration with maximal doppler shift can be made possible.

To see the limits of the acoustic blind zone for a monostatic doppler measurement, consider an expression for the blind zone duration based on a constant sound speed time-of-flight approximation, with pulse duration T , distance from the scatterer D , and speed of sound c_0 :

$$t_{BZ} = T - \frac{2D}{c_0} \quad (6.3)$$

Expression (6.3) is plotted in Figure 43(b) (normalized by T) for three different common sound speeds in acoustics: air, water, and aluminum. From the figure, we can see that, when the distance to the scatterer approaches zero, then the normalized blind zone duration approaches 1, which means that the measurement must take place entirely when the echo is within the blind zone of the transmitted signal. However, as the distance from the scatterer is increased, we can see that the blind zone will go to zero (and then become negative as D is further increased). The distance at which this occurs depends upon the speed of sound of the medium, with a faster sound speed requiring a greater distance to escape the blind zone.

Another interesting advantage of acoustic SIC for doppler applications is that the SIC process may enable bi-static measurement configurations at lower frequencies than were possible previously. This can be explained by the plot in Figure 43(c), which shows the ratio of the bi-static blind zone duration to the monostatic blind zone duration, as a function of distance from the moving target, in the case of omnidirectional transducers

(zero isolation from directivity). We can see that this ratio is always greater than one, and gets significantly worse with longer distances to the target, which results from the expression

$$\frac{t_{BZ,bs}}{t_{BZ,ms}} = \frac{1 + \frac{2(D/T)}{c_0} \left(\frac{1}{\tan \theta} - \frac{1}{\sin \theta} \right)}{1 - \frac{2(D/T)}{c_0}} \quad (6.4)$$

Expression (6.4) is derived solely from geometrical relations and an assumption of constant speed of sound for the time-of-flight calculation. This figure highlights the *disadvantage* of operating in a bi-static configuration without isolation from directivity, as the larger bi-static angles will impose more restrictions upon the distance to the scatterer that can be successfully resolved (given that the plotted ratio is always greater than 1, this means that the blind zone duration will always be greater for bi-static vs. monostatic in the absence of directivity isolation). *However, if acoustic SIC is employed to eliminate the direct path interfering signal, then we can maximize doppler shift measured for velocity vectors that are at oblique angles to the line between the TX and RX nodes, and we can do so at lower frequencies for which high directivity transducers are unavailable or difficult to produce.*

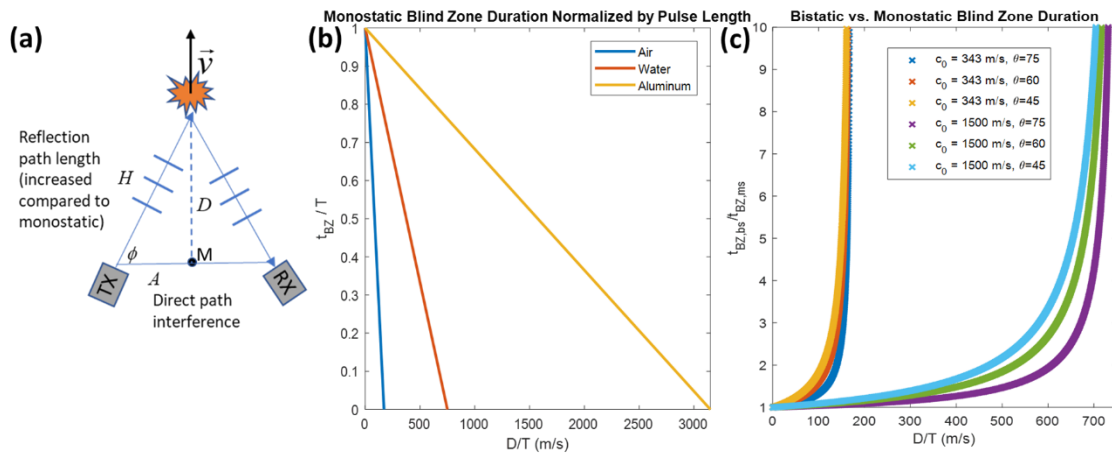


Figure 43. (a) Bi-static doppler measurement system that measures the velocity of a moving scatterer in a direction normal to the plane connecting the transducers. (b) Blind zone duration of a monostatic doppler measurement system for three different fluid materials. (c) Ratio of the bi-static blind zone duration to the monostatic blind-zone duration, in the absence of any directivity for the TX and RX transducers.

Bibliography

- [1] D. G. Stork and R. E. Berg, *The Physics of Sound*, 3rd ed. Pearson, 2004.
- [2] D. T. Blackstock, *Fundamentals of Physical Acoustics*. Hoboken: Wiley-Interscience, 2000.
- [3] L. E. Kinsler, A. R. Frey, A. B. Coppers, and J. V. Sanders, *Fundamentals of Acoustics*. Wiley, 1999.
- [4] V. G. Veselago, “The electrodynamics of substances with simultaneously negative values of ϵ and μ ,” *Sov. Phys. Uspekhi*, vol. 10, no. 4, p. 509, 1968.
- [5] D. R. Smith, W. J. Padilla, D. C. Vier, and S. C. Nemat-Nasser, “Composite medium with simultaneously negative permeability and permittivity,” *Phys. Rev. Lett.*, vol. 84, no. 18, pp. 4184–4187, 2000.
- [6] J. B. Pendry, “Negative refraction makes a perfect lens,” *Phys. Rev. Lett.*, vol. 85, no. 18, pp. 3966–3969, 2000.
- [7] Z. Liu *et al.*, “Locally resonant sonic materials,” *Science*, vol. 289, no. 5485, pp. 1734–1736, 2000.
- [8] S. A. Cummer, J. Christensen, and A. Alù, “Controlling sound with acoustic metamaterials,” *Nat. Rev. Mater.*, no. 1:16001, 2016.
- [9] G. Ma and P. Sheng, “Acoustic metamaterials: From local resonances to broad horizons,” *Sci. Adv.*, vol. 2, no. 2, p. e1501595, 2016.
- [10] M. Dubois, C. Shi, X. Zhu, Y. Wang, and X. Zhang, “Observation of acoustic dirac-like cone and double zero refractive index,” *Nat. Commun.*, no. 8:14871, 2017.
- [11] V. C. Nguyen, L. Chen, and K. Halterman, “Total transmission and total reflection by zero index metamaterials with defects,” *Phys. Rev. Lett.*, vol. 105, no. 233908, 2010.
- [12] B. Edwards, A. Alù, M. E. Young, M. G. Silveirinha, and N. Engheta, “Experimental verification of epsilon-near-zero metamaterial at microwave frequencies,” *Phys. Rev. Lett.*, vol. 100, p. 033903, 2008.
- [13] B. Edwards, A. Alù, M. Silveirinha, and N. Engheta, “Reflectionless sharp bends and corners in waveguides using epsilon-near-zero effects,” *J. Appl. Phys.*, vol. 105, no. 044905, 2009.
- [14] M. G. Silveirinha and N. Engheta, “Theory of supercoupling, squeezing wave energy, and field confinement in narrow channels and tight bends using epsilon-near-zero metamaterials,” *Phys. Rev. B*, vol. 76, no. 245109, 2007.

- [15] A. Alù, M. G. Silveirinha, and N. Engheta, “Transmission-line analysis of epsilon-near-zero-filled narrow channels,” *Phys. Rev. E*, vol. 78, no. 016604, 2008.
- [16] R. Fleury, D. L. Sounas, C. F. Sieck, M. R. Haberman, and A. Alù, “Sound Isolation and Giant Linear Nonreciprocity in a Compact Acoustic Circulator,” *Science*, vol. 343, no. January, pp. 516–519, 2014.
- [17] R. Fleury, D. L. Sounas, and A. Alù, “Subwavelength ultrasonic circulator based on spatiotemporal modulation,” *Phys. Rev. B - Condens. Matter Mater. Phys.*, vol. 91, no. 17, pp. 1–9, 2015, doi: 10.1103/PhysRevB.91.174306.
- [18] Y. Hadad, J. C. Soric, and A. Alu, “Breaking temporal symmetries for emission and absorption,” *Proc. Natl. Acad. Sci. U. S. A.*, vol. 113, no. 13, pp. 3471–3475, 2016, doi: 10.1073/pnas.1517363113.
- [19] R. Fleury, A. B. Khanikaev, and A. Alù, “Floquet topological insulators for sound,” *Nat. Commun.*, vol. 7, 2016, doi: 10.1038/ncomms11744.
- [20] H. Nassar *et al.*, “Nonreciprocity in acoustic and elastic materials,” *Nat. Rev. Mater.*, vol. 5, no. 9, pp. 667–685, 2020, doi: 10.1038/s41578-020-0206-0.
- [21] D. M. Pozar, *Microwave Engineering*, 4th ed. Wiley, 2011.
- [22] J. Il Choi, M. Jain, K. Srinivasan, P. Levis, and S. Katti, “Achieving Single Channel, Full Duplex Wireless Communication,” in *SIGCOMM 2010*, 2010, pp. 1–12, doi: 10.1145/1859995.1859997.
- [23] T. Vossing, J. Rautenberg, and B. Henning, “Simultaneous Transmitting and Receiving with Ultrasonic Sensors,” in *SENSOR Conference 2007 Proceedings II*, 2007, pp. 69–74.
- [24] J. J. Dosch and D. J. Inman, “Self-Sensing Piezoelectric Actuator,” *J. Intell. Mater. Syst. Struct.*, vol. 3, pp. 166–185, 1992.
- [25] N. Engheta, “Pursuing near-zero response,” *Science*, vol. 340, pp. 286–287, 2013.
- [26] R. W. Ziolkowski, “Propagation in and scattering from a matched metamaterial having a zero index of refraction,” *Phys. Rev. E*, vol. 70, no. 046608, 2004.
- [27] A. Alù, M. G. Silveirinha, A. Salandrino, and N. Engheta, “Epsilon-near-zero metamaterials and electromagnetic sources: tailoring the radiation phase pattern,” *Phys. Rev. B*, vol. 75, no. 155410, 2007.
- [28] A. Alù and N. Engheta, “Light squeezing through arbitrarily shaped plasmonic channels and sharp bends,” *Phys. Rev. B*, vol. 78, no. 035440, 2008.
- [29] C. Argyropoulos, P. Chen, G. D’Aguanno, N. Engheta, and A. Alù, “Boosting optical nonlinearities in epsilon-near-zero plasmonic channels,” *Phys. Rev. B*, vol. 85, no. 045129, 2012.
- [30] X. Huang, Y. Lai, Z. H. Hang, H. Zheng, and C. T. Chan, “Dirac cones induced by accidental degeneracy in photonic crystals and zero-refractive-index materials,”

Nat. Mater., vol. 10, pp. 582–586, 2011.

- [31] I. Liberal, A. M. Mahmoud, Y. Li, B. Edwards, and N. Engheta, “Photonic doping of epsilon-near-zero media,” *Science*, vol. 355, pp. 1058–1062, 2017.
- [32] R. Liu *et al.*, “Experimental demonstration of electromagnetic tunneling through an epsilon-near-zero metamaterial at microwave frequencies,” *Phys. Rev. Lett.*, vol. 100, no. 2, pp. 1–4, 2008, doi: 10.1103/PhysRevLett.100.023903.
- [33] Y. Xu and H. Chen, “Total reflection and transmission by epsilon-near-zero metamaterials with defects,” *Appl. Phys. Lett.*, vol. 98, no. 113501, 2011.
- [34] M. G. Silveirinha and N. Engheta, “Tunneling of electromagnetic energy through subwavelength channels and bends using epsilon-near-zero materials,” *Phys. Rev. Lett.*, vol. 97, no. 157403, 2006.
- [35] A. M. Mahmoud and N. Engheta, “Wave-matter interactions in epsilon-and-mu-near-zero structures,” *Nat. Commun.*, vol. 5, no. 5638, 2014.
- [36] A. R. Davoyan, A. M. Mahmoud, and N. Engheta, “Optical isolation with epsilon-near-zero metamaterials,” *Opt. Express*, vol. 21, pp. 3279–3286, 2013.
- [37] J. S. Marcos, M. G. Silveirinha, and N. Engheta, “ μ -near-zero supercoupling,” *Phys. Rev. B*, vol. 91, no. 195112, 2015.
- [38] I. Liberal and N. Engheta, “Near-zero refractive index photonics,” *Nat. Photonics*, vol. 11, no. 149–158, 2017.
- [39] M. G. Silveirinha and N. Engheta, “Design of matched zero-index metamaterials using nonmagnetic inclusions in epsilon-near-zero media,” *Phys. Rev. B*, vol. 75, no. 075119, 2007.
- [40] C. J. Naify, C. N. Layman, T. P. Martin, M. Nicholas, D. C. Calvo, and G. J. Orris, “Experimental realization of a variable index transmission line metamaterial as an acoustic leaky-wave antenna,” *Appl. Phys. Lett.*, vol. 102, no. 20, pp. 1–5, 2013, doi: 10.1063/1.4807280.
- [41] Z. Liang and J. Li, “Extreme acoustic metamaterial by coiling up space,” *Phys. Rev. Lett.*, vol. 108, no. 114301, 2012.
- [42] H. Esfahlani, S. Karkar, H. Lissek, and J. R. Mosig, “Acoustic dispersive prism,” *Sci. Rep.*, vol. 6, no. 18911, 2016.
- [43] H. Esfahlani, S. Karkar, H. Lissek, and J. R. Mosig, “Exploiting the leaky-wave properties of transmission-line metamaterials for single-microphone direction finding,” *J. Acoust. Soc. Am.*, vol. 139, pp. 3259–3266, 2016.
- [44] Y. Jing, J. Xu, and N. X. Fang, “Numerical study of a near-zero-index acoustic metamaterial,” *Phys. Lett. A*, vol. 376, pp. 3259–3266, 2012.
- [45] R. Fleury and A. Alù, “Extraordinary sound transmission through density-near-zero ultranarrow channels,” *Phys. Rev. Lett.*, vol. 111, p. 055501, 2013.

- [46] C. J. Naify, C. A. Rohde, T. P. Martin, M. Nicholas, M. D. Guild, and G. J. Orris, "Generation of topologically diverse acoustic vortex beams using a compact metamaterial aperture," *Appl. Phys. Lett.*, vol. 108, no. 22, pp. 3–7, 2016, doi: 10.1063/1.4953075.
- [47] C. W. Broadman, C. J. Naify, M. J. Lee, and M. R. Haberman, "Design of a one-dimensional underwater acoustic leaky wave antenna using an elastic metamaterial waveguide," *J. Appl. Phys.*, vol. 129, no. 19, p. 194902, 2021, doi: 10.1063/5.0044802.
- [48] C. A. Balanis, *Advanced Engineering Electromagnetics*, 1st ed. John Wiley & Sons, 1989.
- [49] F. Bongard, H. Lissek, and J. R. Mosig, "Acoustic transmission line metamaterial with negative/zero/positive refractive index," *Phys. Rev. B*, vol. 82, no. 094306, 2010.
- [50] L. J. Wang, A. Kuzmich, and A. Dogariu, "Gain-assisted superluminal light propagation," *Nature*, vol. 406, pp. 277–279, 2000.
- [51] A. Alù and N. Engheta, "Achieving transparency with plasmonic and metamaterial coatings," *Phys. Rev. E*, vol. 72, no. 016623, 2005.
- [52] A. Alù and N. Engheta, "Plasmonic materials in transparency and cloaking problems: mechanism, robustness, and physical insights," *Opt. Expr.*, vol. 15, pp. 3318–3332, 2007.
- [53] J. Hao, W. Yan, and M. Qiu, "Super-reflection and cloaking based on zero index metamaterial," *Appl. Phys. Lett.*, vol. 96, no. 101109, 2010.
- [54] H. F. Ma, J. H. Shi, Q. Cheng, and T. J. Cui, "Experimental verification of supercoupling and cloaking using mu-near-zero materials based on a waveguide," *Appl. Phys. Lett.*, vol. 103, no. 021908, 2013.
- [55] S. Enoch, G. Tayeb, P. Sabouroux, N. Guerin, and P. Vincent, "A metamaterial for directive emission," *Phys. Rev. Lett.*, vol. 89, no. 213902, 2002.
- [56] Y. Yu, L. Shen, L. Ran, T. Jiang, J. Huangfu, and J. A. Kong, "Directive emission based on anisotropic metamaterials," *Phys. Rev. A*, vol. 77, no. 053821, 2008.
- [57] H. F. Ma, J. H. Shi, B. G. Cai, and T. J. Cui, "Total transmission and super reflection realized by anisotropic zero-index materials," *New. J. Phys.*, vol. 14, no. 123010, 2012.
- [58] A. Alù and N. Engheta, "Boosting molecular fluorescence with a plasmonic nanolauncher," *Phys. Rev. Lett.*, vol. 103, no. 043902, 2009.
- [59] N. Cselyuszka, M. Sećujski, and V. C. Bengin, "Compressibility-near-zero acoustic metamaterial," *Phys. Lett. A*, vol. 378, pp. 1153–1156, 2014.
- [60] M. B. Muhlestein, C. F. Sieck, P. S. Wilson, and M. R. Haberman, "Experimental

- evidence of Willis coupling in a one-dimensional effective material element,” *Nat. Commun.*, vol. 8, pp. 1–9, 2017, doi: 10.1038/ncomms15625.
- [61] A. Lai, K. M. Leong, and T. Itoh, “Infinite wavelength resonant antennas with monopolar radiation pattern based on periodic structures,” *IEEE Trans. Antennas Propag.*, vol. 55, no. 868, 2007.
 - [62] A. Lai, K. M. Leong, and T. Itoh, “A novel N-port series divider using infinite wavelength phenomena,” in *IEEE MTT-S Int. Microw. Symp. Dig.*, 2005, p. 1001.
 - [63] M. A. Antoniadou and G. V. Eleftheriades, “A broadband series power divider using zero-degree metamaterial phase-shifting lines,” *IEEE Micro. Compon. Lett.*, vol. 15, no. 808, 2005.
 - [64] A. Lai, K. M. Leong, and T. Itoh, “Novel series divider for antenna arrays with arbitrary element spacing based on a composite right/left-handed transmission line,” in *European Microwave Conference*, 2005, p. 4.
 - [65] H. V. Nguyen and C. Caloz, “Tunable arbitrary N-port CRLH infinite-wavelength series power divider,” *Electron. Lett.*, vol. 43, no. 1292, 2007.
 - [66] Z. Zhou *et al.*, “General impedance matching via doped epsilon-near-zero media,” *Phys. Rev. Appl.*, vol. 13, no. 034005, 2020.
 - [67] W. L. Stutzman and G. A. Thiele, *Antenna Theory and Design*. New York, NY: Wiley, 1998.
 - [68] G. W. Stewart, “The theory of the Herschel-Quincke tube,” *Phys. Rev.*, vol. 31, no. 4, pp. 696–698, 1928, doi: 10.1103/PhysRev.31.696.
 - [69] G. W. Stewart, “The Theory of the Herschel-Quincke Tube,” *J. Acoust. Soc. Am.*, vol. 17, no. 2, pp. 107–108, 1945, doi: 10.1121/1.1916304.
 - [70] F. Zangeneh-Nejad and R. Fleury, “Acoustic rat-race coupler and its applications in non-reciprocal systems,” *J. Acoust. Soc. Am.*, vol. 146, no. 1, pp. 843–849, 2019, doi: 10.1121/1.5115020.
 - [71] D. Bharadia, E. McMillin, and S. Katti, “Full duplex radios,” *SIGCOMM 2013*, pp. 375–386, 2013, doi: 10.1145/2486001.2486033.
 - [72] A. Balatsoukas-Stimming, “Non-Linear Digital Self-Interference Cancellation for In-Band Full-Duplex Radios Using Neural Networks,” *IEEE Work. Signal Process. Adv. Wirel. Commun. SPAWC*, vol. 2018-June, 2018, doi: 10.1109/SPAWC.2018.8445987.
 - [73] M. Jain, J. Il Choi, K. Srinivasan, P. Levis, S. Katti, and S. Seth, “Single Channel Full Duplex Wireless Communications,” US Patent No. 9887728, 2018.
 - [74] A. Kord, D. L. Sounas, and A. Alu, “Achieving Full-Duplex Communication,” *IEEE Microw. Mag.*, vol. 19, no. 1, pp. 84–90, 2018, doi: 10.1109/MMM.2017.2759638.

- [75] P. V. Prasannakumar, M. A. Elmansouri, L. B. Boskovic, M. Ignatenko, and D. S. Filipovic, "Wideband Quasi-Monostatic Simultaneous Transmit and Receive Reflector Antenna," *IEEE Trans. Antennas Propag.*, vol. 68, no. 4, pp. 2630–2637, 2020, doi: 10.1109/TAP.2019.2955143.
- [76] H. Alshammary, C. Hill, A. Hamza, and J. F. Buckwalter, "A Code-Domain RF Signal Processing Front End With High Self-Interference Rejection and Power Handling for Simultaneous Transmit and Receive," *IEEE J. Solid-State Circuits*, vol. 55, no. 5, pp. 1199–1211, 2020, doi: 10.1109/jssc.2019.2960486.
- [77] I. T. Cummings, J. P. Doane, T. J. Schulz, and T. C. Havens, "Aperture-Level Simultaneous Transmit and Receive with Digital Phased Arrays," *IEEE Trans. Signal Process.*, vol. 68, pp. 1243–1258, 2020, doi: 10.1109/TSP.2020.2968262.
- [78] E. Everett, A. Sahai, and A. Sabharwal, "Passive self-interference suppression for full-duplex infrastructure nodes," *IEEE Trans. Wirel. Commun.*, vol. 13, no. 2, pp. 680–694, 2014, doi: 10.1109/TWC.2013.010214.130226.
- [79] V. Syrjälä, M. Valkama, L. Anttila, T. Riihonen, and D. Korpi, "Analysis of oscillator phase-noise effects on self-interference cancellation in full-duplex OFDM radio transceivers," *IEEE Trans. Wirel. Commun.*, vol. 13, no. 6, pp. 2977–2990, 2014, doi: 10.1109/TWC.2014.041014.131171.
- [80] D. Korpi, T. Riihonen, V. Syrjälä, L. Anttila, M. Valkama, and R. Wichman, "Full-duplex transceiver system calculations: Analysis of ADC and linearity challenges," *IEEE Trans. Wirel. Commun.*, vol. 13, no. 7, pp. 3821–3836, 2014, doi: 10.1109/TWC.2014.2315213.
- [81] E. Ahmed and A. M. Eltawil, "All-Digital Self-Interference Cancellation Technique for Full-Duplex Systems," *IEEE Trans. Wirel. Commun.*, vol. 14, no. 7, pp. 3519–3532, 2015.
- [82] F. H. Gregorio, G. J. González, J. Cousseau, T. Riihonen, and R. Wichman, "RF front-end implementation challenges of in-band full-duplex relay transceivers," *Eur. Wirel. Conf. 2016*, pp. 257–262, 2016.
- [83] D. Bharadia and S. Katti, "Full-duplex Radios," in *Towards 5G: Applications, Requirements, and Candidate Technologies*, 2017, pp. 364–394.
- [84] S. Kim, M. S. Sim, C. B. Chae, and S. Choi, "Asymmetric simultaneous transmit and receive in wifi networks," *IEEE Access*, vol. 5, pp. 14079–14094, 2017, doi: 10.1109/ACCESS.2017.2723562.
- [85] A. Masmoudi and T. Le-Ngoc, "Channel Estimation and Self-Interference Cancellation in Full-Duplex Communication Systems," *IEEE Trans. Veh. Technol.*, vol. 66, no. 1, pp. 321–334, 2017, doi: 10.1109/TVT.2016.2540538.
- [86] L. Li, A. Song, L. J. Cimini, X. G. Xia, and C. C. Shen, "Interference cancellation in in-band full-duplex underwater acoustic systems," in *OCEANS 2015 -*

MTS/IEEE Washington, 2016, doi: 10.23919/oceans.2015.7404411.

- [87] J. Tian, S. Yan, L. Xu, and J. Xi, “A time-reversal based digital cancelation scheme for in-band full-duplex underwater acoustic systems,” in *OCEANS 2016 - Shanghai*, 2016, doi: 10.1109/OCEANSAP.2016.7485471.
- [88] F. Qu, H. Yang, G. Yu, and L. Yang, “In-band full-duplex communications for underwater acoustic networks,” *IEEE Netw.*, vol. 31, no. 5, pp. 59–65, 2017, doi: 10.1109/MNET.2017.1600267.
- [89] G. Qiao, S. Gan, S. Liu, L. Ma, and Z. Sun, “Digital self-interference cancellation for asynchronous in-band full-duplex underwater acoustic communication,” *Sensors (Switzerland)*, vol. 18, no. 6, 2018, doi: 10.3390/s18061700.
- [90] A. Schröder and C. H. B. Henning, “Ultrasonic transducer interface-circuit for simultaneous transmitting and receiving,” *ICEMI 2009 - Proc. 9th Int. Conf. Electron. Meas. Instruments*, pp. 4519–4522, 2009, doi: 10.1109/ICEMI.2009.5274023.
- [91] A. Schröder and B. Henning, “Improved system identification for simultaneous transmitting and receiving in single transducer applications,” *Proc. - IEEE Ultrason. Symp.*, pp. 141–144, 2010, doi: 10.1109/ULTSYM.2010.5935534.
- [92] D. J. Leo and D. K. Limpert, “Self-sensing technique for active acoustic attenuation,” *Collect. Tech. Pap. - AIAA/ASME/ASCE/AHS/ASC Struct. Struct. Dyn. Mater. Conf.*, vol. 4, pp. 2603–2610, 1999, doi: 10.2514/6.1999-1530.
- [93] B. Ko and B. H. Tongue, “Acoustic control using a self-sensing actuator,” *J. Sound Vib.*, vol. 187, no. 1, pp. 145–165, 1995, doi: 10.1006/jsvi.1995.0507.
- [94] J. Qiu, J. Tani, and M. Haraguchi, “Suppression of noise radiation from a plate using self-sensing actuators,” *J. Intell. Mater. Syst. Struct.*, vol. 16, no. 11–12, pp. 963–970, 2005, doi: 10.1177/1045389X05053915.
- [95] K. Oshima, S. Fujii, and T. Mimura, “Noise Reduction by a Loud Speaker Based on Self-Sensing Actuation,” in *IFAC Proceedings Volumes*, 2000, pp. 47–50, doi: 10.1016/s1474-6670(17)39314-x.
- [96] R. Boulandet, “Tunable Electroacoustic Resonators through Active Impedance Control of Loudspeakers,” Dissertation for École Polytechnique Fédérale de Lausanne, 2012.
- [97] E. Anderson, N. Hagood, and J. Goodliffe, “Self-sensing piezoelectric actuation - Analysis and application to controlled structures,” in *33rd Structures, Structural Dynamics, and Materials Conference*, 1992, p. 2465, doi: 10.2514/6.1992-2465.
- [98] E. H. Anderson and N. W. Hagood, “Simultaneous piezoelectric sensing/actuation: Analysis and application to controlled structures,” *J. Sound Vib.*, vol. 174, no. 5, pp. 617–639, 1994, doi: 10.1006/jsvi.1994.1298.

- [99] G. E. Simmers, J. R. Hodgkins, D. D. Mascarenas, G. Park, and H. Sohn, "Improved piezoelectric self-sensing actuation," *J. Intell. Mater. Syst. Struct.*, vol. 15, no. 12, pp. 941–953, 2004, doi: 10.1177/1045389X04046308.
- [100] G. E. Simmers, H. A. Sodano, G. Park, and D. J. Inman, "Thermal protection for a self-sensing piezoelectric control system," *Smart Mater. Struct.*, vol. 16, no. 6, pp. 2492–2500, 2007, doi: 10.1088/0964-1726/16/6/053.
- [101] K. Suresh, G. Uma, and M. Umapathy, "Design of a resonance-based mass sensor using a self-sensing piezoelectric actuator," *Smart Mater. Struct.*, vol. 21, no. 2, 2012, doi: 10.1088/0964-1726/21/2/025015.
- [102] Y. Xie, "Improved self-sensing piezoelectric actuator for dither motor rate control," *J. Intell. Mater. Syst. Struct.*, vol. 24, no. 14, pp. 1747–1753, 2013, doi: 10.1177/1045389X13486708.
- [103] Y. Yang, L. Wang, J. Tan, and B. Zhao, "Induced voltage linear extraction method using an active Kelvin bridge for disturbing force self-sensing," *Sensors (Switzerland)*, vol. 16, no. 5, 2016, doi: 10.3390/s16050739.
- [104] B. I. N. Hu, "Advanced Sensor Fusion and Vibration Control Technologies for Ultra-High Density Hard Disk Drives," Dissertation for National University of Singapore, 2016.
- [105] D. G. Cole and R. L. Clark, "Adaptive Compensation of Piezoelectric Sensoriactuators," *J. Intell. Mater. Syst. Struct.*, vol. 5, no. 5, pp. 665–672, 1994, doi: 10.1177/1045389X9400500510.
- [106] J. S. Vipperman and R. L. Clark, "Implementation of an adaptive piezoelectric sensoriactuator," *AIAA J.*, vol. 34, no. 10, pp. 2102–2109, 1996, doi: 10.2514/3.13358.
- [107] Y. He, X. Chen, Z. Liu, and Y. Qin, "Piezoelectric self-sensing actuator for active vibration control of motorized spindle based on adaptive signal separation," *Smart Mater. Struct.*, vol. 27, no. 6, 2018, doi: 10.1088/1361-665X/aabbf4.
- [108] J. S. Vipperman and R. L. Clark, "Hybrid Model-Insensitive Control Using a Piezoelectric Sensoriactuator," *J. Intell. Mater. Syst. Struct.*, vol. 7, pp. 689–695, 1996.
- [109] W. W. Law, W. H. Liao, and J. Huang, "Vibration control of structures with self-sensing piezoelectric actuators incorporating adaptive mechanisms," *Smart Mater. Struct.*, vol. 12, no. 5, pp. 720–730, 2003, doi: 10.1088/0964-1726/12/5/008.
- [110] J. Qiu and M. Haraguchi, "Vibration control of a plate using a self-sensing piezoelectric actuator and an adaptive control approach," *J. Intell. Mater. Syst. Struct.*, vol. 17, no. 8–9, pp. 661–669, 2006, doi: 10.1177/1045389X06055760.
- [111] M. N. Islam and R. J. Seethaler, "Position self-sensing for piezoelectric actuators in the presence of creep and rate-dependent hysteresis," *Rev. Sci. Instrum.*, vol. 83,

no. 116101–1, pp. 2–5, 2012, doi: 10.1063/1.4764949.

- [112] M. Rakotondrabe, I. A. Ivan, S. Khadraoui, P. Lutz, and N. Chaillet, “Simultaneous displacement/force self-sensing in piezoelectric actuators and applications to robust control,” *IEEE/ASME Trans. Mechatronics*, vol. 20, no. 2, pp. 519–531, 2015, doi: 10.1109/TMECH.2014.2300333.
- [113] S. F. Ling, X. Hou, and Y. Xie, “Decoupling loading effect in simultaneous sensing and actuating for dynamic measurement,” *Sensors Actuators, A Phys.*, vol. 120, no. 1, pp. 257–265, 2005, doi: 10.1016/j.sna.2004.11.034.
- [114] Q. Z. Wang, G. Wang, and F. X. Li, “Precise, Long-Time Displacement Self-Sensing of Piezoelectric Cantilever Actuators Based on Charge Measurement Using the Sawyer-Tower Circuit,” *Chinese Phys. Lett.*, vol. 35, no. 10, 2018, doi: 10.1088/0256-307X/35/10/107701.
- [115] S. Zarif Mansour and R. Seethaler, “Simultaneous quasi-static displacement and force self-sensing of piezoelectric actuators by detecting impedance,” *Sensors Actuators, A Phys.*, vol. 274, pp. 272–277, 2018, doi: 10.1016/j.sna.2018.03.022.
- [116] S. Z. Mansour and R. Seethaler, “Displacement and Force Self-Sensing Technique for Piezoelectric Actuators Using a Nonlinear Constitutive Model,” *IEEE Trans. Ind. Electron.*, vol. 66, no. 11, pp. 8610–8617, 2019, doi: 10.1109/TIE.2018.2890486.
- [117] T. F. Lu, Y. Fan, and T. Morita, “An investigation of piezoelectric actuator high speed operation for self-sensing,” *Meas. J. Int. Meas. Confed.*, vol. 136, pp. 105–115, 2019, doi: 10.1016/j.measurement.2018.12.055.
- [118] A. J. Fleming, S. O. R. Moheimani, and S. Behrens, “Synthesis and implementation of sensor-less active shunt controllers for electromagnetically actuated systems,” *IEEE Trans. Control Syst. Technol.*, vol. 13, no. 2, pp. 246–261, 2005, doi: 10.1109/TCST.2004.839565.
- [119] K. Makihara, J. Onoda, and K. Minesugi, “A self-sensing method for switching vibration suppression with a piezoelectric actuator,” *Smart Mater. Struct.*, vol. 16, no. 2, pp. 455–461, 2007, doi: 10.1088/0964-1726/16/2/025.
- [120] E. Grasso, N. Totaro, H. Janocha, and D. Naso, “Piezoelectric self sensing actuators for high voltage excitation,” *Smart Mater. Struct.*, vol. 22, no. 6, 2013, doi: 10.1088/0964-1726/22/6/065018.
- [121] T. A. Gisby, B. M. Obrien, and I. A. Anderson, “Self sensing feedback for dielectric elastomer actuators,” *Appl. Phys. Lett.*, vol. 102, no. 19, 2013, doi: 10.1063/1.4805352.
- [122] V. Hofmann and J. Twiefel, “Self-Sensing with loaded piezoelectric Bending actuators,” *Sensors Actuators, A Phys.*, vol. 263, no. August 2016, pp. 737–743, 2017, doi: 10.1016/j.sna.2017.06.004.

- [123] R. Boulandet, M. Michau, P. Micheau, and A. Berry, "Aircraft panel with sensorless active sound power reduction capabilities through virtual mechanical impedances," *J. Sound Vib.*, vol. 361, pp. 2–19, 2016, doi: 10.1016/j.jsv.2015.09.042.
- [124] I. A. Ivan, O. Aljanaideh, J. Agnus, P. Lutz, and M. Rakotondrabe, "Quasi-Static Displacement Self-Sensing Measurement for a 2-DOF Piezoelectric Cantilevered Actuator," *IEEE Trans. Ind. Electron.*, vol. 64, no. 8, pp. 6330–6337, 2017, doi: 10.1109/TIE.2017.2677304.
- [125] R. Ambur and S. Rinderknecht, "Unbalance detection in rotor systems with active bearings using self-sensing piezoelectric actuators," *Mech. Syst. Signal Process.*, vol. 102, pp. 72–86, 2018, doi: 10.1016/j.ymssp.2017.09.006.
- [126] K. Jung, K. J. Kim, and H. R. Choi, "A self-sensing dielectric elastomer actuator," *Sensors Actuators, A Phys.*, vol. 143, no. 2, pp. 343–351, 2008, doi: 10.1016/j.sna.2007.10.076.
- [127] K. A. Saalbach, J. Twiefel, and J. Wallaschek, "Self-sensing cavitation detection in ultrasound-induced acoustic cavitation," *Ultrasonics*, vol. 94, no. June 2018, pp. 401–410, 2019, doi: 10.1016/j.ultras.2018.06.016.
- [128] J. N. Potter, P. D. Wilcox, and A. J. Croxford, "Diffuse field full matrix capture for near surface ultrasonic imaging," *Ultrasonics*, vol. 82, pp. 44–48, 2018, doi: 10.1016/j.ultras.2017.07.009.
- [129] R. N. McDonough and A. D. Whalen, *Detection of Signals in Noise*, 2nd ed. Cambridge: Academic Press, 1995.
- [130] S. W. Smith, *The Scientist and Engineer's Guide to Digital Signal Processing*. San Diego: California Technical Publishing, 1997.
- [131] M. Richards, *Fundamentals of Radar Signal Processing*, 2nd ed. New York: McGraw-Hill Education, 2014.
- [132] T. Snow, "Interference Mitigation for Simultaneous Transmit and Receive Applications on Digital Phased Array Systems," Dissertation for Purdue University, 2014.
- [133] H. Esfahlani, H. Lissek, and J. R. Mosig, "Generation of acoustic helical wavefronts using metasurfaces," *Phys. Rev. B*, vol. 95, no. 024312, 2017.
- [134] B. H. Song and J. S. Bolton, "A transfer matrix approach for estimating the characteristic impedance and wave numbers of limp and rigid porous materials," *J. Acoust. Soc. Am.*, vol. 107, no. 1131, 2000.
- [135] "ASTM E2611-09, Standard test method for measurement of normal incidence sound transmission of acoustical materials based on the transfer matrix method," West Conshohocken, PA, 2009.

- [136] E. I. Alekseev, E. N. Bazarov, V. . Gubin, A. I. Sazonov, M. I. Starostin, and A. I. Oussov, “Recirculating fibre ring interferometer with compensation for losses in the cavity,” *Quantum Electron.*, vol. 31, no. 1113, 2001.
- [137] H. Haus, *Waves and Fields in Optoelectronics*. Englewood Cliffs, NJ: Prentice-Hall, 1984.
- [138] T. W. Van Doren, “Propagation of finite amplitude sound in multiple waveguide modes,” Dissertation for the University of Texas at Austin, 1993.
- [139] A. Alù and N. Engheta, “Dielectric sensing in -near-zero narrow waveguide channels,” *Phys. Rev. B - Condens. Matter Mater. Phys.*, vol. 78, no. 4, pp. 1–5, 2008, doi: 10.1103/PhysRevB.78.045102.
- [140] Q. Cheng, W. X. Jiang, and T. J. Cui, “Spatial power combination for omnidirectional radiation via anisotropic metamaterials,” *Phys. Rev. Lett.*, vol. 108, no. 213903, 2012.
- [141] M. Navarro-Cia, M. Beruete, M. Sorolla, and N. Engheta, “Lensing system and Fourier transformation using epsilon-near-zero metamaterials,” *Phys. Rev. B*, vol. 86, no. 165130, 2012.
- [142] L. W. Schmerr and J.-S. Song, *Ultrasonic Nondestructive Evaluation Systems: Models and Measurements*. Springer US, 2007.
- [143] C. H. Sherman and J. L. Butler, *Transducers and arrays for underwater sound*, 2nd ed. Springer New York, 2007.
- [144] M. S. Byrne, H. Esfahlani, M. McDermott, and A. Alù, “Acoustic Supercoupling in a Zero-Compressibility Waveguide,” *Research*, vol. 2019, no. 2457870, 2019, doi: 10.34133/2019/2457870.
- [145] M. S. Byrne, H. Esfahlani, and A. Alù, “Acoustic power divider based on compressibility-near-zero propagation,” *Phys. Rev. Appl.*, vol. 14, no. 2, p. 1, 2020, doi: 10.1103/PhysRevApplied.14.024057.
- [146] E. Mor, A. Azoulay, and M. Aladjem, “A Matching Pursuit Method for Overlapping Ultrasonic Echoes,” *IEEE Trans. Ultrason. Ferroelectr. Freq. Control*, vol. 57, no. 9, pp. 1996–2004, 2010.
- [147] F. W. T. Yeh, T. Lukomski, J. Haag, T. Clarke, T. Stepinski, and T. R. Strohaecker, “An alternative Ultrasonic Time-of-Flight Diffraction (TOFD) method,” *NDTE Int.*, vol. 100, no. July, pp. 74–83, 2018, doi: 10.1016/j.ndteint.2018.08.008.
- [148] T. Szabo, *Diagnostic Ultrasound Imaging: Inside Out*, 2nd ed. Academic Press, 2013.
- [149] D. W. Beran, C. G. Little, and B. C. Willmarth, “Acoustic doppler measurements of vertical velocities in the atmosphere,” *Nature*, vol. 230, no. 5290, pp. 160–162,

1971, doi: 10.1038/230160a0.

- [150] M. S. Phanikumar, I. Aslam, C. Shen, D. T. Long, and T. C. Voice, “Separating surface storage from hyporheic retention in natural streams using wavelet decomposition of acoustic Doppler current profiles,” *Water Resour. Res.*, vol. 43, no. 5, pp. 1–16, 2007, doi: 10.1029/2006WR005104.
- [151] A. D. Pierce, *Acoustics: An Introduction to Its Physical Principles and Applications*, 3rd ed. Springer, 2019.